NF1 as a regulator of cytoskeleton dynamics and biomarker for decision-making in HER2-positive breast cancer

by

Bruno Achutti Duso, M.D.

A Dissertation

Presented to the European School of Molecular Medicine (SEMM) and the

University of Milan (UniMi),

In Fulfillment of the Requirements for the Degree of

Doctor of Philosophy

Milan, MI

February, 2023

Luca Mazzarella, M.D. Ph.D.

Dissertation Mentor

For Rython

ABSTRACT

The tumour suppressor *NF1* is best characterised as a canonical negative Ras regulator, but sparse evidence suggests additional Ras-independent roles. The interaction of its product neurofibromin with both microtubule (MT) and actin cytoskeleton remains poorly characterised to date but may be of particular therapeutic interest as *NF1* is somatically mutated across multiple tumour types. We identified *NF1* as the second most differentially mutated gene between metastatic and primary HER2$^+$ breast cancer (BC), so we investigated the biological consequences of *NF1* loss on sensitivity to antineoplastic treatment and on the metastatic process. We generated *NF1* knockout (KO) HER2$^+$ BC cells (i.e.: BT-474, SK-BR-3, HCC1954) by CRISPR/Cas9. *NF1*KO cells demonstrated exquisite sensitivity to the antibody-drug conjugate (ADC) trastuzumab emtansine (T-DM1). This hypersensitivity was specific to the mertansine MT-targeting component (DM1) since it was i) replicated by the naked payload but not the antibody alone; ii) absent with other ADCs (i.e.: trastuzumab deruxtecan [T-DXd]); iii) not accompanied by increased T-DM1 uptake; and iv) associated with increased drug-target engagement in *NF1*KO cells. The mechanism is likely Ras-independent, as oncogenic Ras overexpression did not alter T-DM1 sensitivity. By combining molecular biology with confocal and live-cell imaging, we discovered that *NF1*KO cells exhibited marked signs of altered mitosis with longer G2/M duration, supernumerary centrosomes, chromosome misalignment and frequent aneuploidy. In agreement, we found that BC patients bearing *NF1* mutations from the AACR-GENIE cohort exhibited a higher aneuploidy score (AS). MTs in *NF1*KO cells were severely hypodynamic and showed imbalanced expression of plus/minus end MT-associated proteins (MAPs). This was also associated with an increased abundance of GTP-bound tubulin, a conformational state known to cause MT stability. This raises the intriguing possibility that *NF1* may directly regulate tubulin intrinsic GTP-hydrolysis, similar to its GTPase activity on Ras. Finally, we show that *NF1*KO cells present with markedly anchorage-independent growth advantage, a feature associated with acquisition of metastatic potential. Assessment of biophysical properties of *NF1*KO models showed enhanced actin subcortical mesh with upregulation of cell junction markers and marked global stiffening by atomic force microscopy. This study provides extensive mechanistic evidence for a previously underappreciated role of *NF1* in MT and actin dynamics, which reshapes our understanding of its tumour-suppressive activity and provides a rationale for the pharmacological targeting of *NF1*-mutated tumours in prospective clinical trials.

TABLE OF CONTENTS

INDEX OF FIGURES

GLOSSARY

ADCC: antibody dependent cell-mediated cytotoxicity;

APC: anaphase-promoting complex;

BC: breast cancer;

CDK4/6: cyclin-dependent kinase 4 and 6;

CETSA: cellular thermal shift assay;

CFA: colony formation assays;

CIN: chromosomal instability;

Cryo-EM: cryoelectron microscopy;

CSRD: cysteine and serine-rich domain;

CTC: circulating tumour cells;

CTD: C-teminal domain;

ctDNA: circulating tumour DNA;

DAR: drug-to-antibody ratio;

dMMR: defficient mismatch repair;

EGFR: epidermal growth factor receptor;

ER: estrogen receptor;

ESCAT: ESMO Scale for Clinical Actionability of molecular Targets;

GAP: GTPase-activating protein;

GDP: guanosine diphosphate;

GEF: guanine nucleotide-exchange factor;

GO: gene ontology;

GRD: GAP-related domain;

GTP: guanosine triphosphate;

HER2: human epidermal growth factor receptor 2;

HR: hormone receptor;

IHC: immunohistochemistry;

ILC: invasive lobular carcinoma;

ILD: interstitial lung disease;

KO: knockout;

LoF: loss of fucntion;

LRD: leucine-rich domain;

mAB: monoclonal antibody;

MAPS: microtubule-associated proteins;

mBC: metastatic BC;

MSI: microsatellite instability;

MT: microtubule;

MTAs: microtubule targeting agents;

MTB: molecular tumour board;

NGS: next generation sequencing;

NLS: nuclear localisation sequence;

OR: odds ratio;

OS: overall survival;

PD-1: programmed cell death protein 1;

PD-L1: programmed cell death ligand 1;

PFS: progression-free survival;

PgR: progesterone receptor;

PM: plasma membrane;

RasGAP: Ras GTPase activating protein;

SAC: spindle assembly checkpoint;

SD: standard deviation;

Sec14/PH: Sec14 homologous domain and pleckstrin homologous domain;

SEM: standard error of the mean;

SERD: selective estrogen receptor degrader;

SPRED1: sprouty-related EVH1 domain containing 1;

T-DM1: trastuzumab emtansine;

T-DXd: trastuzumab deruxtecan;

TBD: tubulin-binding domain;

TILs: tumour-infiltrating lymphocytes;

TKI: tyrosine kinase inhibitor;

TMB: tumour mutational burden;

TNBC: triple negative breast cancer;

WT: wild type.

1. INTRODUCTION

1.1. Background on metastatic breast cancer

1.1.1. Epidemiology and molecular taxonomy

Excluding non-melanoma skin cancer, breast cancer (BC) is the most frequent tumour, with escalating incidences worldwide, especially in women under 50[1,2]. A total of 2.3 million new cases were diagnosed in 2020, with 685.000 BC-related deaths (**figure I1A**)[2]. For 2040 these numbers are predicted to increase by around 40 and 50%, respectively: about 3 million cases/year and a 1 million deaths. Low-human development index (HDI) countries are expected to rise the most, with an almost doubling of both indicators[3]. (**figure I1B, C**). These worrying data prompted the launch of the Global Breast Cancer Initiative by the World Health Organization (WHO)[4], with the goal of undertaking global sustainable efforts to improve outcomes in BC by promoting early diagnosis and adequate treatment.

In the last 20 years, BC understanding has passed from gene expression-based instrinsic subtype classification[5,6] to point mutations, and gene based on somatic copy number aberrations, point mutations, and gene expression[7–11]. Although several commercial tests are available, with variable predictive power and often discordant [12], immunohistochemistry (IHC) remains the cornerstone of diagnostic and therapeutic guidance, acting as a surrogate to classify BC, as proposed by the St Gallen[13], in:

- **Hormone receptor (estrogen receptor [ER]/progesterone receptor [PgR]) positive (HR^+)/human epidermal growth factor receptor 2 (HER2) negative ($HER2^-$)** tumours that, based on proliferative markers Ki67 and HER2 status, are further stratified into:

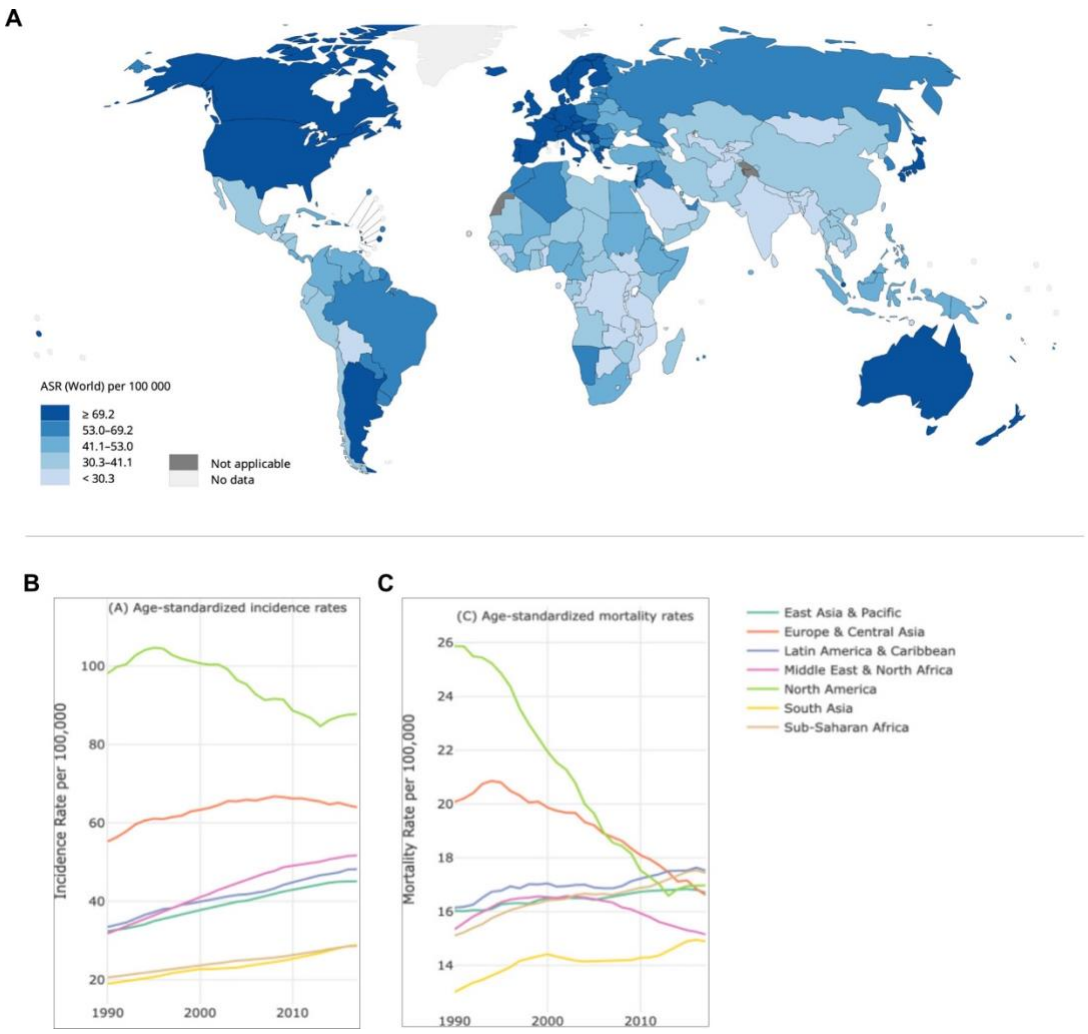

Figure I1. **A.** Age-standardized rate (ASR) of BC incidence worldwide. Data source: GLOBOCAN 2020. Map generation: IARC (https://gco.iarc.fr/today/) World Health Organisation; **B.** Trends in the incidence and **C.** mortality rate of BC, through time, age-standardised, according to world region. Modified from Lima SM et al[1].

- Luminal A-like, with the lowest proliferation status, an excellent prognosis, chemorefractory in most part but very much sensitive to endocrine therapy;
- and Luminal B-like, with higher proliferation rates, a poorer prognosis, still responds scarcely to chemotherapy and is less sensitive to hormone modulation.

In these tumours, gene expression-based prognostic assays are usually performed in the adjuvant setting as a way of, alongside other clinical features (e.g.: node status), identifying those patients that would not benefit from the addition of chemotherapy to the systemic regimen[14].

- **HR$^-$/HER2$^-$** triple negative breast cancer (TNBC), mostly composed of basal-like and claudin-low tumours, is characterised by the lack of ER, PR and HER2 expressions. Historically, it tends to present with the worst outcomes from all subtypes, both due to its natural history as well as to the lack of specific targets. Although, In the last >5 years, immune activation signatures, a dysfunctional DNA repair machinery, and trophoblast cell-surface antigen 2 (TROP2) expression have been particularly associated with these cases, enabling new therapeutic approaches[15] and changing disease course.
- **HR$^+$/HER2$^+$** tumours, accounting for both Luminal B with HER2 overexpression and the HER2-enriched subtype.
- **HR$^-$/HER2$^+$** tumours, which on their majority represent the HER2-enriched subtype identifiable by PAM50.

In the context of HER2$^+$ disease, a strong debate arose recently on the importance of lower levels of HER2 (i.e.: IHC 1+ or IHC2+ with a negative in-situ hybridisation). Accumulating evidence suggests that it does not constitute a distinct molecular entity, but rather expands our understanding and opportunities within the HER2 expression continuum, in particular with the advent of trastuzumab deruxtecan (T-DXd), which demonstrated activity in patients with HER2-low tumours[16–18]. New tests are surfacing for better characterisation of these patients. The first to be largely validated is the HER2DX, a gene-expression based assay that looks at immune infiltration, tumour cell proliferation, luminal differentiation, and the expression of the HER2 for inputs on prognosis and prediction of response to neoadjuvant therapy[19,20].

This stratification strategy was useful to standardise patient care and surely had an impact on the improved patient outcomes, but is recognised to be still shortsighted, since not infrequently patients within the same IHC-based group present with divergent clinical presentations, disease aggressiveness and treatment responses. As new prognostic and predictive markers are being unraveled, there is a growing need to navigate through disease complexity. For this narrative, we will focus on the therapeutic aspects of locally advanced and metastatic HER2$^+$ tumours.

1.1.2. Treatment of advanced HER2$^+$ disease

Efficient targeting of tumour addiction to HER2 with monoclonal antibodies (mAbs) (e.g.: trastuzumab, pertuzumab, margetuximab), tyrosine kinase inhibitors (TKIs) (e.g.: lapatinib, neratinib, tucatinib) and antibody-drug conjugates (ADCs) (e.g.: trastuzumab emtansine [T-DM1], T-DXd), has dramatically contributed, in combination with chemotherapy, to improve survival rates (**figure I2**)[21,22]. In the early setting, 5-year survival rates exceed 90%, but in metastatic disease, resistance develops almost inevitably and mortality remains unacceptably high[23,24].

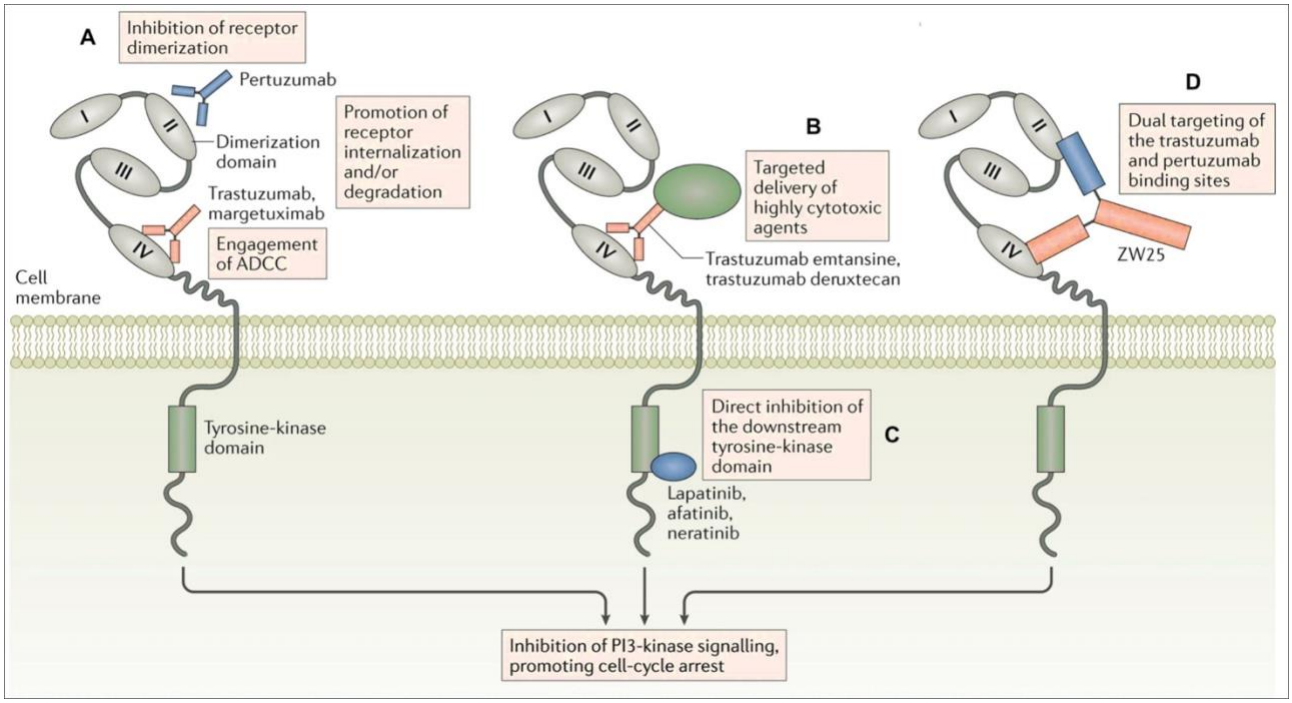

Figure I2. The distinct mechanisms of anti-HER2 drugs. **A.** mAbs that target one extracellular domain of the HER2 receptor and exert their antitumour activity through inhibition of downstream signalling pathways, activation of antibody-dependent cellular cytotoxicity (ADCC) or by preventing dimerisation of HER2 with other HER family members; **B.** ADCs, detailed below; **C.** TKIs, that bind to the intracellular domain of HER2 and act by blocking phosphorylation of the tyrosine kinase residue, inhibiting cell proliferation through the MAPK and PI3K pathways; **D.** Bispecific antibodies (e.g.: ZW25) target more than one of the HER2 extracellular domains. Clinical data on those agents are limited to early phase trials and they will not be addressed. Adapted from Oh D & Bang[25].

Today, a neoadjuvant combination of targeted and cytotoxic agents is the standard of care in locally advanced HER2$^+$ BC, aiming to (i) de-escalate surgery in the breast/axilla and (ii) prospect post-neoadjuvant strategies based on objective response. Radiation remains an important cornerstone

of BC therapy, with risk-adapted, hypofractionated regimens, and partial breast irradiation as options within the standard of care[26]. In the metastatic setting, the first-line recommended regimen is still the combination of trastuzumab, pertuzumab and a taxane if a patient is fit for receiving chemotherapy. Two options are suitable for second-line according to previous drug exposure and central nervous system involvement, and several ones available in the third-line setting[27–29]. The algorithm from **figure I3** covers the standard of care for most of HER2$^+$ metastatic BC (mBC) in the present day.

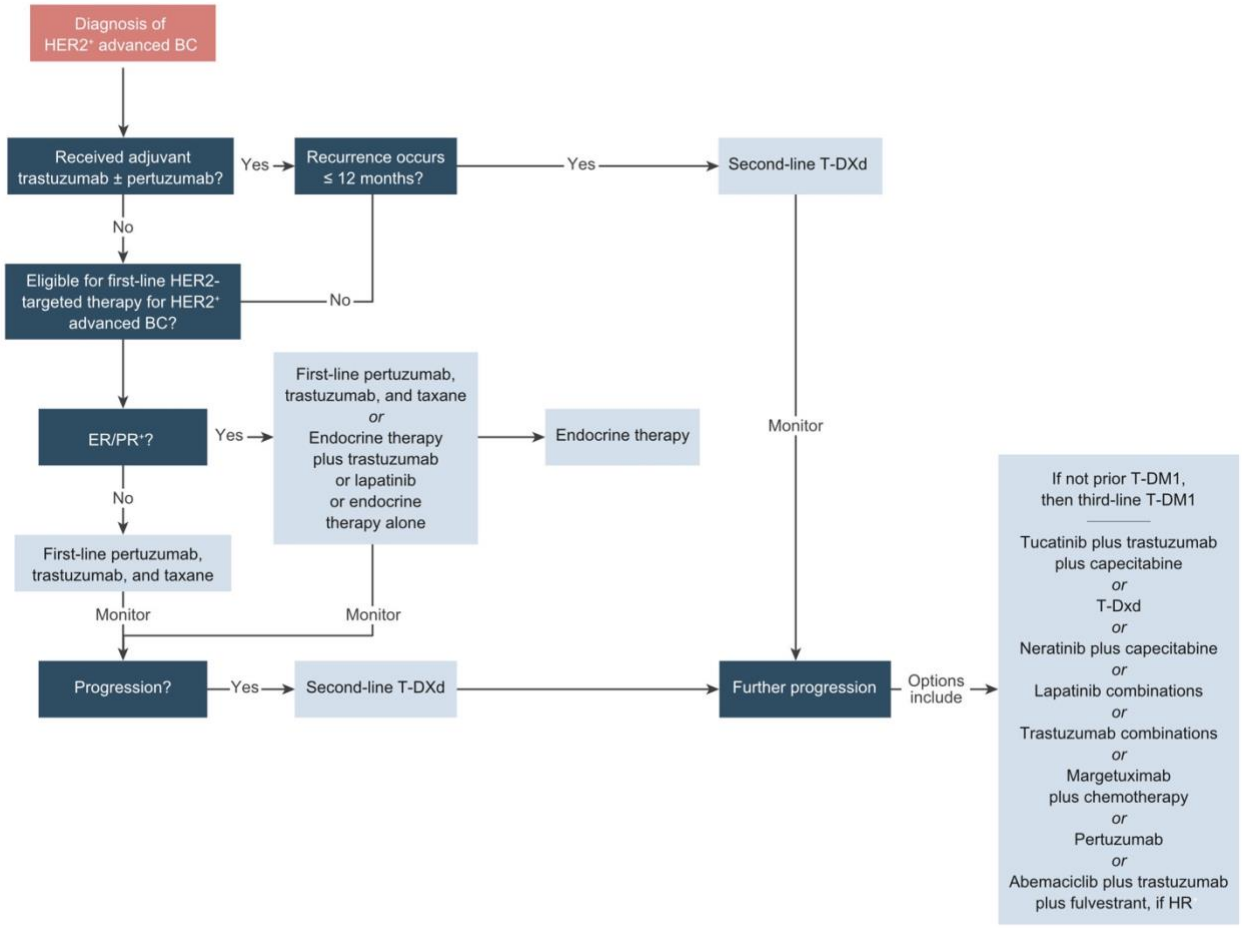

Figure I3. An updated, nonexhaustive reasoning for treating HER2$^+$ advanced disease. Approved biosimilars are an option instead of trastuzumab. Modified from Giordano SH et al.[27]

Additionally, tumours that also express HR may receive endocrine therapy plus a cyclin-dependent kinase 4 and 6 (CDK4/6) inhibitor in combination with anti-HER2 therapy once chemotherapy is completed. A relevant update in the systemic therapy of this population has been the approval of T-DXd in the second-line setting, basically replacing T-DM1 10 years after its first approval[30,31]. T-DXd demonstrated significantly longer median progression-free survival (PFS) in the DESTINY-

Breast03 trial, in genomically unselected HER2$^+$ mBC patients after progression on trastuzumab and a taxane[32,33]. No overall survival (OS) data is available yet. However, greater effectiveness of T-DXd was associated with greater toxicities. A higher incidence of drug-related adverse effects was reported for T-DXd across BC, lung, gastric, and colorectal cancers, with rates of interstitial lung disease (ILD)/pneumonitis of 15.4% and grade 5 toxicity (death) in 2.2% of cases[34]. Today, there are no biomarkers to identify specific subgroups that may derive an equal or greater benefit from T-DM1 or other agents in this context.

Both T-DM1 and T-DXd are ADCs, a class of agents that have changed paradigms in oncology by granting potent cytotoxic agents the possibility to be specifically delivered to cancer cells (**figure I4**). These molecules are the product of the bioconjugation of a mAb, a linker, and a cytotoxic payload. The mechanism of ADC efficacy is becoming clearer as drug development evolves and embraces multiple factors: (i) the specificity of the mAb component for the tumour-associated antigen; (ii) the stability and cell-sensitivity of the synthetic linker, which should remain uncleaved in the bloodstream to avoid ectopic drug release but promptly cleaveable within tumour cells, and (iii) a highly potent payload that can induce target cell death once internalised[35–37].

T-DM1 was the first anti-HER2 ADC to conclude development in HER2$^+$ BC and consists of trastuzumab joined by a noncleavable thioether linker (MCC) to mertansine (DM1) with a drug-to-antibody ratio (DAR) of 3.5. DM1 is a potent inhibitor of microtubule dynamics[38]. Its specific binding site lies at the interface between tubulin dimers on the β-tubulin subunit[39]. T-DXd, on the other hand, shares only the trastuzumab moiety. The linker, a cathepsin-cleavable tetrapeptide-based, connects the mAb to DXd with a 7.7 DAR. DXd, an exatecan derivate, is a metabolic activation-independent topoisomerase I inhibitor, approximately 3- to 10- times more potent than SN-38[40,41].

A common drawback for most ADCs is the absence of good predictive biomarkers - apart from quantifying the mAb target - in order to improve patient selection[42]. A recent exploratory analysis of the DAISY trial suggested that the spatial distribution of HER2 may predict response to T-DXd; response rates were lower in patients in which HER2-expressing cells were spatially far from each other (average cell density ~30%), compared to samples where they were clustered closer (average cell density ~96%). Mutations in *SLX4* - a gene involved in the DNA repair machinery - were also found in 20% of samples at progression as compared to 2% at baseline, implying it as a possible mediator of payload resistance[43].

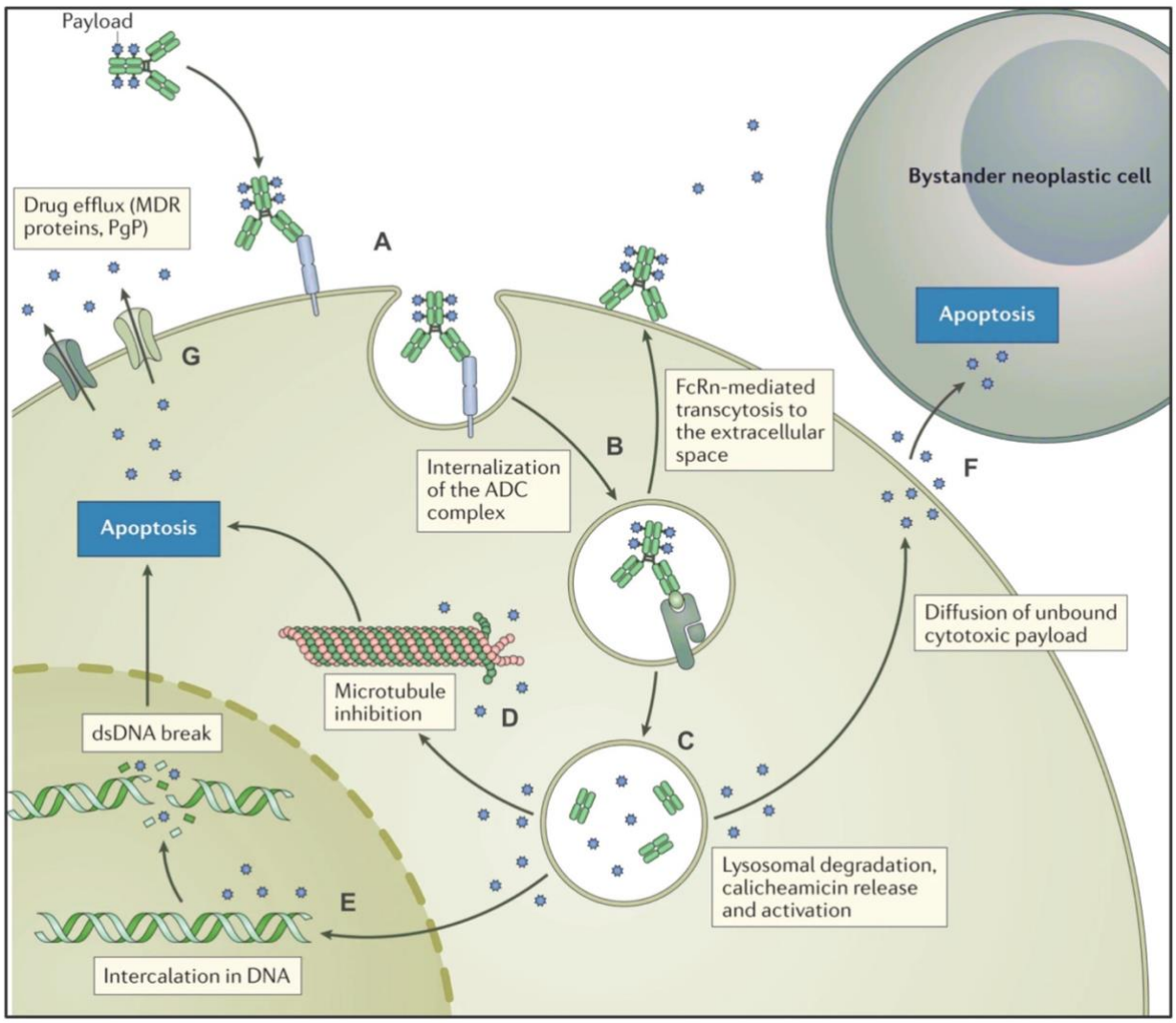

Figure I4. A summary of how an ADC works. **A.** Molecules engage the specific antigen through the mAb component and most are **B.** internalised, predominantly through endocytosis along with their bound payloads (a fraction is able to bind to the endosome Fc receptor, get transported to the cell surface and released into the extracellular space via neonatal Fc receptor (FcRn)-mediated transcytosis); **C.** The acidic, proteolytic or redox conditions inside the mature endosome/lysosome causes the release of the cytotoxic component from the remaining ADC, which then diffuses into the cytoplasm to act upon its substrate (e.g.: **D.** microtubules, for T-DM1 or **E.** DNA, for T-DXd); **F.** Hydrophobic payloads can also diffuse through cell membranes, inducing cytotoxic activity against neighbouring cells irrespective of their expression of the target antigen. This "bystander effect" is considered to be a contributing feature to the efficacy of ADCs in tumours with heterogeneous expression of the mAb target. **G.** Upregulation of drug efflux pumps and multidrug resistance (MDR) proteins is an example of acquired resistance mechanism to ADCs, reducing overall effectiveness of the drug. Modified from Jabbour, Paul & Kantarjian[35].

1.1.3. A current picture of precision medicine in BC

The efforts on molecular profiling, with germline-corrected data and patients with >10y follow up[7,9,44], have led to the identification of at least 40 putative cancer driver genes. However, how to efficiently use this information may be the most difficult step to accomplish. Knowledge databases, like OncoKB[45] and the ESMO Scale for Clinical Actionability of molecular Targets (ESCAT), rank molecular targets based on the best available evidence and provide a systematic framework to support their value as clinical targets[46]. The latter was used in the mBC context within the SAFIR02-Breast trial, where results from multigene sequencing and SNP array were used as tools to guide systemic therapy, improving the outcomes of patients only if they carried alterations classified in the I/II tiers of the scale [47]. Indeed, many molecular tumour boards (MTBs) are evaluating the genomic alterations from tissues and plasma based on the ESCAT to recommend treatment strategies. Current recommendations[48] for the usage of biomarkers to guide mBC therapy, apart from (re)assessing ER, PgR and HER2 status, consist of routine testing for:

- ***PIK3CA*** somatic variants for $HR^+/HER2^-$ patients who may be eligible for regimens including a PI3K inhibitor (i.e.: alpelisib) in combination with hormone therapy (i.e.: fulvestrant). Assessment should be performed with next-generation sequencing (NGS) of tumour tissue samples or circulating tumour DNA (ctDNA) from plasma;
- ***ESR1*** mutations (any missense mutation in codons 310-547) for $HR^+/HER2^-$ postmenopausal women or men with advanced BC that may be eligible for treatment with elacestrant - a new oral SERD[49,50];
- ***BRCA1*** and ***BRCA2*** germline pathogenic variants for $HER2^-$ patients who may be candidates for poly (ADP-ribose) polymerase (PARP) inhibitors (i.e.: olaparib);
- ***PD-L1*** expression in both the tumour and immune cells with an US Food and Drug Administration (FDA)/European Medicines Agency (EMA)-approved test, **defficient mismatch repair/microsatellite instability (dMMR/MSI),** and **tumour mutational burden (TMB)** to designate a patient as candidate for treatment with an immune-checkpoint inhibitor (i.e.: pembrolizumab, dostarlimab-gxly) in monotherapy or combined with chemotherapy;
- ***NTRK*** fusions, at physician's discretion, for patients who may be eligible for treatments including a TRK inhibitor (i.e.: larotrectinib, entrectinib).

PALB2 germline variants, BRCA1/BRCA2 somatic variants, homologous recombination deficiency (HRD), trophoblast cell-surface antigen 2 (TROP2) expression, circulating tumour DNA (ctDNA) and circulating tumour cells (CTCs) still have accumulate insufficient evidence to support their routine assessment outside clinical trials.

Data from the TCGA Pan-Gyn cohort (n = 2579 fresh-frozen primary samples - 1097 BC, 579 ovarian cancers, 308 uterine cervix cancers, 548 endometrial carcinomas and 57 uterine carcinosarcomas - prior to any chemotherapy or radiation therapy) highlights *MAP2K4* and *NF1* as notable tumour suppressor genes with recurring copy-number losses[51]. Our group also confronted samples from BC patients from large datasets[52–54] looking for mutations that were enriched in the metastatic setting compared to primary lesions (*see section 2.1.1)*. We found *NF1* as the single most significantly enriched gene within ERBB2-amplified tumours. The biology of *NF1* will be discussed in the next sections.

1.2. The Neurofibromin 1 (NF1) gene and its product

The *NF1* gene was precisely mapped to the 17q11.2 chromosome locus in 1989[55], following the identification of two patients with neurofibromatosis type 1 and chromosome 17 translocations. The exact sequence of flanking markers and confidence limits of the recombination fractions were explored on the following years by pioneer efforts from groups like Dr. Francis S. Collins'[56,57], Dr. Robert Weiss'[58,59] and Dr. Frank McCormick's[60], until the entire *NF1* coding sequence was assembled in 1991[61]. *NF1* is one of the largest human genes and it spans over 350kb of genomic DNA[62], encoding a transcript containing 57 constitutive exons and 4 alternatively spliced, tissue-specific variants (**figure I5A**)[63]. The discovery that multiple tumours are associated with germline disruption of the *NF1* gene, the identification of *NF1* somatic mutations in sporadic solid and haematological neoplasms as well as the autosomal dominant mode of inheritance of neurofibromatosis type 1 syndrome[64] have promptly established *NF1* as a tumour-suppressor gene[65]. *NF1* is highly evolutionary conserved across eukaryotes, from *Dictyostelium* amoebae[66], through the common fruit fly *Drosophila melanogaster*[67] the ray-finned fish *Takifugu rupripes*, murines, chimpanzees and humans (The Ensembl database (http://www.ensembl.org, release 108 - Oct 2022), with homology levels ranging from 60[68] to 100%.[69] Currently, over 3890 different inherited (likely pathogenic) *NF1* variants have been reported in the Human Gene Mutation Database (HGMD®, Professional 2021.4) and 2889 (pathogenic) in Clinvar (Nov 2022), varying from missense/nonsense

(27.7%), splicing (16.3%), microdeletions (26.9%), microinsertions (11.1%), indels (2%), gross deletions (>20 bp, 13.3%), gross insertions (>20 bp, 2%), complex rearrangements (0.6%) and a couple of putative regulatory mutations[70,71]. There is no evidence of mutational hot spots throughout the gene[72], suggesting an acute susceptibility of the entire protein to dysregulation, probably due to the complex nature of its final structural topology (*see section 1.2.1*). Accordingly, the vast majority (~82%) of constitutional *NF1* mutations are inactivating, predicted to result in almost complete absence of the transcript or protein[73].

The *NF1* gene encodes a large protein of 2818-2839 amino acids (aa) and predicted ~320 kDa called neurofibromin[74]. First sequence analyses showed a striking homology between *NF1* from human tissues and (i) *Saccharomyces cerevisiae IRA1* and *IRA2* genes, which were known to negatively regulate the RAS/cyclic AMP (cAMP) pathways[75] and (ii) the catalytic domains of p120 GTPase-activating protein (GAP) through a 360 aa sequence that later would be described as the GAP-related domain (GRD)[76]. This family of proteins decrease the activity of the small membrane-anchored guanine nucleotide binding protein (G-protein) Ras by accelerating its intrinsic rate of GTP hydrolysis from active GTP-bound Ras into the inactive GDP-bound form[77]. Confirmation of said function came from experiments showing that this portion of *NF1* complemented the function of *IRA1* and *IRA2*, restoring a wildtype phenotype when expressed in *IRA*-mutated yeast by stimulating the intrinsic GTPase activity of the yeast Ras protein or the GTPase activity of human Ras expressed in yeast [56,60,78], establishing neurofibromin as a Ras-GAP.

1.2.1. Neurofibromin isoforms, structure, domains and interactors

To date, at least six different *NF1* pre-mRNA undergoing alternative splicing have been reported and enough characterised - from which some do (30alt31, Δe43) and some do not (11alt12, 12alt13, 56alt57) alter the reading frame of the gene -, suggesting a complex regulation of *NF1* transcript processing and time- and tissue-specific expression variability[74,79–82]. The two most abundant isoforms are isoform 1 (UniProt P21359-2), which contains 2818 aa, has a predicted molecular weight of 327 kDa and contains 57 exons with no alternative inclusions; and isoform 2 (UniProt P21359) which contains a 21 aa insertion encoded by exon 30alt31. Noteworthy are two other variants: the *NF1* Δe43 splice variant, lacking exon 51 with its functional nuclear localisation sequence (NLS), which regulates a timely nuclear import of *NF1* in late S-G2[81,83]. This variant seems to be particularly expressed in tissues where *NF1* mRNA levels are high during embryonic

development but barely detectable in adults (i.e.: lungs, liver, placenta, kidneys, skeletal muscle) and may have a unique role in spindle assembly and chromosome segregation[84]. This isoform is not associated with the neurofibromatosis type 1 syndrome[85]. The other is a recently discovered isoform with a 140 bp deletion in exon 21, exclusively present in a BC cell line, where it might promote tumourigenesis by inducing a premature stop and functionally impact the GRD and its downstream domains[86].

While individual central domains of neurofibromin were crystallised relatively early on (i.e.: the GRD and a Sec14-like with a tightly interacting pleckstrin homology [PH] domain that together are referred to as the Sec14/PH module[87,88]), the overall organisation of the protein has long remained elusive. Recently, structures of neurofibromin solved by cryoelectron microscopy (cryo-EM) have revealed that *NF1* is arranged in a dimer (~640 kDa), bound head-to-tail in a lemniscate shape. This dimer exists in two conformations[72,89–91]: an allosterically, nucleotide-activated state and an autoinhibited closed one. Several domains were identified in neurofibromin: a cysteine/serine-rich domain (CSRD) and a tubulin-binding domain (TBD) at its N-terminal; the GRD, a Sec14/PH and a leucin-rich domain (LRD)[92] at its center; and a focal adhesion kinase (FAK)/dihydropyrimidinase-like 2 (DPYSL2)[93]-interacting domain at its C-terminal (CTD), which contains the embedded NLS[83]. High-resolution crystal structures, however, are presently limited to the GRD[87,94] and the Sec14/PH[95]. As of today, no further details exist on the biochemistry or structure of the remaining ~70-80% of the protein. Domain structure is depicted in **figure I5B**.

1.2.2. Current knowledge on *NF1* somatic mutations and their role on tumour progression

Neurofibromatosis type 1 [Online Mendelian Inheritance in Man (OMIM) #162200], an autosomal dominant multisystem disorder, is the most common tumour-predisposing disease in humans, with an incidence ranging from 1:960 to 1:7.812 [96,97]. Approximately 50% are inherited and in more than 80% of cases a germline pathogenic variant of *NF1* leads to a complete loss of function (LoF) or reduction of neurofibromin, which translates into a wide spectrum of clinical findings, including pigmentary skin lesions, neurofibromas, skeletal abnormalities, cognitive disorders and malignances of varying grades[64].

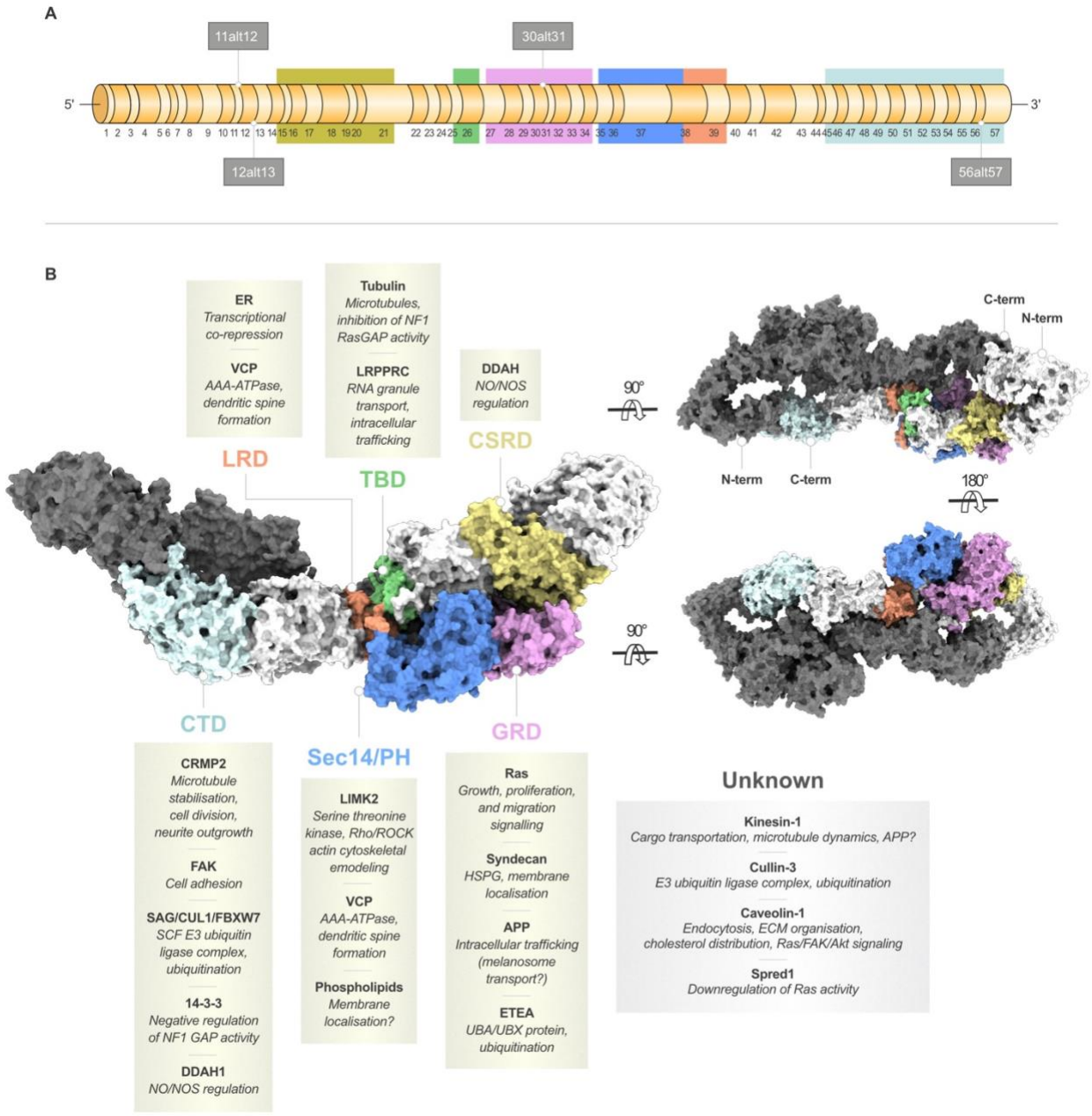

Figure I5. A. Representation of the *NF1* gene with its 57 exons and alternative mRNA transcripts; **B.** Structural image of a neurofibromin dimer and its domains, with a schematic representation of known and unknown interactors[98]. CSRD (cysteine- and serine-rich domain), TBD (tubulin-binding domain), GRD (GAP-related domain), Sec14/PH (Sec14 homologous domain and pleckstrin homologous domain), LRD (leucin-rich domain), and CTD (C-terminal domain). Figure was generated together with L Scietti, head of the Biochemistry and Structural Biology Unit at the Department of Experimental Oncology, European Institute of Oncology, Milan.

Somatically, *NF1* is the 15th most common driver gene according to the integrative analysis of 2658 whole-cancer genomes and their matching normal tissues from 38 tumour types within the

Pan-Cancer Analysis of Whole Genomes (PCAWG) Consortium of the International Cancer Genome Consortium (ICGC) and The Cancer Genome Atlas (TCGA)[99]. Alterations are distributed as shown in **figure I6.**

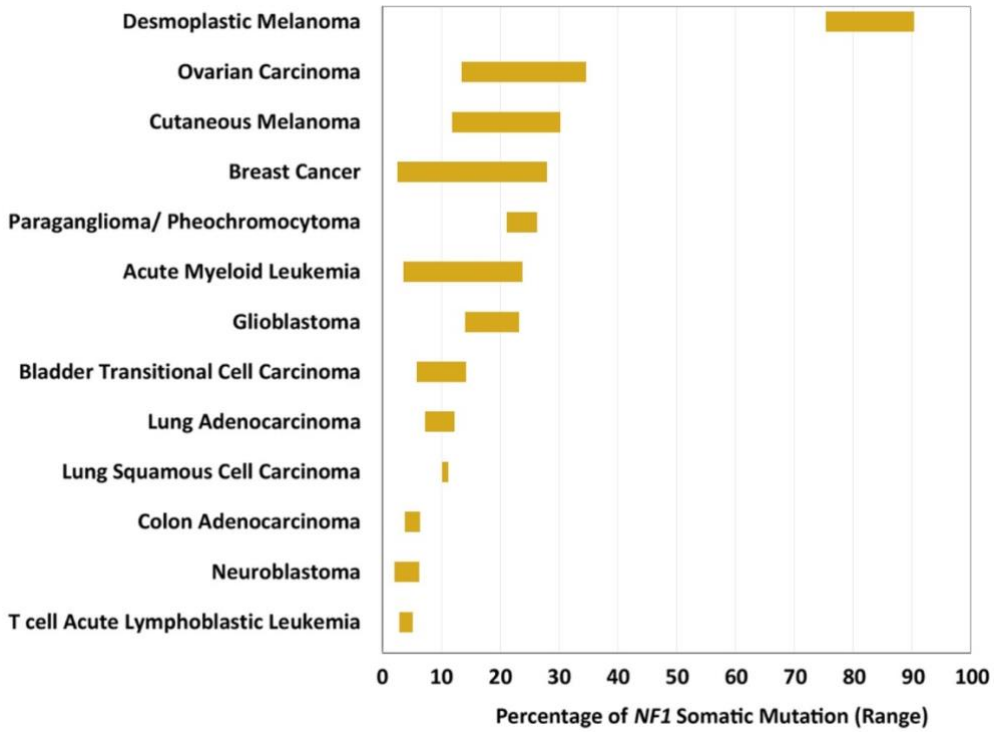

Figure I6. Somatic *NF1* mutation frequencies (range, %) across tumours. Modified from Mo J, Moye SL, McKay RM & Le LQ[100].

1.2.3.1. NF1 and Ras

In GTP-binding proteins, the nucleotide loading and hydrolysis cycle between an inactive GDP-bound and an active GTP-bound state is regulated by guanine nucleotide-exchange factors (GEFs) or GAPs, respectively[101]. The Ras superfamily proteins form heterodimeric complexes with their cognate GAPs to stabilise and/or complement the active site and increase the rate of hydrolysis by several orders of magnitude[102,103]. Ras propagates signalling to a variety of pathways and is currently one of the best characterised oncogenes[104–107]. Neurofibromin activity as a key downregulator of Ras activity[56,60,78] naturally got significant attention, arguably disproportionate compared to other putative roles in cellular biology.

The upregulation of RAF/MEK/ERK branch signalling upon *NF1* inactivation is known to promote cell growth and survival[108,109]. Both as prognostic and/or predictor of response to its inhibition, this pathway was widely explored in neurofibroma[110,111] - resulting in the recent FDA approval of selumetinib for inoperable plexiform neurofibromas[112,113] -, and melanomas[114–117] carrying *NF1* alterations. Similar contexts are currently under investigation for lung adenocarcinomas[118,119], where low levels of neurofibromin are associated with resistance to epidermal growth factor receptor (EGFR) TKIs[120]. In BC, *NF1* loss has been mainly associated with MAPK pathway hyperactivation as a resistance mechanism and targeted through different effectors.

In ER^+ BC, loss of *NF1* has been found as one of the most common genetic alterations associated with endocrine resistance[121,122], which arrises both through ER-dependent mechanisms - where *NF1* acts like an ER corepressor through the LRD[122,123] - and associated with MAPK signalling and expression of cyclin D1, with ER-independent S-phase entry[121,124]. The addition of a MEK inhibitor to fulvestrant (a selective estrogen receptor degrader [SERD]) was demonstrated to be effective in *NF1*-silenced or -ablated ER^+ preclinical models. The relation between *NF1* mutations and CDK4/6 inhibition was evaluated both *in vitro* and through ctDNA analysis from patients enrolled in the PALOMA-3 trial[125]. Here, the addition of palbociclib to fulvestrant in patients carrying *NF1* mutations (6.34%) was suggested by the authors as effective on overcoming the worse intrinsic outcomes expected on the mutated cohort. *NF1* alterations were also enriched and associated with endocrine therapy resistance in metastatic invasive lobular carcinoma (ILC), frequently co-occuring with mutations in the

IDH1 gene[126]. In all these settings, mutations of *NF1* were mutually exclusive with *ESR1* or *ERBB2*mutations.

Less evidence is available for HER2$^+$ disease. Smith et al. identified *NF1* as mechanism of acquired resistance to HER2-targeted therapies through the MAPK-MEK-ERK pathway and, diverging from what was manifested in the ER$^+$ context, pointed to CDK2 (with cyclin E amplification) as the mediator of MEK-dependent cell cycle progression[127].

Another well-described hyperactivated Ras downstream pathway is the PI3K/AKT/mTOR. Johannessen et al. [128], Dasgupta et al. and Li et a.l[129] all showed that, in multiple *NF1*-deficient models, the mTOR pathway is constitutively activated[130,131] and is potentially targetable, although mTOR targeting in BC, in general, leads to low response rates and acquired resistance[132–134] through overactivation of multiple compensatory pathways[135–139] and immune evasion[140].

1.2.3.2. NF1 beyond RAS

As seen in neurofibromatosis type 1, some phenotypes cannot be attributed to the Ras hyperactivation (or at least not alone), and studies elucidating the role of other domains and their novel interacting proteins have broadened our understanding of the pleiotropic, Ras-independent effects of *NF1*[100,141]. Neurofibromin was long thought to be only a cytoplasmic protein, with interactions like the one with sprout-related EVH1 domain containing 1 (SPRED1), which negatively regulate Ras/MAPK signaling[142], to be happening mainly at the cell membrane level via phospholipids[143] and caveolin-1[144,145].

The nuclear presence of neurofibromin was first identified in keratinocytes and telencephalic neurons between 2000 and 2001. This observation was later confirmed by Vandenbroucke et al., which identified a NLS present in exon 51, essential for the nuclear import of neurofibromin[83]. In yeast, *NF1* was found to regulate metaphase to anaphase transition in a Ras-independent manner[146] and to associate with the spindle[147,148] upon CTD phosphorylation by protein kinase C (PKC)[149]. In glioblastoma models, neurofibromin was not only present in the nucleus, but distributed by a Ran GTPase gradient in a cell-cycle-dependent fashion for correct chromosome alignment: predominantly extra-nuclear at the G1/S transition, progressively accumulated in the nucleus throughout the S phase, and then became almost completely nuclear just prior to mitosis, gradually declining by the next G1[150,151]. Neurofibromin has also been reported to interact with CRMP2 (*see section 1.3.2*),

syndecans[152–154] - a small family of transmembrane proteoglycans associated with metastatic cellular processes[155,156] -, and the valosin containing protein (VCP)[92] - an AAA+ ATPase central in the regulation of the protein quality control system/secretory pathway[157–159] -, but less is known regarding those functions and their translation to the clinics.

1.3. Evidence for a potential role of *NF1* in the regulation of cytoskeleton dynamics

Dissecting the crosstalk of neurofibromin with the cytoskeleton may be crucial to understand *NF1* role in tumour biology and as a pharmacological biomarker. Specially during mitosis, the progress of spindle formation and cytokinesis lays on an orchestrated morphological and mechanical changes promoted by the coordinated activities of the plasma membrane (PM), the microtubule (MT) and the actin cytoskeleton[160–162] (**figure I7**). In 1993, Bollag G et al. found that tubulin co-purified with neurofibromin in insect cells; interestingly, tubulin decreased neurofibromin Ras-GAP activity[163] in that case, suggesting competition between tubulin and Ras for the same or close binding site. Subsequent studies confirmed colocalisation of neurofibromin with F-actin in growth cones and filopodia of neurons undergoing differentiation[93,164–166]. Although evidence suggests *NF1* activity on both actin and MTs, I will now discuss separately the two cytoskeletal pools. It is important to stress that the vast majority of the studies investigating the connection of *NF1* with the cytoskeleton has been collected in neuroectodermal systems, due to the established involvement of *NF1* in neurofibromatosis-related tumours. Evidence in other tumour types, where *NF1* is more commonly mutated at the somatic level, is scarce, leaving a non-negligible gap for the extrapolation of these findings.

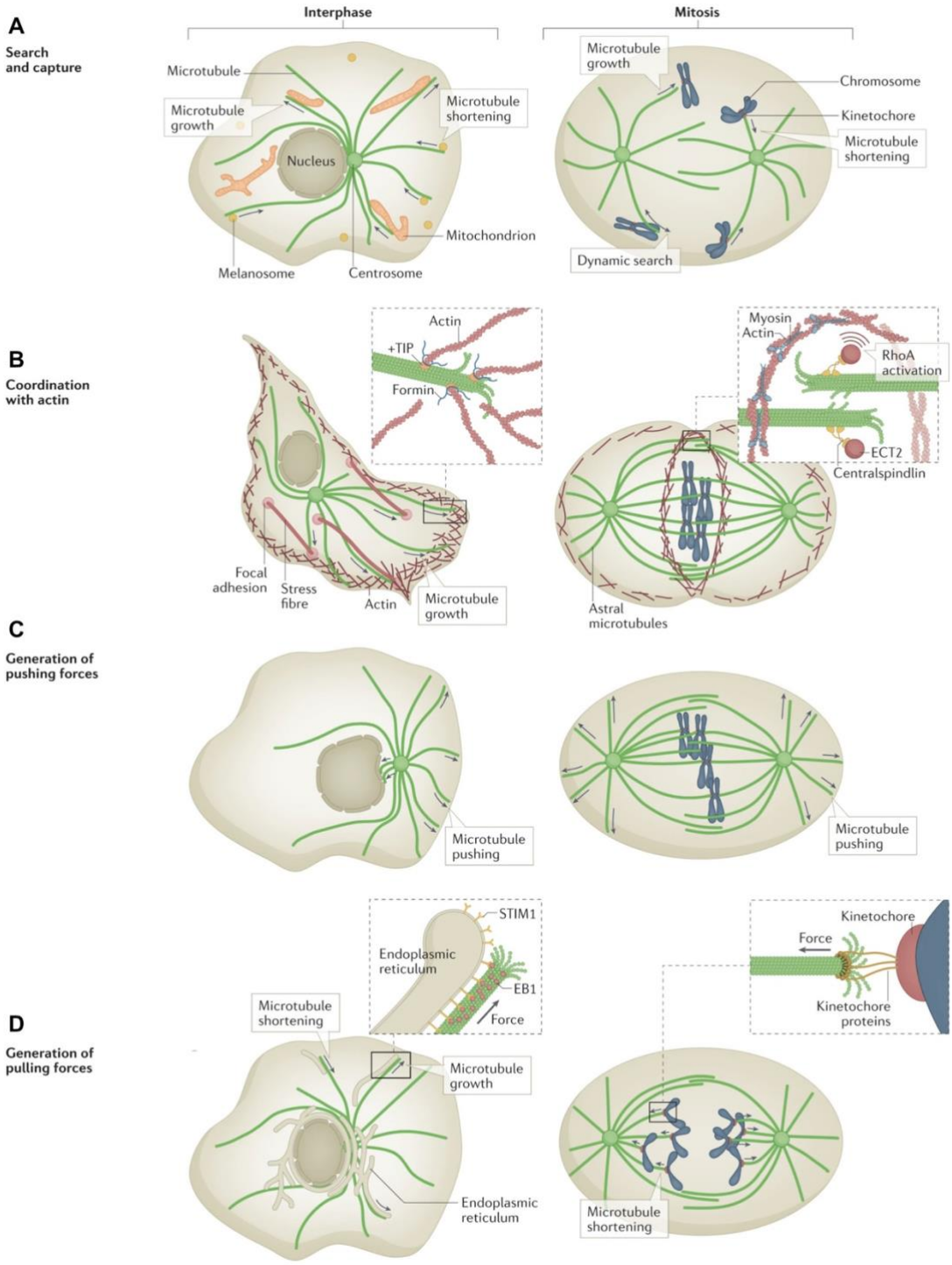

Figure I7. The intimate crosstalk between MTs, actin and the PM throughout the cell cycle. **A.** MTs searching and capturing organelles during interphase and chromosomes during mitosis. **B.** Interactions with focal adhesion structures through the MT plus tip (+TIP) in growing cells while projecting towards the actin cortex to form astral MTs and defining the actomyosin ring position with RhoA partners during mitosis; **C.** MTs exerting cytoplasmic forces to maintain nucleus position and spindle centering during mitosis; **D.** MT plus ends remodelling the ER in interphase and guiding kinetochores through cell division. Adapted from Gudimchuk NB & McIntosh JR[167].

1.3.1. *NF1* and actin

Actin exists in two forms: the monomeric G (globular)-actin and the polymeric F (filamentous)-actin[168], tightly regulated by polymerisation/depolymerisation dynamics. A significantly increase in the association of neurofibromin with actin in co-immunoprecipitation (co-IP) was observed upon EGF-induced PKC phosphorylation of the CSRD domain of *NF1*[166]. Neurofibromin inhibits parallel signaling pathways centered on the phosphorylation of the cofilin family proteins[169]: while the N-terminal (pre-GRD)[170] downregulates the Rac1/Pak1/LIMK1/cofilin pathway, the Sec14/PH domain inhibits the LIM domain kinase 2 (LIMK2) from Rho/ROCK/LIMK2/cofilin. Consistently, LIMK2 was upregulated upon neurofibromin knockdown in HeLa cells, with changes in cell morphology, motility and adhesion[165]. Both pathways play a crucial role in actin cytoskeleton dynamics[171,172]. Neurofibromin also interacts with focal adhesion kinase (FAK) and the loss of this interaction leads to increased adherence to collagen and fibronectin matrices in mouse embryonic fibroblast (MEFs), with FAK and actin redistributing towards the cell leading edge[173]. In MEF 3D cultures, FAK hyperactivation due to *NF1* loss increased phosphorylation of the downstream effectors Src, ERK and AKT and resulted in increased colony formation. Combinatorial treatment with the FAK inhibitor defactinib and the MEK inhibitor selumetinib fully suppressed colony growth[174]. Additionally, increased FAK mRNA levels is a frequent finding in ovarian and BC patients with poor survival outcomes[175,176].

1.3.2. *NF1* and microtubules

Neurofibromin interacts with tubulin dimers/polymers apparently through two different domains. First evidences of this interaction were mapped, in fact, to a domain defined as the "tubulin-binding domain" (TBD) and shown to decrease the *NF1* Ras-GAP activity[164]. Conversely, selected GRD mutations compromised the ability of neurofibromin to associate with MTs[177]. Debate still exists on a possible functional overlap between GRD and TBD since (i) the TBD is only a few aa upstream from the GRD and (ii) residues important for p21-Ras regulation seemed also required for microtubule binding[177]. This evidence dates back to the mid 1990s and no further clarification emerged over time. Neurofibromin also localises to the mitotic spindle (α- and β-tubulin) and to the centrosome (γ-tubulin), during both mitosis and interphase[150,151] in neuroectodermal cells. These interactions, on the other hand, were

shown to be mediated by the CTD and suggests that different components of *NF1* affect different cytoskeletal functions, based on cell state. Distinction between a direct interaction of neurofibromin on MT stabilisation *versus* the need for complexing with other MT associated proteins (MAPs) is yet an unresolved question.

MTs are characterised by dynamic instability. Protofilaments, made of α/β-tubulin heterodimers, are in continuous longitudinal and lateral remodeling. In a stochastic process - more frequent at the growing, plus end but also at the shortening minus end[178] - they independently alternate between phases of disassembly and assembly known as catastrophe and rescue, respectively, in fast-pacing cycles[179]. This biological phenomenon is essential for MTs to exert their roles within eukaryotic cells (i.e.: differentiation, growth, vesicle transport, motility, cell division). The mechanics and kinetics of MTs are spatially and temporally modulated in essence by the rate of GTP hydrolysis[180–183], their interplay with MAPs[179,184–186], and tubulin post-translational modifications (PTMs)[187,188]; the latter are likely less relevant for interaction with *NF1* and will not be discussed further.

- The α/β-tubulin dimers have a nucleotide exchangeable site (E-site) exposed in the β subunit, which renders them competent for polymerisation/depolymerisation by switching from GTP to GDP; and a nonexchangeable (N-site) buried within the intra-dimer interface, constitutively occupied by GTP[189]. The GTP bound to the E-site gets hydrolysed during polymerisation to form GDP-Pi and create an MT consisting largely of GDP-tubulin[190–192]. GDP-tubulin is more unstable than GTP-tubulin and more likely to depolymerise. Due to hydrolysis delay, a small region of GTP/GDP-Pi-tubulin dimers, called “GTP cap,” remains at the plus end of the MT and is thought to stabilise it against depolymerisation. Once the GTP-tubulin cap is lost, rapid shrinking is observed[190]. Nonetheless, “islands” of non-hydrolysed GTP-tubulin can remain embedded within the lattice of the polymerised MT and have been observed in both *in vivo* and *in vitro* systems. These GTP islands have been proposed to slow down or stop depolymerisation altogether and allow the conversion of a shortening to a growing MT[193,194]. This idea has also been supported by recent results suggesting that GTP enriched regions are dynamic structures themselves, responsible for rapid on-off kinetics that could facilitate MT regrowth[195–197]. Tubulin has intrinsic, low GTPase activity[198] and its activation normally occurs when the tubulin dimer binds to the end of a growing MT[189]. Additionally, many

MAPs (*see below*) are known to interact differently with MTs depending on the bound nucleotide[199]. MAPs capability of sensing a conformational change is well documented (i.e.: tau[200], end-binding proteins[201], kinesins[180,202]), but just recently reported to also trigger tubulin-GTP hydrolysis[203]. It remains poorly understood, however, how tubulin conformational transitions from curved (single protofilaments or unpolymerised) to straight (expanded or compacted, in the MT body) and/or GTP/GDP states may impact on the affinity for specific MT targeting agents (MTAs)[204–206] (**figure I8 B, C**).

- Neurofibromin is known to associate with dynein and kinesins[207–209], though the downstream consequences of this interaction are poorly understood. Kinesins - a superfamily of microtubular motor proteins[210] - have been recently uncovered to not only act as mere cargo transporters but also to regulate MT dynamics, especially during mitosis[211,212]. Kinesin 1 (KIF5b) indirectly carries catalytic enzymes and the GTP exchange factor Rho-GEF[213]; kinesin-13s (KIF2a/b/c[MCAK])[214] and kinesin 8 (KIF19a)[215] have depolymerisation capabiltites towards the stable GTP cap of growing MTs[216–219]; and kinesin-8 (KIF18a) either prevents the assembly of GTP tubulin or depolymerises GTP-islands within the MT lattice[220,221]. During mitosis, Eg-5 (KIF11)[222–225], kinesin 12 (KIF15)[226,227] and KIF18a/b[228–231] also play an essential part on kinetochore-MT attachment, bipolar spindle formation and chromosome segregation. For most of these kinesins there is evidence on their correlation with tumour progression and response when targeted in BC[232], colorectal cancer[233], and glioblastoma[234] preclinical models. Another MAP partner of *NF1* is the collapsin response mediator protein 2 (CRMP2). Neurofibromin was first found to interact with CRMP2 for scopes of guiding axonal outgrowth[235,236], but recent evidence is unveiling its role as MT assembly promoter and determinant of taxane activity in preclinical models[237]. When unphosphorylated, CRMP2 binds both to tubulin dimers - transferring them to the plus end of MTs[238] - or to mature MTs for stabilisation[239]. The presence of neurofibromin dampens CRMP2 phosphorylation mainly by the two-step hit from cyclin-dependent kinase 5 (CDK5) and

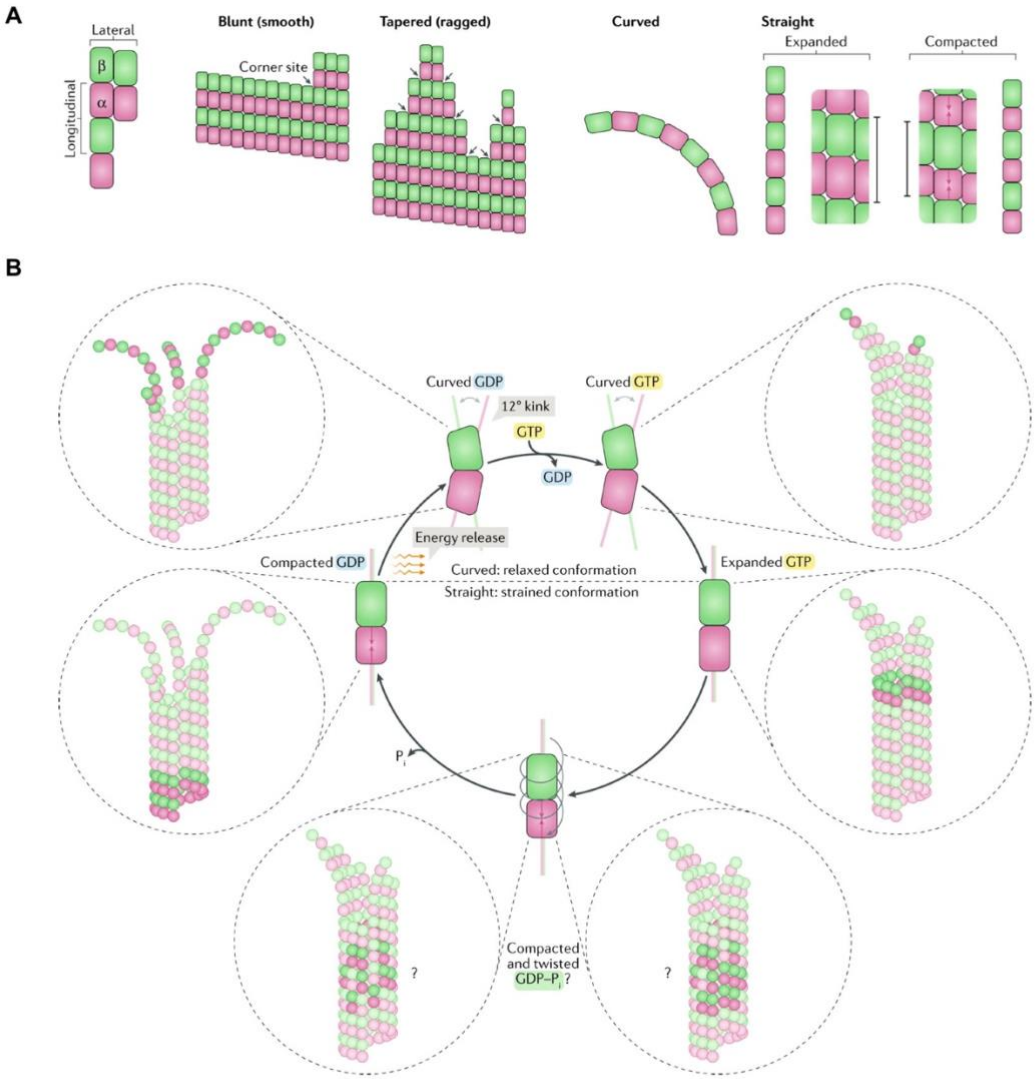
A
Lateral
Longitudinal
β
α
Blunt (smooth)
Corner site
Tapered (ragged)
Curved
Straight
Expanded
Compacted
B
Curved GDP
12° kink
Curved GTP
GTP
GDP
Energy release
Compacted GDP
Curved: relaxed conformation
Straight: strained conformation
Expanded GTP
Pi
Compacted and twisted GDP–Pi ?
?
?

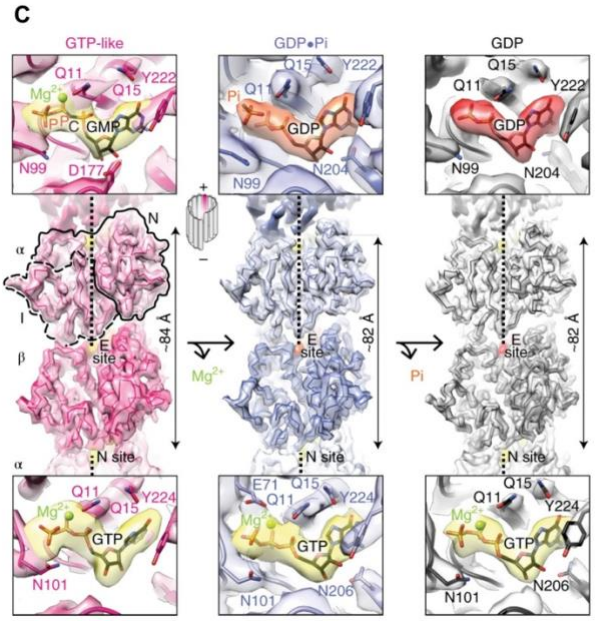
C
GTP-like
GDP•Pi
GDP
Q11
Y222
Q15
Mg2+
GMPCPP
GMP
GDP
Pi
N99
D177
N204
N
α
β
I
E site
N site
~84 Å
~82 Å
Mg2+
Pi
Q11
Y224
GTP
N101
E71
N206

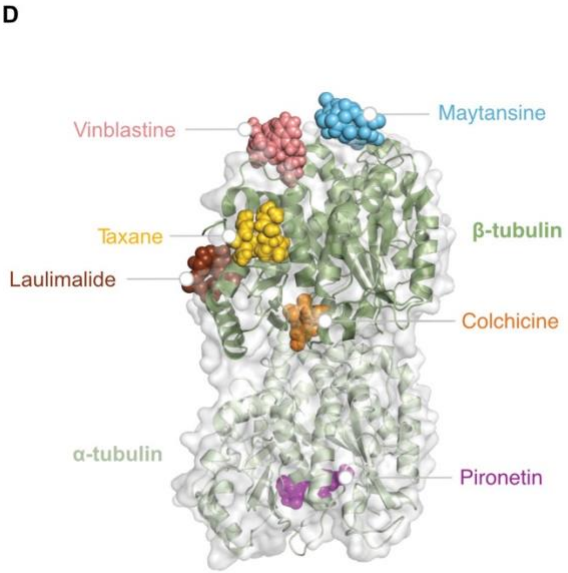
D
Vinblastine
Maytansine
Taxane
β-tubulin
Laulimalide
Colchicine
α-tubulin
Pironetin

Figure I8 (*previous page*). A. The different architectures assumed by α/β-tubulin polymers and **B, C.** how they cycle between conformations according to the nucleotide occupying the E-site and their interaction with the MT lattice; **D.** MTAs binding sites. Representation of the α/β-tubulin dimer with biding sites for maytansine (PDB-ID 4TV8, light blue), vinblastine (PDB-ID 5J2T, pink), taxane (PDB-ID 5LXT, gold), laulimalide (PDB-ID 4O4H, brown), colchicine - fitting at the intra-dimer interface (PDB-ID 4O2B, orange), and pironetin (PDB-ID 5LA6, purple) - the only characterised MTA binding to an α-tubulin site. Modified from Brouhard GJ & Rice LM[240], Manka SW & Moores CA[186], and Eli S et al.[241]

---

glycogen synthase kinase 3β (GSK-3β)[242], keeping it on active state and fostering MT growth[236]. Its phosphorylation levels, but not expression, have been positively linked to cancer progression[243,244]. Moutal et al. observed an inverse correlation between *NF1* expression and CRMP2 phosphorylation, where low neurofibromin was determinant of higher CRMP2 phosphorylation levels and proliferation of human glioblastoma cell lines; while inhibiting CRMP2 phosphorylation led to *in vivo* tumour response[245]. The CDK5/GSK-3β/CRMP2 pathway has been extensively studied in the context of neuropathic pain in neurofibromatosis type 1 patients[246,247].

2. Results

2.1. *NF1* as a biomarker for T-DM1 sensitivity

2.1.1. *NF1* is the most differentially mutated gene in metastatic *versus* primary HER2$^+$ BC

This project was initiated with the intent to unbiasedly identify genes associated with metastatic progression in HER2$^+$ BC. In the specific context of HER2$^+$ disease, metastasis-enriched genes may also be involved in resistance to anti-HER2 antibodies, since virtually all patients diagnosed between 2010 and 2018 would have received trastuzumab in the adjuvant setting.

We pooled publicly available datasets of BC sequencing (TCGA[53], enriched for primary lesions and both the MSK-MET[54] and the AACR-GENIE[52] for mBC) and compared frequencies of mutated genes in primary (n = 1066) *vs* metastatic cases (n = 1048 and n = 1418 for MSK-MET and the AACR-GENIE, respectively) in the overall cohorts and in the *ERBB2*-amplified subgroups. Since the HER2 clinical status, ascertained as per ESMO/ASCO/St. Gallen guidelines with IHC and FISH, is often unreported or unreliable, we decided to define HER2 positivity based on copy number data obtained directly from NGS. Odds ratio (OR) were calculated as the ratio of gene frequencies in metastatic versus primary cohorts, and genes with less than 5% of mutated samples - considered poorly informative - were excluded from multiple hypothesis correction to avoid false-negatives due to false discovery rate (FDR) overcorrection. Considering all BC subtypes, *NF1* did not reach the 5% threshold of mutated samples but it reaches a significant higher OR in the metastatic setting compared to primary (3.5 *vs* 6.1 and 5.7%; OR = 1.76 and 1.66; p = 8.04 x 10^{-3} and 1.07 x 10^{-2}, respectively, for the MSK-MET and the AACR-GENIE; Fisher's exact test). In the *ERBB2* amplified subgroup, *NF1* was the second most significant gene differentially mutated between metastatic and primary patients, after *TP53* (2.5 *vs* 9.3 and 8.5%; OR = 4.08 and 3.67; p = 2.80 x 10^{-2} and 3.24 x 10^{-2}, Fisher's exact test; FDR adj p = 0.098 and 0.097, respectively, for the MSK-MET and the AACR-GENIE; **figure R1A, B** and **figure A1**). The spectrum of mutations included 188 and 259 loss-of-function (LoF) and nonsense mutations for primary and metastatic samples, respectively, in a scattered pattern across domains, typical of a tumour suppressor gene[248,249] (**figure R1C, D**).

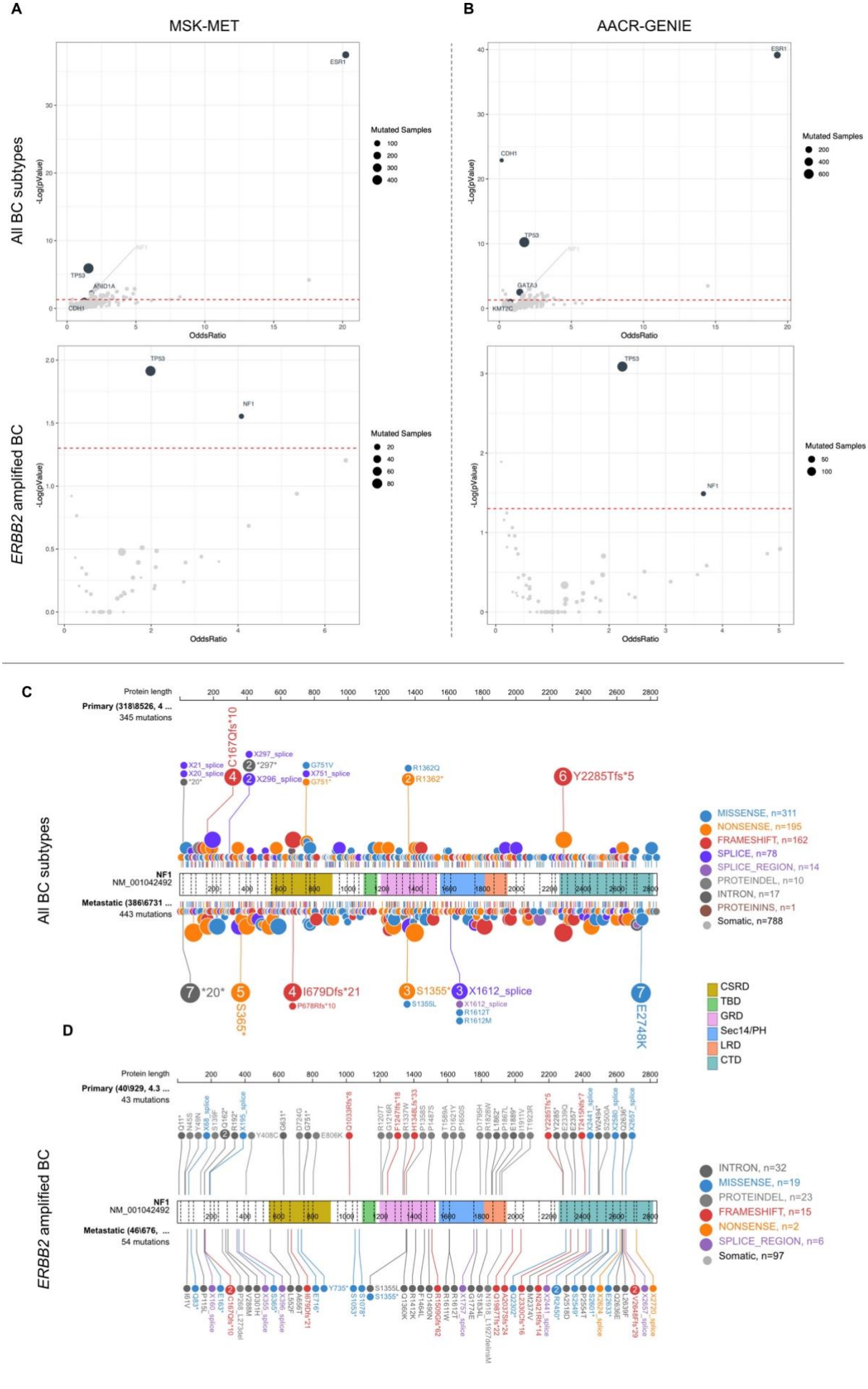
A
MSK-MET
B
AACR-GENIE
All BC subtypes
ERBB2 amplified BC
-Log(pValue)
OddsRatio
Mutated Samples
ESR1
TP53
NF1
ARID1A
CDH1
GATA3
KMT2C
C
D
Protein length
Primary (318\8526, 4 ...
345 mutations
Metastatic (386\6731 ...
443 mutations
Primary (40\929, 4.3 ...
43 mutations
Metastatic (46\676, ...
54 mutations
NF1
NM_001042492
C167Qfs*10
X297_splice
X21_splice
X20_splice
20
297
X296_splice
G751V
X751_splice
G751*
R1362Q
R1362*
Y2285Tfs*5
20
S365*
I679Dfs*21
P678Rfs*10
S1355*
S1355L
X1612_splice
R1612T
R1612M
E2748K
MISSENSE, n=311
NONSENSE, n=195
FRAMESHIFT, n=162
SPLICE, n=78
SPLICE_REGION, n=14
PROTEINDEL, n=10
INTRON, n=17
PROTEININS, n=1
Somatic, n=788
CSRD
TBD
GRD
Sec14/PH
LRD
CTD
INTRON, n=32
MISSENSE, n=19
PROTEINDEL, n=23
FRAMESHIFT, n=15
NONSENSE, n=2
SPLICE_REGION, n=6
Somatic, n=97

Figure R1 (*previous page*). A, B. Comparison of mutational frequency in unmatched metastatic *vs* primary tumours from all subtypes (top) or *ERBB2* amplified (bottom) BC. Primary samples were taken from TCGA and metastatic samples from MSK-MET and AACR-GENIE. Plots depict OR *vs* -log p value of mutation frequency; 0.05 was used as threshold for p value (red dotted line). We used the Benjamini-Hochberg procedure to control the FDR at 0.25 (>0.25 = grey, ≤0.25 = black), excluding mutations with an overall frequency <5%; **C, D.** Lollipop plots generated using the AACR-GENIE cohort v13.0-public samples. Mutations are divided according to distribution in primary (top) *vs* metastatic (bottom) tumours, from all subtypes and *ERBB2* amplified samples.

2.1.2. Generation of *NF1* knockout HER2$^+$ BC cell lines

To investigate the biological consequences of *NF1* loss in HER2$^+$ BC, we generated multiple *NF1* knockout clones of the widely used HER2$^+$ BC cell line BT-474, SK-BR3 and HCC1954 by means of CRISPR/Cas9. We validated the results by western blot (**figure R2A**) and NGS (**figure R2B**). Protein loss was confirmed with a panel of anti-neurofibromin antibodies that recognise distinct epitopes throughout the protein, all demonstrating a complete loss of signal. Throughout the present study, we used BT-474 cells for exploratory experiments and then validated our findings on SK-BR3 and/or HCC1954 cells. HCC1954 cells were also used for xenograft models due to their superior efficiency in generating growing masses *in vivo* within a short time frame and without the need of exogenous hormone supplementation (required by BT-474). We explored two orders of hypotheses, based on the assumptions detailed above: the involvement of *NF1* in pharmacological sensitivity to agents used in HER2$^+$ BC, explored in sections 2.1 and 2.2, and in the metastatic process, explored in section 2.3.

2.1.3. *NF1* ablation leads to overall resistance to anti-HER2 agents but exquisite sensitivity to maytansinoids

We subjected BT-474 wild type (BT-474^{WT}) and *NF1* knockout (BT-474^{KO}) cells to a pharmacological screen with the main currently European Medicines Agency (EMA)/United States Food and Drug Administration (FDA)-approved HER2-targeting agents and their chemotherapy companions (**Figure R3**).

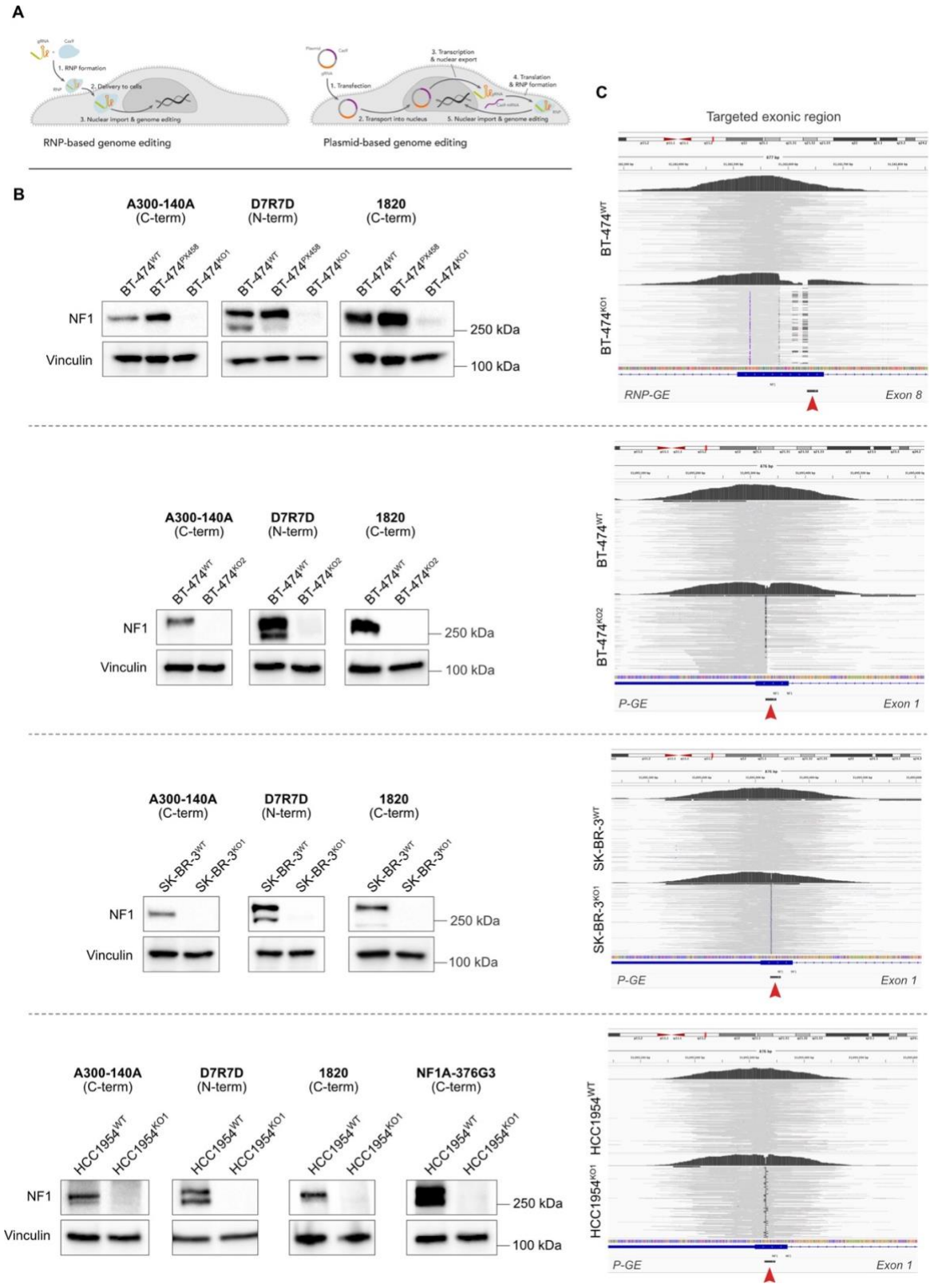

Figure R2. A. Schematic illustration of the ribonucleoprotein (RNP)- and plasmid-based CRISPR/Cas9 techniques utilised for generating the *NF1*KO clones. Modified from Integrated DNA Technologies, Inc. ©2022; **B.** Thorough evaluation of multiple antibodies against different immunogens of neurofibromim showing complete protein absence in BT-474, SK-BR-3 and HCC1954 cells; **B.** NGS of

all clones used in the current manuscript, compared to parental. Panels are zoomed in the locus region according to *NF1*sgRNA (red arrowhead), from Integrative Genomics Viewer (IGV). Data were generated together with A Castiglioni, an undergraduate within the lab, and analysed with G Frigè, a staff scientist at the Department of Experimental Oncology, European Institute of Oncology, Milan, using the Illumina DRAGEN Bio-IT Platform v4.0.

We decided to use a BrdU incorporation-based assay and not an ATP-based one such as CellTiter-Glo® as the former showed a superior dynamic range (not shown). For trastuzumab, pertuzumab, T-DXd, lapatinib and paclitaxel, IC_{50} values were higher or equivalent in BT-474^{KO} compared to BT-474^{WT}, supporting the idea of *NF1*-associated resistance to standard HER2-targeting agents - in particular to pertuzumab and lapatinib. However, we unexpectedly found a lower IC_{50} in response to T-DM1 (1.55 µg/mL in BT-474^{WT} *vs* 0.24 µg/mL in BT-474^{KO}). Resistance to HER2-targeting agents was also recently demonstrated by Smith et al.[127], whereas a relationship between *NF1* and T-DM1 remains unexplored to the best of our knowledge, so we decided to further pursue this finding.

In longer-term (8 days) culture and colony formation assays (CFA), the difference between WT and KO cells in terms of T-DM1 response was pronounced, in all cell lines tested (**figure R4**). In a competitive setting, which we generated by co-culturing H2B-GFP-labelled BT-474^{WT} cells and H2B-mCherry-labelled BT-474^{KO} cells, a T-DM1-induced KO-specific disadvantage became significant as early as day three (**figure R5A**).

An analysis of apoptotic markers revealed a clear increase in PARP cleavage and reduction of antiapoptotic Bcl-2 in WB at 48h in BT-474^{KO} cells compared to BT-474^{WT}. Propidium iodide (PI)-based cell cycle assessment showed a significant increase in T-DM1-induced G2/M arrest in KO cells (OR = 2.09 and 1.58 for 0.2 and 4 µg/mL, respectively) (**Figure R5C**), which could also be visibly appreciated as an increase of rounded up cells through phase microscopy (**Figure R5D**).

A

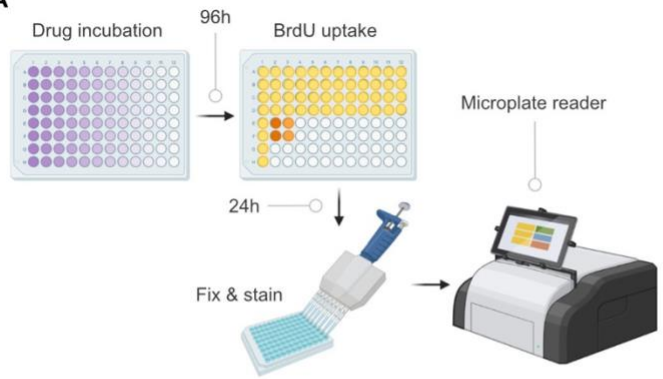

	IC_{50}	
	BT-474^{WT}	BT-474^{KO}
Trastuzumab	12.5 µg/mL	12.6 µg/mL
Pertuzumab	0.47 µg/mL	1.43 µg/mL
Lapatinib	0.095 µM	0.165 µM
Pacitaxel	3.8 µM	4.04 µM
T-DXd	0.035 µg/mL	0.033 µg/mL
T-DM1	1.55 µg/mL	0.24 µg/mL

B

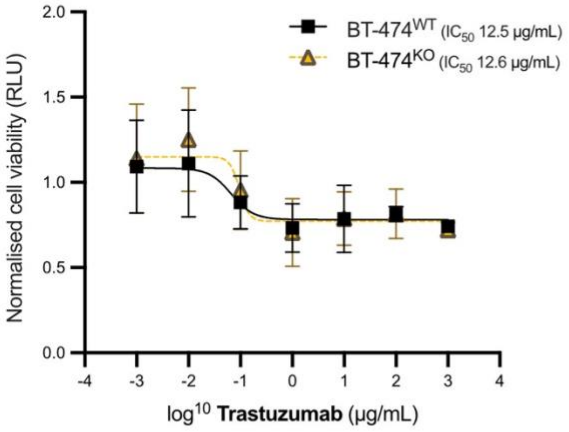

C

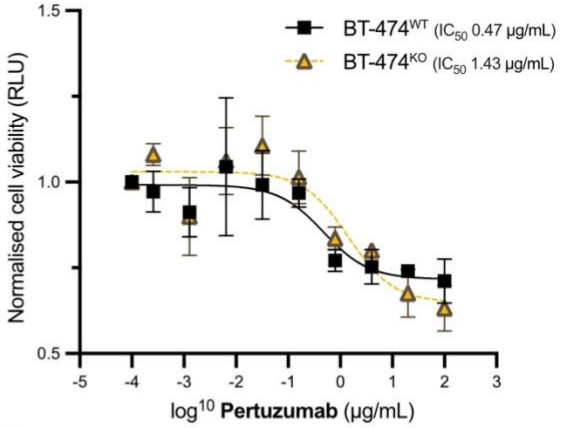

D

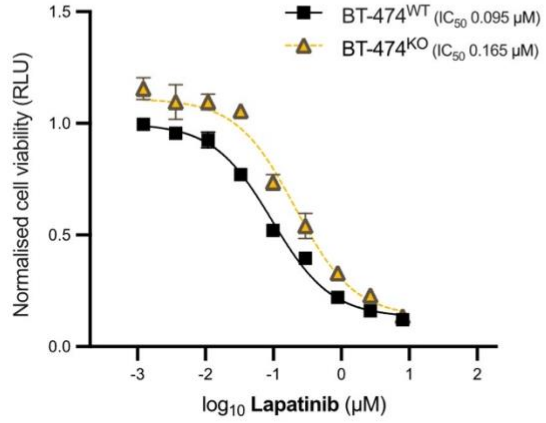

E

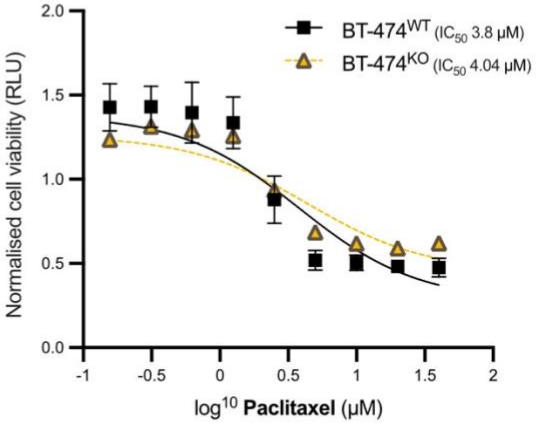

F

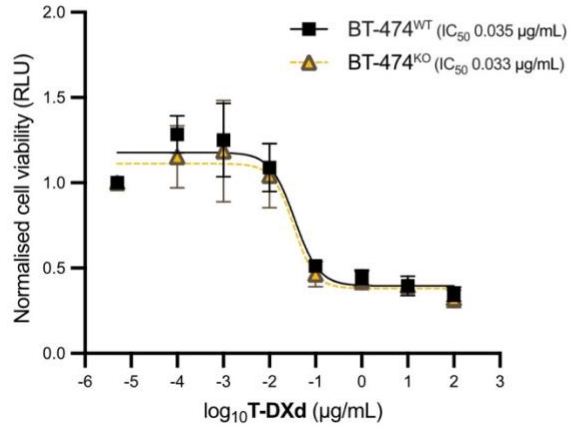

G

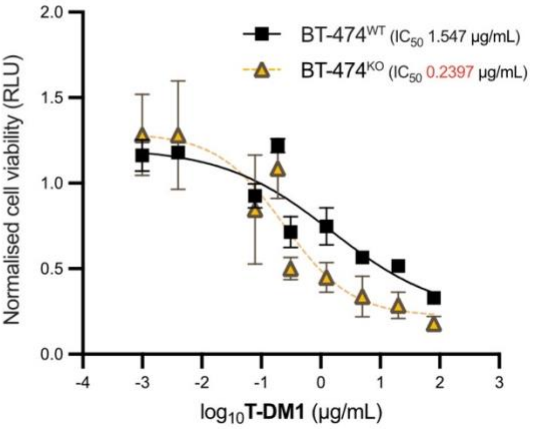

Figure R3 (*previous page*). A. Schematic of high-throughput BrdU-incorporation screening, with **B.** summary of IC_{50} values; **C-G.** Viability curves of key agents with their respective IC_{50} after four days of treatment plus 24h of BrdU incorporation. Data represents mean ± SD from at least three independent experiments.

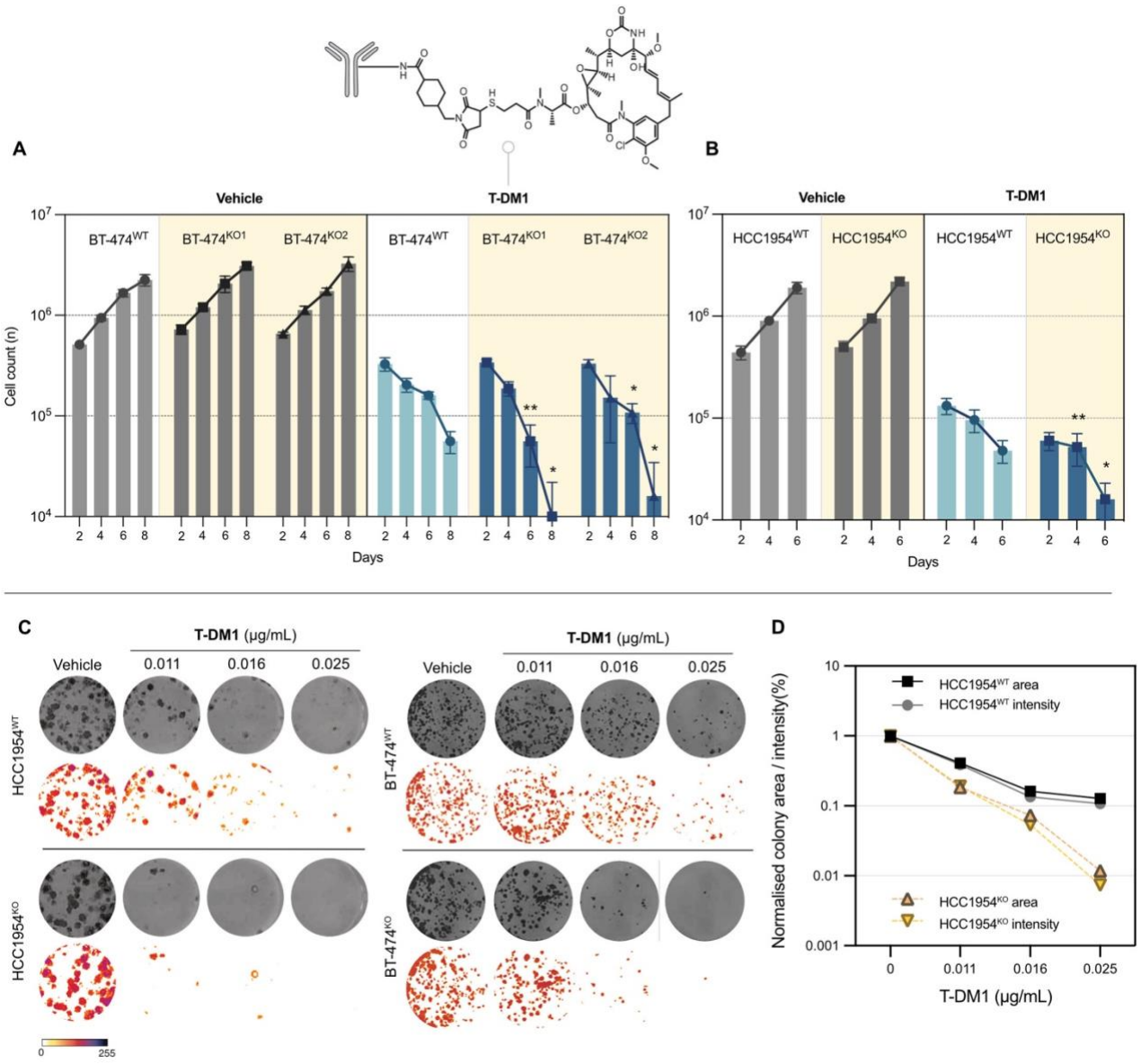

Figure R4. A, B. 6-8-days growth curves with T-DM1 on BT-474 and HCC1954 cells. Rituximab, a human IgG1 monoclonal antibody, was used as control. Multiple unpaired *t*-tests were performed, p is represented for each time point (* $p \leq 0.05$; ** $p \leq 0.01$); **C.** CFA for HCC1954 and BT-474 cell lines. Single cell suspensions were plated at very low densities and, before the first mitosis, incubated with IgG1 control or T-DM1 at anti-clonogenic concentrations. 8-bit greyscale images of individual wells and same individual wells after thresholding and background removal by the

Colony_thresholder macro (ColonyArea ImageJ plugin[250]). Scale bar represents the intensity displayed in the thresholded wells. Zero intensity (white) corresponds to areas where no cells were identified (background); **D.** Area covered by remaining colonies and their respective intensity.

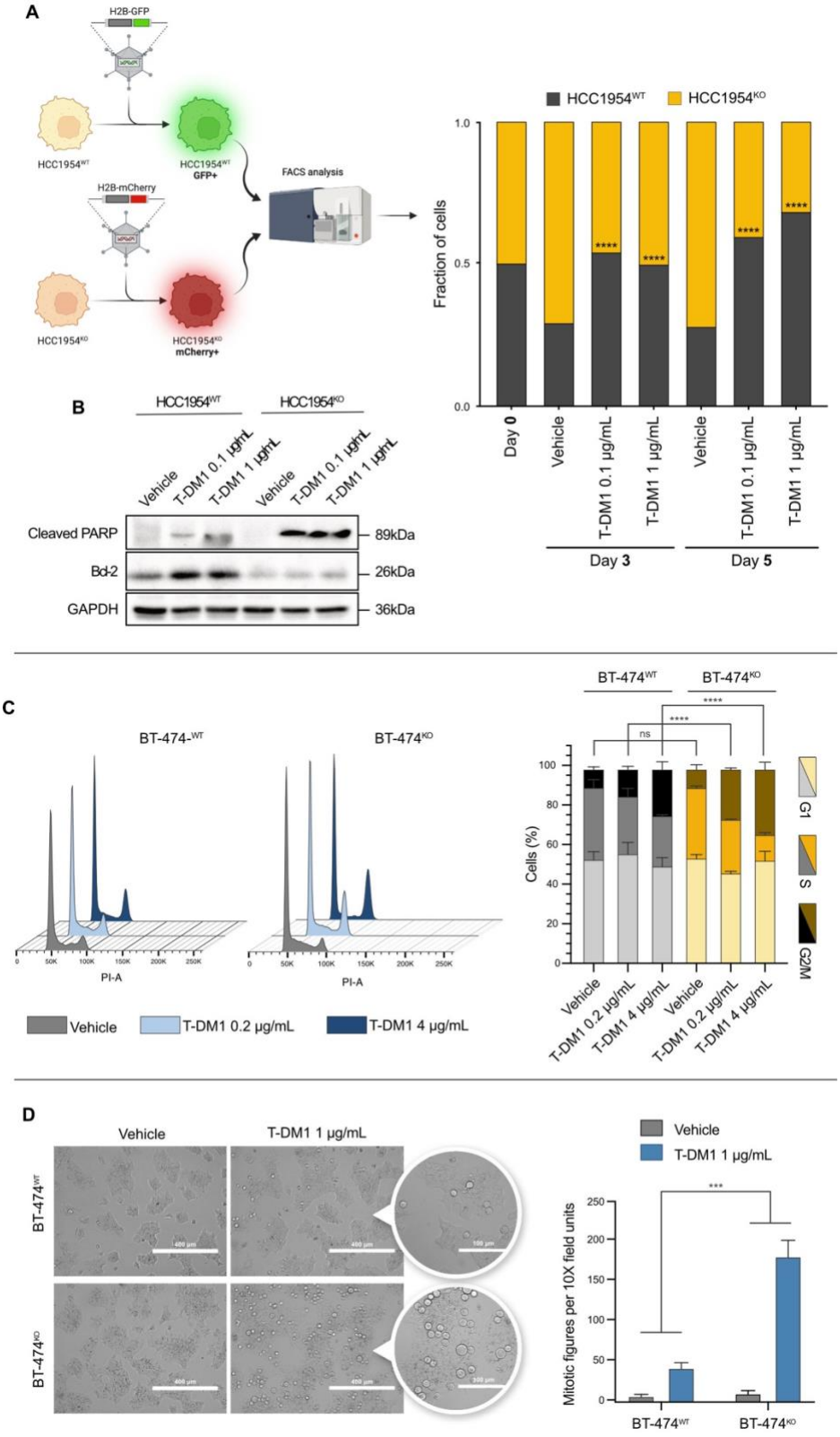

Figure R5 (*previous page*). A. HCC1954^{WT} and HCC1954^{KO} engineered to express H2B-GFP and H2B-mCherry, respectively, were co-cultured at a 1:1 ratio, with or without the addition of T-DM1. At days three and five, cells were trypsinised and the living mixed cell suspension was analysed via FACS for viability and cell cycle (not shown); **** $p < 0.0001$, $\chi 2$ test); **B.** Whole cell lysates of HCC1954^{WT} and HCC1954^{KO} blotted for cleaved PARP and Bcl-2 at 48h after T-DM1 treatment; **C.** Propidium-iodide (PI) cell cycle analysis after 36h of T-DM1 at the indicated doses; **** $p < 0.0001$, $\chi 2$ test; error bars are SD. Data was reproducible with other cell lines (not shown); **D.** A significant increase in round-up figures on BT-474^{KO} cells, indicative of ongoing mitosis, can be observed in phase contrast microscopy (EVOS® FL Cell Imaging System) after 24h of T-DM1 treatment; $p = 0.0004$, Fisher's exact test; error bars are SD.

2.1.4. T-DM1 sensitivity is not induced by oncogenic Ras signaling and does not correlate with increased drug internalisation

Efficacy or resistance to ADCs may be explained by different orders of biological processes, so we performed a series of experiments aimed at narrowing down possible alternative hypotheses. First, we investigated different pharmacological aspects of T-DM1 that may lead to increased or impaired efficacy. T-DM1 is subject to receptor-mediated internalisation and trafficking to the lysosomes, processes mediated by caveolin - a known neurofibromin interactor[144,145] - and modulated by mTOR signaling[251]). We observed no difference on internalisation rates of T-DM1 nor T-DXd after 24h of lysosomal activity blockade with chloroquine (CQ) ($p = 0.70$ and $p = 0.18$, respectively; Student's *t*-test, two-tailed) (**figure R6**), ruling out the hypothesis that *NF1*KO-induced T-DM1 sensitivity be due to increased internalisation. On the other hand, treatment with the naked payload DM1 showed clear hypersensitivity in long-term cultures and CFA, whereas no difference between BT-474^{KO} and BT-474^{WT} cells was observed with trastuzumab alone nor T-DXd (**figure R7**). To directly study the interaction of DM1 with its pharmacological target in living cells, we used the cellular thermal shift assay (CETSA),[252,253254] a thermodynamic stabilisation assay used to infer the strength of drug-target interaction. Peptide binding stability of naked DM1 to β-tubulin during thermal denaturation was significantly increased in BT-474^{KO} cells *vs* BT-474^{WT} **(figure R8)**. By performing a two-way ANOVA, we observed that temperature factor is significant for both BT-474^{WT} and BT-474^{KO} ($p = 2.05 \times 10^{-12}$ and 1.79×10^{-9}, respectively). However, the addition of treatment is significant only for BT-474^{KO} ($p = 0.00462$) and not for BT-474^{WT} ($p = 0.78$). Thus, we can safely conclude that *NF1* loss leads to increased sensitivity specifically to DM1.

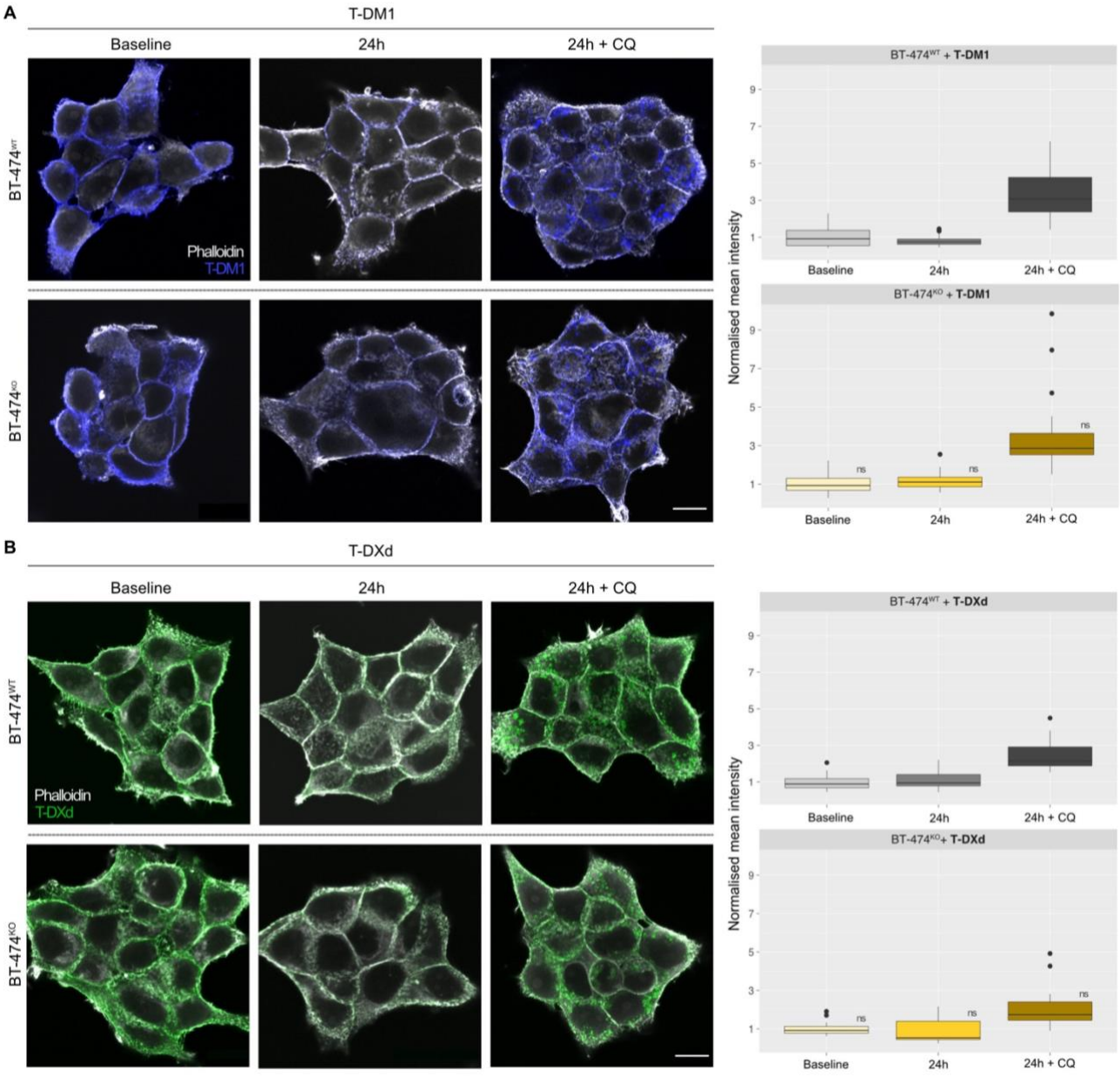

Figure R6. Immuno-confocal microscopy showing equivalent internalisation rates of both **A.** T-DM1 and **B.** T-DXd in BT-474^{KO} cells. Phalloidin (grey), T-DM1 (blue), T-DXd (green). Scale bar = 20 µm. CQ, chloroquine (5 µM). At least 28 cells were analysed per genotype. Data were generated and analysed together with A Castiglioni, an undergraduate within the lab, and S Freddi, a physicist staff scientist at the Department of Experimental Oncology, European Institute of Oncology, Milan.

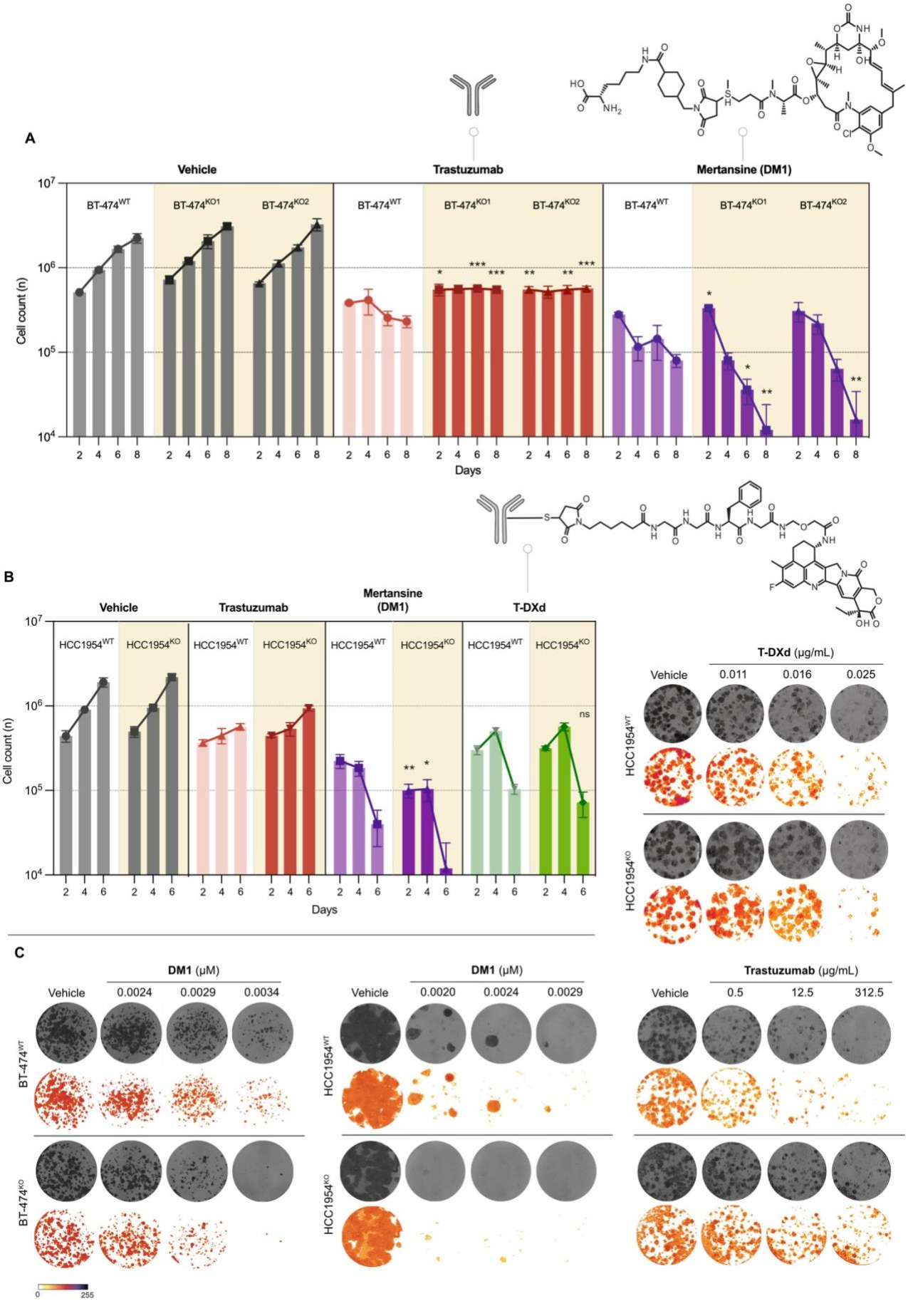
A
Vehicle
Trastuzumab
Mertansine (DM1)
BT-474WT
BT-474KO1
BT-474KO2
Cell count (n)
Days
B
Vehicle
Trastuzumab
Mertansine (DM1)
T-DXd
HCC1954WT
HCC1954KO
Cell count (n)
Days
ns
T-DXd (μg/mL)
Vehicle
0.011
0.016
0.025
C
DM1 (μM)
Vehicle
0.0024
0.0029
0.0034
0.0020
Trastuzumab (μg/mL)
0.5
12.5
312.5
0
255

Figure R7 (*previous page*). A, B. 6-8-days growth curves and **C.** CFA with trastuzumab, DM1 and T-DXd on HCC1954 and BT-474 cells. Experimental conditions identical to the ones previously described in *figure 4*.

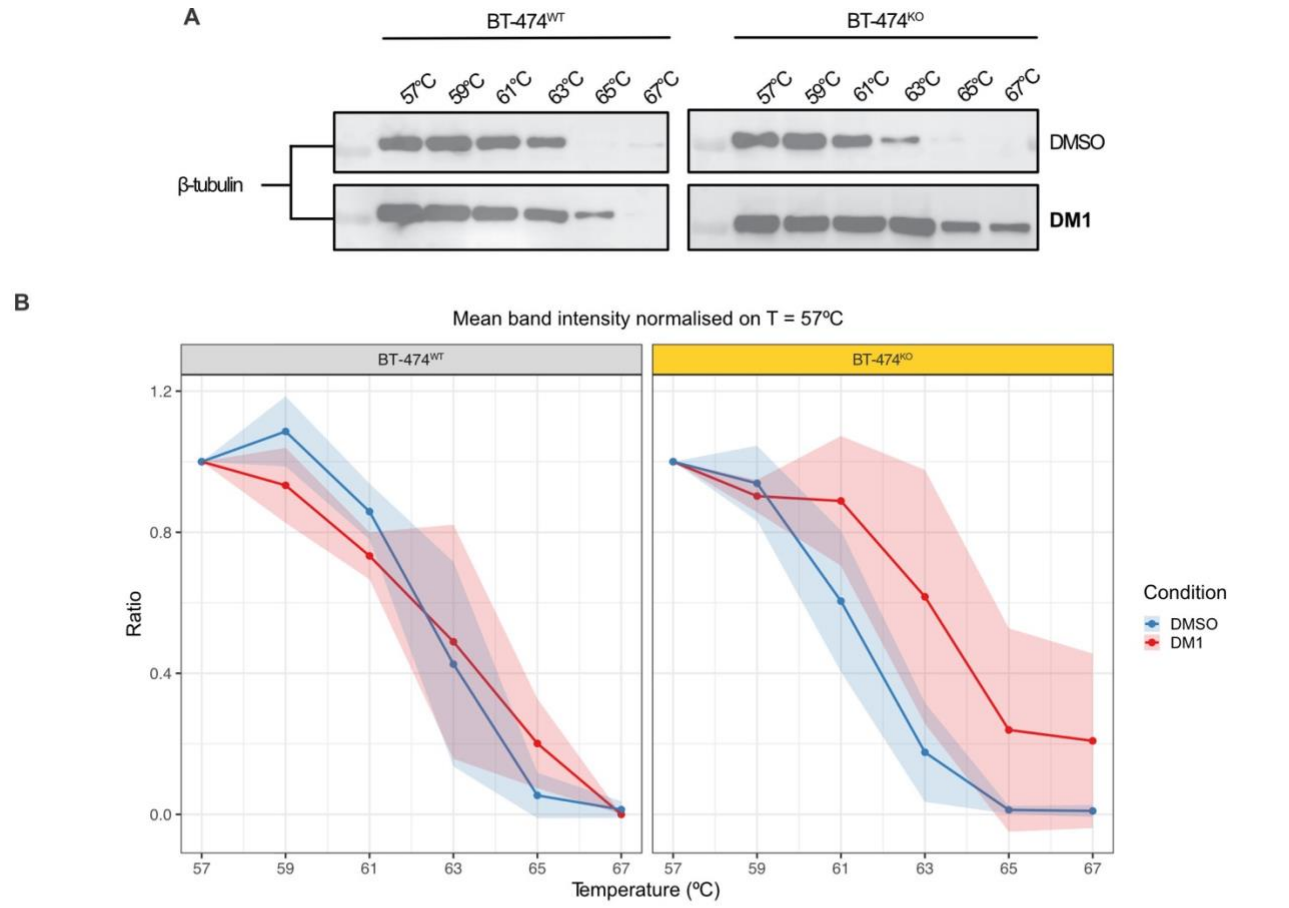

C

BT-474^{WT}

	Df	Sum Sq	Mean Sq	F value	Pr(>F)
Treatment	1	0.002	0.0016	0.080	0.780
Temperature	5	5.726	1.1452	55.611	2.05e-12 ***
Treatment: Temperature	5	0.096	0.0192	0.932	0.478
Residuals	24	0.494	0.0206		

BT-474^{KO}

	Df	Sum Sq	Mean Sq	F value	Pr(>F)
Treatment	1	0.310	0.3103	9.756	0.00462 **
Temperature	5	4.656	0.9313	29.283	1.79e-09 ***
Treatment: Temperature	5	0.241	0.0481	1.513	0.22306
Residuals	24	0.763	0.0318		

Figure R8. CETSA. **A.** western blot for β-tubulin of cell extracts from BT-474^{WT} and BT-474^{KO} cells incubated with DM1 for 2h and then exposed to increasing temperatures as indicated. **B.** Quantification of band intensities from CETSA western blots (n = 3 independent experiments), normalised on baseline signal at 57°C. Ribbons indicate SD; **C.** Results from two-way ANOVA separately performed on BT-474^{WT} and BT-474^{KO} normalised data. Data were generated and analysed together with E Messuti, a junior PhD student and G Tini, a postdoc mathematician within the lab.

Secondly, we assessed if oncogenic Ras signaling could phenocopy *NF1* loss. In active Ras pulldown assays (**figure R9A**), we observed a variable impact of *NF1* ablation on the Ras activation state: although BT-474^{KO} and, to a lesser extent, SK-BR3^{KO} cells showed increased signals of GTP-bound Ras compared to their parental counterparts, this was not evident in HCC1954 cells (**figure R9B**), suggesting that *NF1* loss does not necessarily lead to Ras hyperactivation, even in cells that show hypersensitivity to T-DM1. To directly investigate whether oncogenic Ras activation could phenocopy *NF1* loss, we generated BT-474 cells stably expressing the KRAS^{G12V} mutant (BT-474^{G12V}), which showed the expected constitutive Ras hyperactivation (**figure R9C**). Long-term growth curves, however, showed no increased sensitivity of BT-474^{G12V} cells (**figure R9D**). These results indicate that oncogenic Ras activation per se does not induce T-DM1 hypersensitivity, suggesting that the *NF1*KO phenotype may be independent of its activity on Ras inhibition.

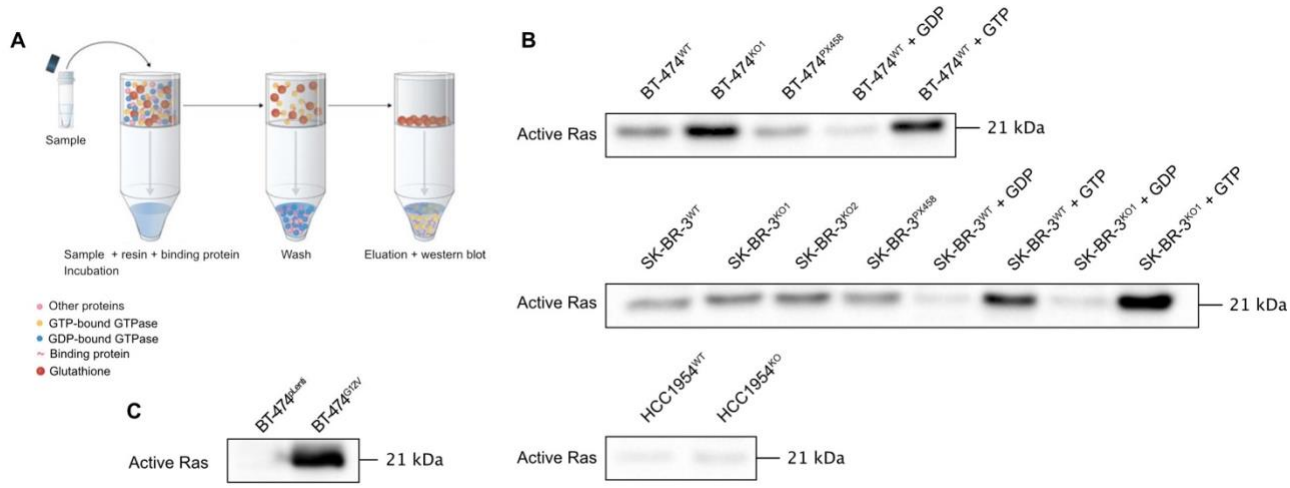

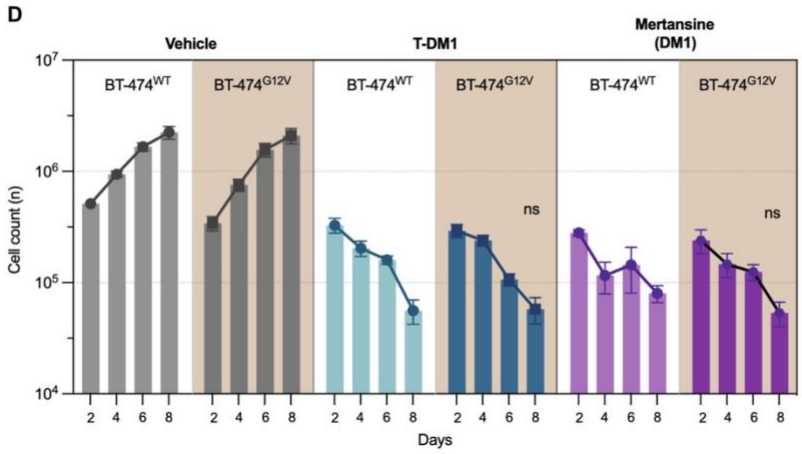

Figure R9. A. Active Ras pull-down in **B.** BT-474, SK-BR-3 and HCC1954 cells; **C.** $KRAS^{G12V}$ overexpression in BT-474 cells; **D.** 8-days growth curves with T-DM1 on BT-474^{WT} and BT-474^{G12V} cells.

2.1.5. T-DM1 induces enhanced tumour regression in *NF1*KO mouse xenograft models and possibly prolongs progression-free survival (PFS) in *NF1* mutated, heavily pretreated $HER2^+$ mBC patients

To validate the translational relevance of our results, we directly compared the efficacy of T-DM1 in xenografts concomitantly bearing WT and *NF1*KO $HER2^+$ human BC tumours. $HCC1954^{WT}$ and $HCC1954^{KO}$ cells were engineered to express the firefly luciferase (FLuc) gene and injected in the right and left inguinal mammary fat pads, respectively, of 9-weeks old NOD-SCID-γ (NSG) mice (**figure R10A**). At day 14, tumours were assessed for baseline bioluminescence imaging (BLI), and did not show significant differences between $HCC1954^{WT}$ and $HCC1954^{KO}$ lesions. Mice were randomly treated intravenously with 4 mg/kg of T-DM1 or vehicle control (n = 10 per treatment group). Significant differences in T-DM1-induced tumour regression, both in terms of size and radiance, were already evident at the first time point (day 19) (**figure R10B, C**). The growth of $HCC1954^{KO}$ tumours remained significantly lower on the T-DM1 cohort throughout the observation period up to day 35, without any weight loss (**figure A2**, **Appendix**). Available tumour specimens are currently being processed and will be analysed for IHC, IF, and RNA-seq.

For further translational validation, we analysed a cohort of 406 mBC patients with available mutational data in ctDNA obtained through the Guardant360 NGS-based platform[255]. Data were obtained in collaboration with Prof. M Cristofanilli and P D'Amico at the Northwestern University (NWU). We identified 13 HER2+ patients who received T-DM1 in the advanced setting (> 4 prior lines of therapy). Patients at earlier stages were excluded in order to match clinical features between $NF1^{MUT}$ and $NF1^{WT}$ patients, since all $NF1^{MUT}$ patients received T-DM1 beyond the 4^{th} line (**figure** R**10D**). Three out of 13 patients had *NF1* mutations, and showed a trend favouring a longer PFS (median 334 *vs* 80 days, HR 0.4, p = 0.14; **figure R10E, F**). These data cannot yet be considered conclusive due to the small sample size and we plan to supplement the analysis with additional prospectively enrolled patients.

In conclusion, our results show that *NF1* genetic loss, a frequent occurrence in $HER2^+$ mBCs (~10% of the cases), is associated with significantly increased sensitivity to T-DM1. This appears to be independent of the activation of oncogenic Ras signaling and specifically due to DM1 activity.

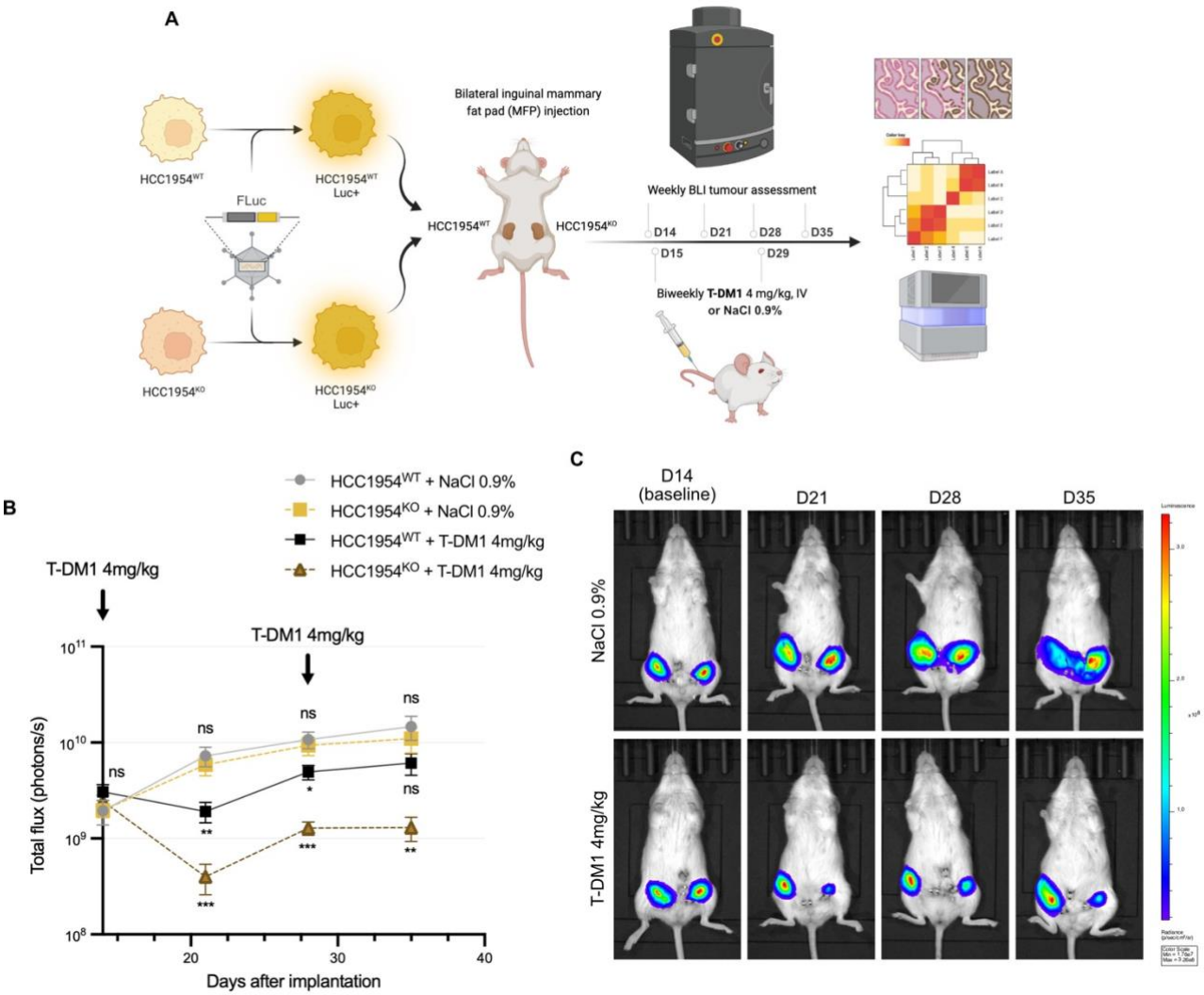
A
HCC1954WT
HCC1954WT Luc+
FLuc
HCC1954KO
HCC1954KO Luc+
Bilateral inguinal mammary fat pad (MFP) injection
HCC1954WT
HCC1954KO
Weekly BLI tumour assessment
D14
D21
D28
D35
D15
D29
Biweekly T-DM1 4 mg/kg, IV or NaCl 0.9%
B
HCC1954WT + NaCl 0.9%
HCC1954KO + NaCl 0.9%
HCC1954WT + T-DM1 4mg/kg
HCC1954KO + T-DM1 4mg/kg
T-DM1 4mg/kg
T-DM1 4mg/kg
Total flux (photons/s)
Days after implantation
ns
*
**
***
C
D14 (baseline)
D21
D28
D35
NaCl 0.9%
T-DM1 4mg/kg
D
406 mBC
47 received T-DM1
29 received T-DM1 after 3rd line
13 had corresponding ctDNA available
10 NF1WT
3 NF1MUT
E
Progression Free Survival (PFS) on T-DM1
NF1WT
NF1MUT
Days
F
NF1WT
NF1MUT
Probability of survival (%)
p = 0.14
Days

Figure R10 (*previous page*). A. Experimental design and **B.** growth of HCC1954^{WT} and HCC1954^{KO} xenograft mammary tumours treated biweekly with IV vehicle or T-DM1 (4 mg/kg); n = 10 mice per group, means of total flux (photons/s) with SD are plotted. At the latest time point, p = ns for HCC1954^{WT} and 0.0322 for HCC1954^{KO}, Student's *t*-test; **C, D.** Identification of 13 patients who received T-DM1 in the advanced metastatic setting (> 4 prior lines of therapy): the 3 out of 13 patients carrying *NF1* mutations showed a trend for longer PFS (p = 0.14); stratified by *NF1* status through liquid biopsy (Guardant Health). Data was generated together with D Tosoni, a group leader, N Roda, a postdoc, and A Polazzi, all from the Department of Experimental Oncology, European Institute of Oncology, Milan.

2.2. *NF1* loss impairs microtubule dynamics

2.2.1. *NF1*KO cells exhibit more prominent signs of mitotic catastrophe than *NF1*WT upon T-DM1 treatment

As discussed in *section 1.1.2*, DM1 interferes with longitudinal protofilament interactions of β-tubulin, inhibiting MT dynamic instability and arresting cells in G2/M by preventing correct kinetochore attachment and mitotic spindle assemblage. This series of events would ultimately lead to mitotic catastrophe, which has been proposed as a strategy of higher eukaryotes for eradicating mitosis-incompetent cells - by death or senescence - and preserve genome stability[256]. The data presented in *section 1* strongly suggest that *NF1* may play a role in mitosis, that may not be evident during unperturbed 2D growth but that becomes key in determining hypersensitivity to T-DM1. This hypothesis was further supported by the analysis of RNA-seq data of cells harvested at 36h after T-DM1 treatment (**figure R11A-D**). Gene Ontology (GO) pathways functionally relevant for mitosis and structurally related to MTs and the mitotic spindle were the most differentially regulated upon T-DM1 treatment between BT-474^{KO} and BT-474^{WT} cells. When clustered over the Hallmark Mitotic Spindle signature, these genes recapitulate the intrinsic transcriptional differences between unperturbed BT-474^{KO} and BT-474^{WT} cells, most evidently in clusters 2 and 3 **(Figure R11E)**. Cell cycle, kinesins (BioPlanet), centriole duplication and separation, G2/M phase transition, spindle assembly (Elsevier Pathway Collection), axon guidance (KEGG) and signaling by Rho GTPases (Reactome) were the top significantly associated terms downregulated in BT-474^{KO} (custer 2), implying a likely NF1*KO*-specific additive effect.

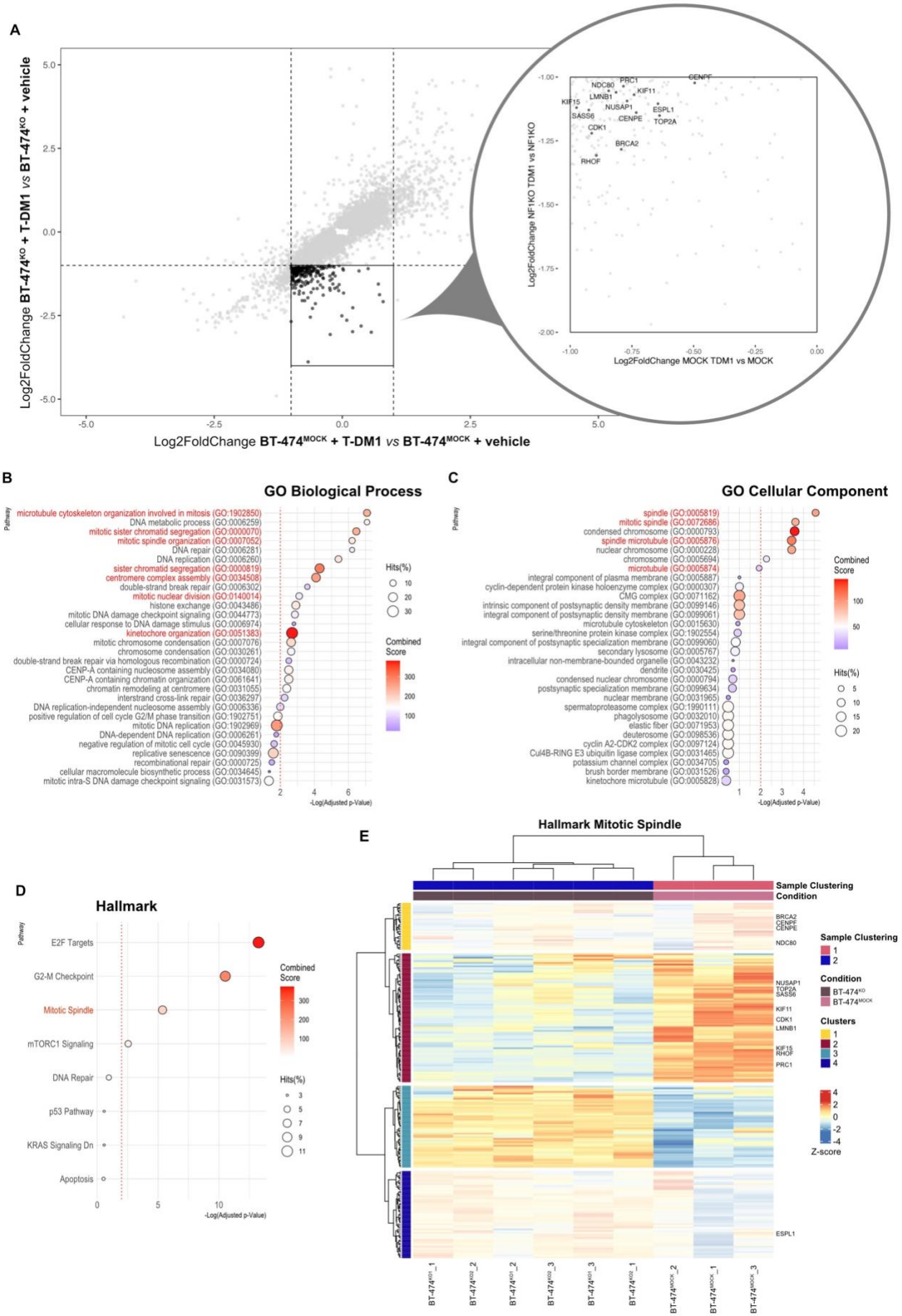
A
Log2FoldChange BT-474KO + T-DM1 vs BT-474KO + vehicle
Log2FoldChange BT-474MOCK + T-DM1 vs BT-474MOCK + vehicle
Log2FoldChange NF1KO TDM1 vs NF1KO
Log2FoldChange MOCK TDM1 vs MOCK
NDC80
PRC1
CENPF
KIF11
LMNB1
KIF15
NUSAP1
ESPL1
SASS6
CENPE
TOP2A
CDK1
BRCA2
RHOF
B
GO Biological Process
microtubule cytoskeleton organization involved in mitosis (GO:1902850)
DNA metabolic process (GO:0006259)
mitotic sister chromatid segregation (GO:0000070)
mitotic spindle organization (GO:0007052)
DNA repair (GO:0006281)
DNA replication (GO:0006260)
sister chromatid segregation (GO:0000819)
centromere complex assembly (GO:0034508)
double-strand break repair (GO:0006302)
mitotic nuclear division (GO:0140014)
histone exchange (GO:0043486)
mitotic DNA damage checkpoint signaling (GO:0044773)
cellular response to DNA damage stimulus (GO:0006974)
kinetochore organization (GO:0051383)
mitotic chromosome condensation (GO:0007076)
chromosome condensation (GO:0030261)
double-strand break repair via homologous recombination (GO:0000724)
CENP-A containing nucleosome assembly (GO:0034080)
CENP-A containing chromatin organization (GO:0061641)
chromatin remodeling at centromere (GO:0031055)
interstrand cross-link repair (GO:0036297)
DNA replication-independent nucleosome assembly (GO:0006336)
positive regulation of cell cycle G2/M phase transition (GO:1902751)
mitotic DNA replication (GO:1902969)
DNA-dependent DNA replication (GO:0006261)
negative regulation of mitotic cell cycle (GO:0045930)
replicative senescence (GO:0090399)
recombinational repair (GO:0000725)
cellular macromolecule biosynthetic process (GO:0034645)
mitotic intra-S DNA damage checkpoint signaling (GO:0031573)
Pathway
Hits(%)
Combined Score
-Log(Adjusted p-Value)
C
GO Cellular Component
spindle (GO:0005819)
mitotic spindle (GO:0072686)
condensed chromosome (GO:0000793)
spindle microtubule (GO:0005876)
nuclear chromosome (GO:0000228)
chromosome (GO:0005694)
microtubule (GO:0005874)
integral component of plasma membrane (GO:0005887)
cyclin-dependent protein kinase holoenzyme complex (GO:0000307)
CMG complex (GO:0071162)
intrinsic component of postsynaptic density membrane (GO:0099146)
integral component of postsynaptic density membrane (GO:0099061)
microtubule cytoskeleton (GO:0015630)
serine/threonine protein kinase complex (GO:1902554)
integral component of postsynaptic specialization membrane (GO:0099060)
secondary lysosome (GO:0005767)
intracellular non-membrane-bounded organelle (GO:0043232)
dendrite (GO:0030425)
condensed nuclear chromosome (GO:0000794)
postsynaptic specialization membrane (GO:0099634)
nuclear membrane (GO:0031965)
spermatoproteasome complex (GO:1990111)
phagolysosome (GO:0032010)
elastic fiber (GO:0071953)
deuterosome (GO:0098536)
cyclin A2-CDK2 complex (GO:0097124)
Cul4B-RING E3 ubiquitin ligase complex (GO:0031465)
potassium channel complex (GO:0034705)
brush border membrane (GO:0031526)
kinetochore microtubule (GO:0005828)
Pathway
Combined Score
Hits(%)
-Log(Adjusted p-Value)
D
Hallmark
E2F Targets
G2-M Checkpoint
Mitotic Spindle
mTORC1 Signaling
DNA Repair
p53 Pathway
KRAS Signaling Dn
Apoptosis
Pathway
Combined Score
Hits(%)
-Log(Adjusted p-Value)
E
Hallmark Mitotic Spindle
Sample Clustering
Condition
BRCA2
CENPE
CENPF
NDC80
NUSAP1
TOP2A
SASS6
KIF11
CDK1
LMNB1
KIF15
RHOF
PRC1
ESPL1
Sample Clustering
Condition
Clusters
Z-score
BT-474KO_1
BT-474KO_2
BT-474KO_2
BT-474KO_3
BT-474KO_3
BT-474KO_1
BT-474MOCK_2
BT-474MOCK_1
BT-474MOCK_3

Figure R11 (*previous page*). A. Genes with the most altered expression after T-DM1 treatment between BT-474^{KO} and BT-474^{MOCK}, sorted by log2FC; **B-D.** GO (Biological Process, Cellular Component and Hallmark) bubbleplots of the 30 top ranked pathways differentially deregulated between BT-474^{KO} and BT-474^{MOCK} upon T-DM1 treatment. Pathways are raked in decreasing order of -$\log_{10}$ adjusted p value. Bubbles are coloured by combined score from high (red) to low (blue) values. The score is obtained by the combination of the p value (Fisher's exact test) with the normalised z-score following the formula: $c = \log(p) \cdot z$[257], where c is the combined score, p is the p value and z is the z-score. Red dashed line represents the adjusted p value significance threshold (0.01 -log10 = 2). The size of the bubbles is proportional to the percentage of positive hits in the signature; **E.** Hierarchical clustering analysis has been done using the gene expression values from Hallmark Mitotic Spindle molecular signature. Specifically, we used Ward's criterion for genes with 1 - (correlation coefficient) as a distance measure. Three technical replicates were used for each condition. Data were analysed together with E Bonetti, a bioinformatics PhD student within the lab.

We then decided to investigate in depth the cell cycle alterations possibly associated with *NF1* loss and T-DM1 activity. We took advantage of the FUCCI(Ca) reporter, which allows real-time monitoring of progression of cells though G1, S, and G2/M phases[258] by quantifying the abundance of mVenus and mCherry fluorescent proteins expressed under the promoter of licensing factors Cdt1 and its inhibitor Geminin, which are alternately expressed during the cell cycle. Using time-lapse microscopy, we observed that BT-474^{KO} cells were characterised by a baseline prolonged permanence in G2/M (fraction of time spent in G2/M 24.8 *vs* 17.9%, $p = 1.81 \times 10^{-7}$). In agreement with flow cytometry data, treatment with T-DM1 led to a more significant G2/M arrest in BT-474^{KO} cells (28.6 *vs* 21.3%; $p = 1.85 \times 10^{-10}$ at 0.1 µg/mL and 33 *vs* 28.8%, at 1 µg/mL; $p = 1.58 \times 10^{-13}$ at 1 µg/mL, **figure R12A, B**). In addition, T-DM1-induced cell death (measured by a fluorescent DNA dye in the same experiment) was more common in BT-474^{KO} cells: 21.38 *vs* 10.6% for the lower dose and 23.21 *vs* 15.06% for the higher dose (**figure R12C, D)**. Cells tended to die during mitosis or right after re-entry in G1 (qualitative visual assessment, quantification is ongoing). After 90h, residual BT-474^{KO} cells treated with T-DM1 more frequently developed a flat, enlarged morphology and stained more strongly for β-galactosidase activity (**figure R13**), both hallmarks of treatment-induced senescence, a well-established consequence of mitotic catastrophe[256,259].

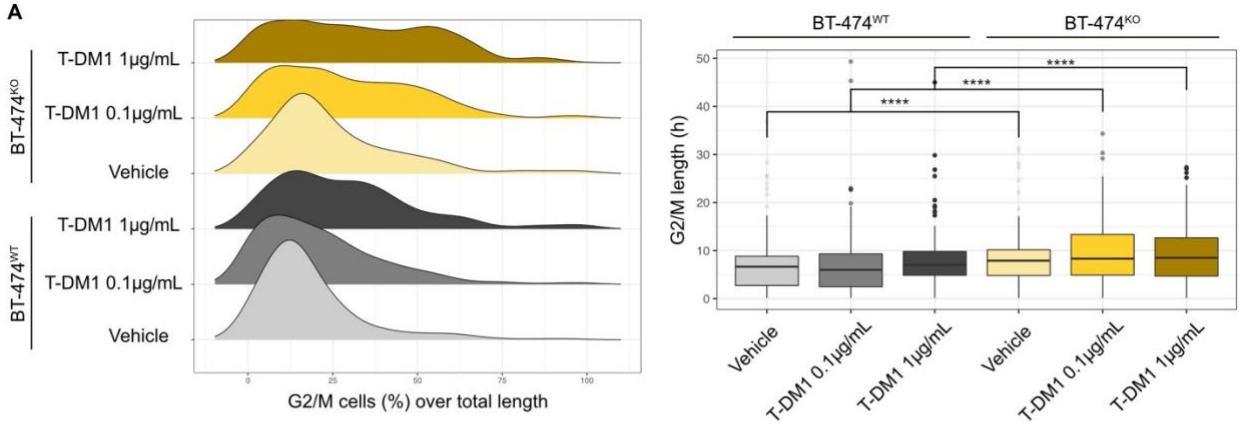

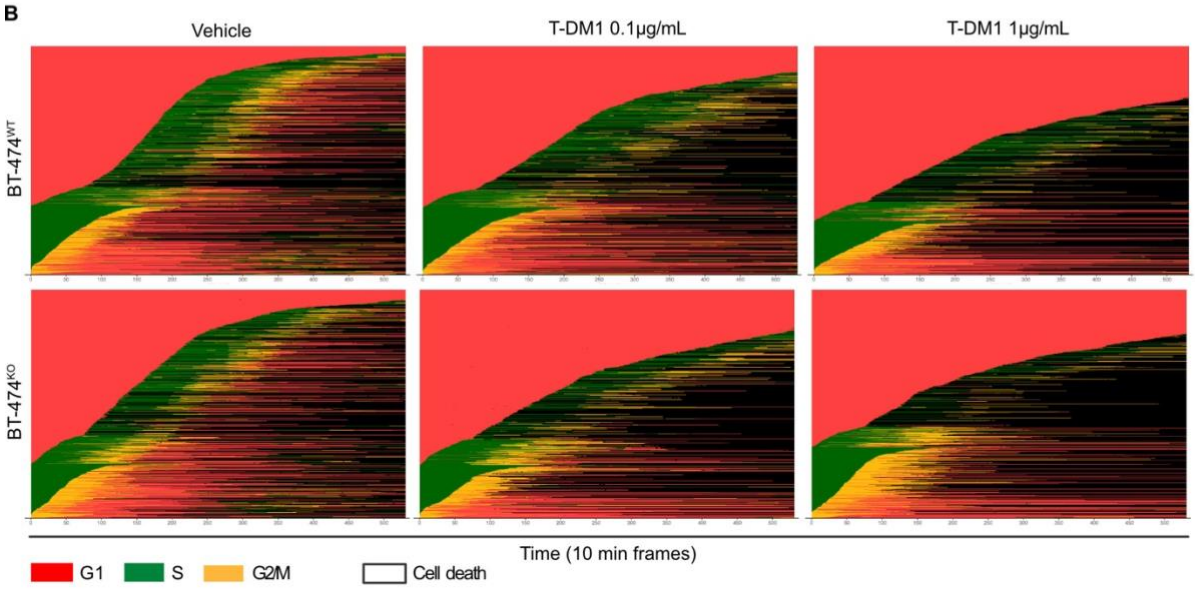

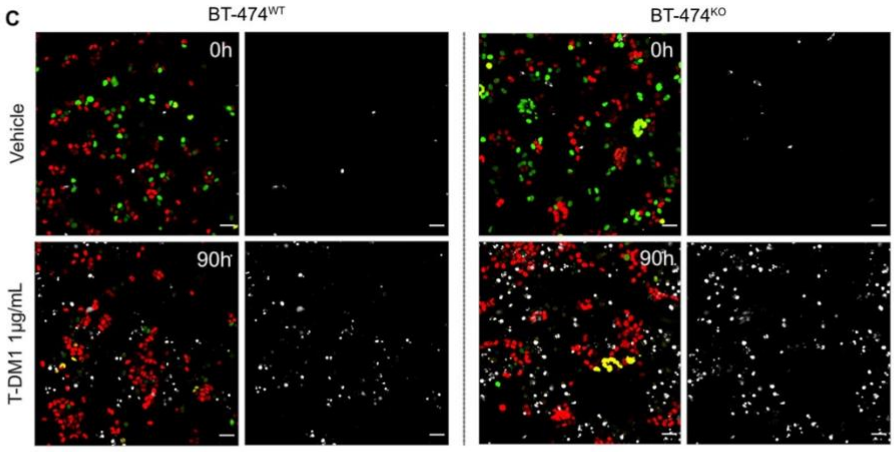

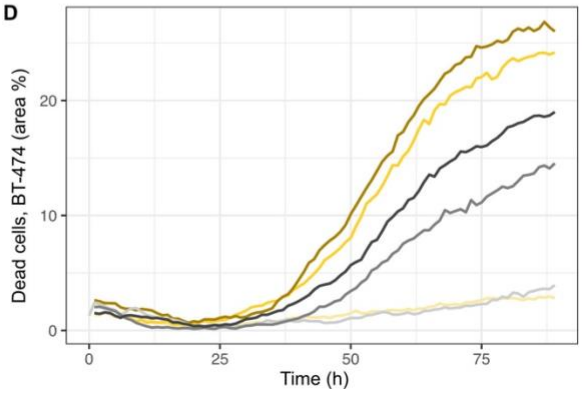

Dead cells (area %)	Vehicle	T-DM1 0.1 µg/mL	T-DM1 1 µg/mL	
BT-474WT	2,42	2,03	1,52	Frame 1
BT-474KO	1,35	2,40	2,64	
BT-474WT	3,94	14,54	19	Frame 90
BT-474KO	2,80	24,18	26,01	

Figure R12 (*previous page*). A. Ridgeline and box plots showing the distribution and quantification of cell fraction according to time spent in G2/M phase of BT-474^{WT} and BT-474^{KO} cells upon T-DM1 treatment; **B.** Cell fate analysis of 200 cells/condition during 90h of T-DM1 exposure, showing a reduction in proliferating cells, longer G2/M arrest and higher G1 prevalence across time in BT-474^{KO} cells compared to BT-474^{WT}; **C.** G1 (red), S (green) G2/M (yellow), and DRAQ7™ (white) - a live-cell impermeable, far-red emitting DNA dye that marks for cell death - are represented at 0h and 90h; **D.** Cell viability curves through time. Data was analysed together with G Tini, a postdoc mathematician within the lab and C Soriani, a physicist staff scientist from the Department of Experimental Oncology, European Institute of Oncology, Milan.

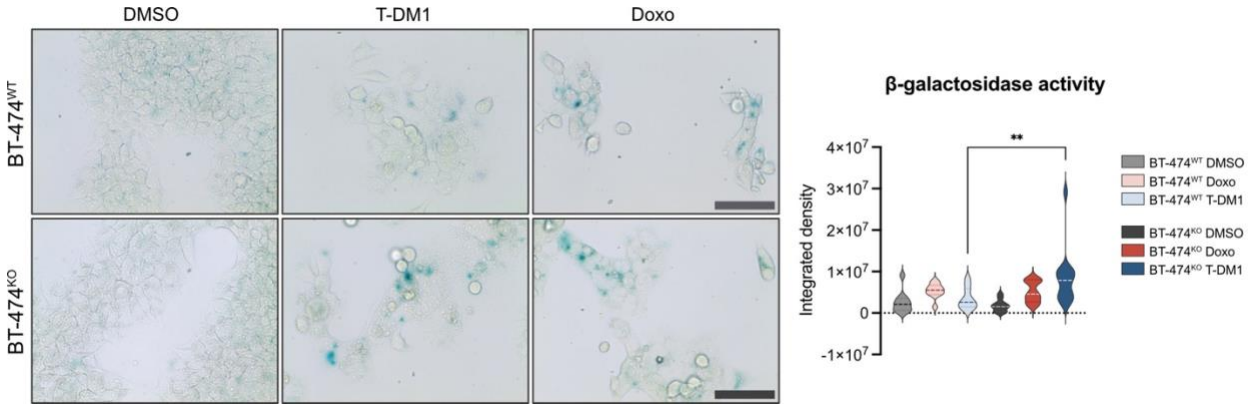

Figure R13. Treatment-induced senescence with morphological features and β-galactosidase staining after five days of T-DM1 treatment in BT-474^{WT} and BT-474^{KO} cells. Doxorubicin was used as positive control; ** p = 0.0059; Mann–Whitney U test; scale bar = 1.5 mm.

2.2.2. *NF1* ablation leads to prolonged and aberrant mitosis

We qualitatively investigated mitotic spindle and chromosomal dynamics of BT-474^{WT} and BT-474^{KO} cells by stable expression of H2B-GFP (to monitor chromatin condensation) and a cell permeable, highly specific microtubular probe. Nuclear envelope breakdown (NEBD) was set as T0 and the longest distance between chromosomes towards opposite spindle poles (anaphase A) as T1, , following the methodology of Mercadante DL, Crowley EA & Manning AL[260]. First, we confirmed a longer time from NEBD to anaphase A in BT-474^{KO} *vs* BT-474^{WT} cells (mean 87.28 *vs* 65.60 min ± 1.99; p = 0.0063; **figure R14A, B**). BT-474^{KO} cells frequently experienced a temporary multipolar state (**figure R14**, green arrowheads), with a small percentage undergoing multipolar cell division (**figure**

R14C). As expected for such events, numbers were small for statistical inferences. In agreement with previous data[261], multipolarity was associated with an increased frequency of lagging chromosomes during anaphase (**figure R14**, white arrowhead) in BT-474^{KO}. This phenomenon of efficient clustering into pseudo-bipolar spindles ensures a viable progeny in p53 deficient cells[261–264], but become prone to the formation of merotelic attachments - an error in which a single kinetochore is attached to MTs emanating from both spindle poles -, resulting in lagging DNA and chromosome segregation errors[265].

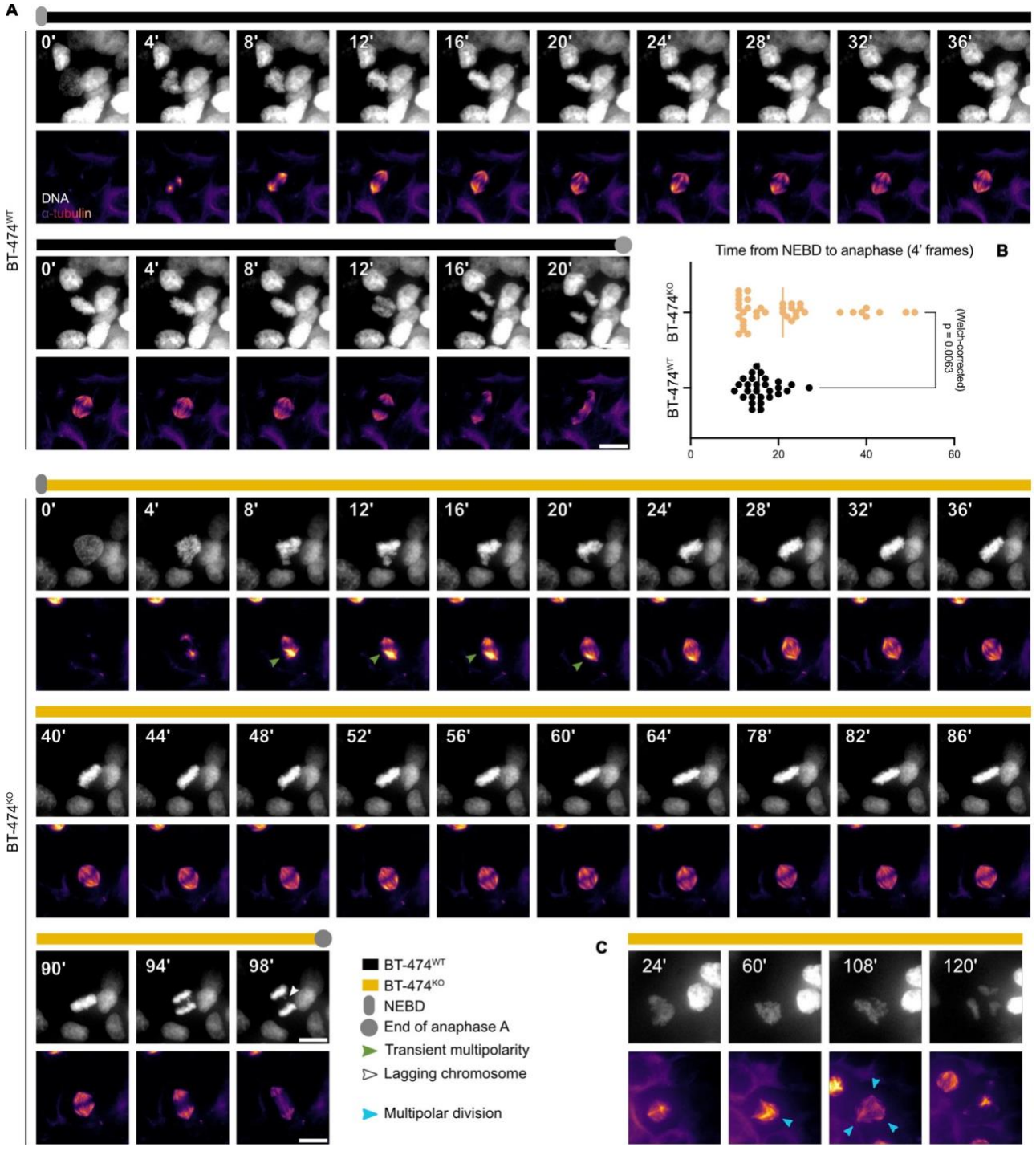

Figure R14 (*previous page*). A. Still frames from the analysis of mitotic timing in H2B-GFP/mCherry BT-474^{WT} and BT-474^{KO}, respectively. Scale bar = 15 µm; **B.** Time from NEBD to anaphase A was measured with 4 min frames individually from 28 BT-474^{WT} and 39 BT-474^{KO} cells where the full mitotic course could be appreciated. Frame means are plotted with interquartile range; Welch's *t*-test was used; **C.** Key frames of a BT-474^{KO} cell engaging anaphase in a multipolar conformation.

2.2.3. Centrosome amplification (CA) is a hallmark of *NF1*KO cells

Multipolar structures suggested the presence of supernumerary centrosomes in the absence of *NF1*, which would explain the nonphysiological pulling forces and lagging chromosomes observed in time-lapse microscopy. To quantify centrosomes, we first synchronised HCC194 cells in metaphase by a combination of late G2 arrest with a CDK1 inhibitor (RO3306) and timely proteasome degradation blockade after release[266] (**figure R15A**). We analysed cells co-stained with a centrosome marker (Cep3) and α-tubulin. HCC195^{KO} population showed a significantly larger fraction of cells with >2 centrosomes compared to HCC195^{WT} (mean 31.21 *vs* 9.92%; p = 0.0002; **figure R15B**), with several unresolved multipolar spindles and assorted morphologies of aberrant metaphase plates. Since long exposures to CDK1 inhibitors may induce the accumulation of centrosomal components[267,268], we quantified centrosomes in a distinct cell line and using double thymidine block (DTB) to synchronise cells. Again, supernumerary centrosomes were significantly more common in SK-BR3^{KO} compared to SK-BR3^{WT} cells (23.14 *vs* 4.35%; p < 0.00001; **figure R15C**). We further noticed multiple cells with >2 centrosomal structures separated by narrow intercentrosomal distances (**figure R15C, inset**), confirming the frequent transition from multipolar to pseudo-bipolar states prior to anaphase. Interphase cells were evaluated as well[269] by using α-tubulin for masking the cytoplasm boundaries and precisely attribute centrosomes to their respective cytoplasm (**figure R15D**). Of note, T-DM1 treated SK-BR-3^{KO} cells more frequently arrive at metaphase with massively wider intercentriolar distances, retaining the multipolar state (**figure R15C, inset**). Even though at high intracellular concentrations DM1 completely abrogates MT structures, mitotic slippage under subtle spindle defects is a known mechanism of resistance to MTAs[270–272], and can be speculated as a complementary effect of T-DM1 over cells lacking functional *NF1*, which are unlikely to thrive in case of unsuccessful centrosome clusering before mitosis exit. The presence of extra centrosomes usually triggers autophagy for Cep63 degradation as means to avoid genomic instability[273,274]. We looked at autophagy activation through the LC3II/LC3I ratio, which was reduced in BT-474^{KO} and SK-BR-3^{KO} cells (but not in HCC1954^{KO}), suggesting that impaired

autophagic degradation may be partially responsible for maintaining CA upon *NF1* loss. Treatment with DM1 did not affect these parameters (**figure R15E**).

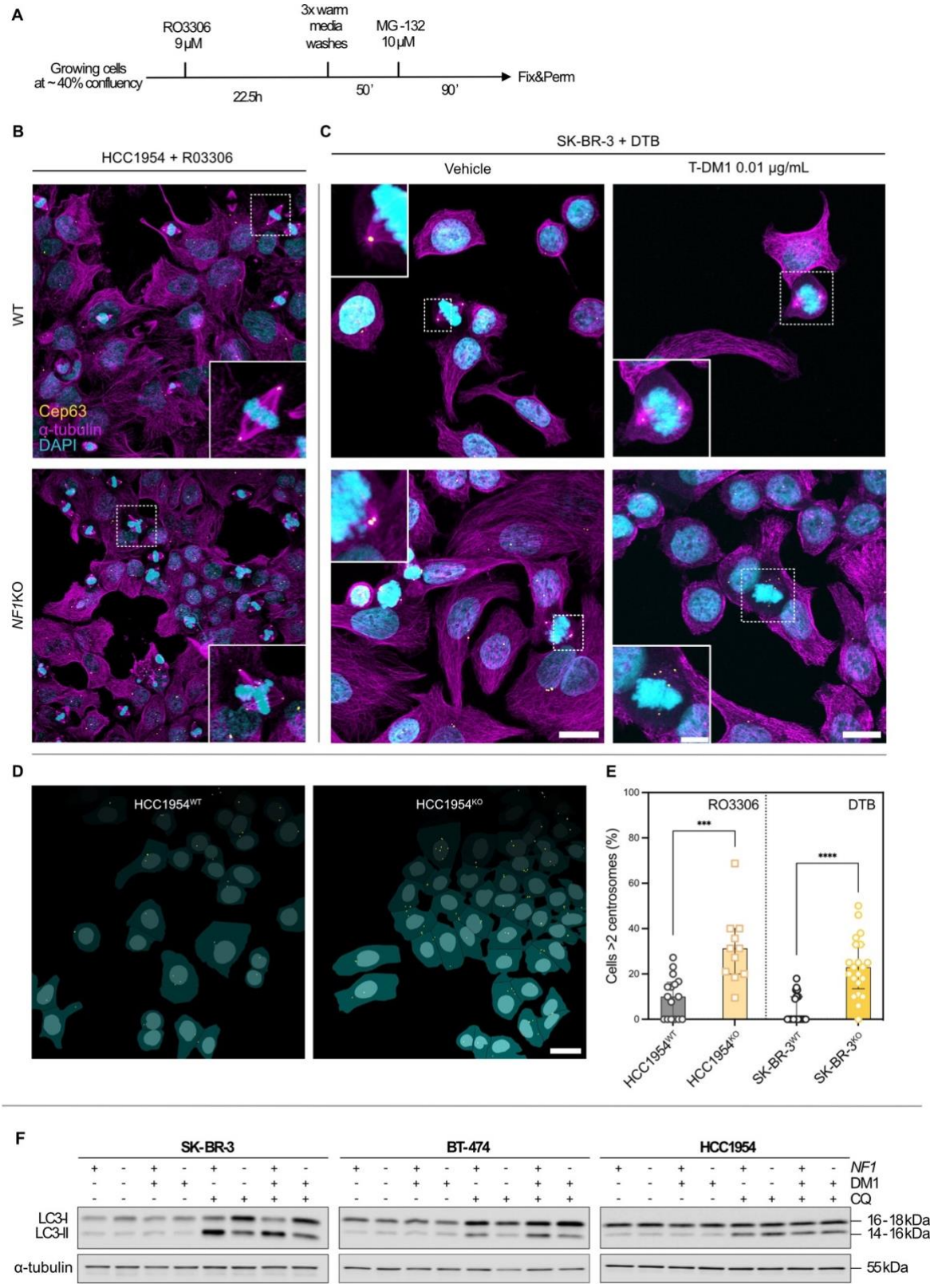

Figure R15 (*previous page*). A. Experimental scheme of metaphase synchronisation and **B.** results from HCC1954 cells co-stained with Cep63 (yellow), α-tubulin (magenta) and DAPI (cyan). Insets show a perfect bipolar spindle containing one centrosome each for WT and a multipolar architecture of a cell with five centrosomes for *NF1*KO; **C.** Same readout was sought for using SK-BR-3 cells and DTB. Inset for SK-BR-3^{KO} shows an example of pseudo-bipolar mitotic figure, indicative of efficient centrosome clustering wit unresolved multipolarity upon T-DM1 treatment in *NF1*KO cells. Scale bar = 30 µm, Inset scale bar = 7.5 µm; **D.** CellProfiler masking for interphase centrosome analysis and **E.** Overall quantification of cells with >2 centrosomes. *** p = 0.0002; **** p<0.0001, Student's *t*-test, two-tailed; **F.** Autophagy activation analysis. CQ was added in the last 4h, allowing detection of the total amount of autophagosomes. Data were generated and analysed together with E Gavilán-Dorronzoro, a postdoc within the lab).

2.2.4. Loss of *NF1* increases chromosome misalignments, resulting in congression defects and aneuploidy

Supernumerary centrosomes and aberrant spindle dynamics usually translate into chromosomal instability[275–278], so we assessed if *NF1* loss was associated with aneuploidy. Indeed, BT-474^{KO} cells showed increased abnormal chromosome alignment when compared to BT-47^{WT}, including major polar bundles (25 - 34,2 in BT-474^{KO1} and BT-474^{KO2}, respectively) *vs* 9,7% in BT-47^{WT}, **figure R16A**). Additionally, metaphase plate size, a marker of genomic instability[279280,281], was significantly wider in BT-474^{KO} cells (mean 11,8 *vs* 8,93 µm; p < 0,0001; **figure R16B**). Thus, BT-474^{KO} cells appear to progress through mitosis despite incomplete kinetochore-MT attachments and/or misaligned chromosomes, a process that is inhibited by the spindle assembly checkpoint (SAC) in physiological conditions[282283,284].

To quantify polyploidy in BT-474^{KO} cells, we measured DNA content throughout the cell cycle using BrdU-PI staining. BT-474^{KO} clones exhibited a significantly higher fraction of events with >2n DNA content (mean 5.07 *vs* 2.01; p = 0.0096, Student's *t*-test, two-tailed; **figure R16D**). Finally, we sought to validate this finding by looking at aneuploidy levels in BC patients from the large AACR-GENIE dataset, which includes 15210 BC patients, of which 6598 underwent targeted sequencing with *NF1*-containing panels[52]. By quantifying segmentation data using Arm-level Somatic Copy-number Events in Targeted Sequencing (ASCETS) - a targeted-sequencing specific aneuploidy score quantifier[285] - we found significantly higher aneuploidy scores on the 290 patients that were

mutated for *NF1* compared to the WT population (median 0.2567 *vs* 0.20592, p = 5.06 x 10^{-6}, Wilcoxon signed-rank test).

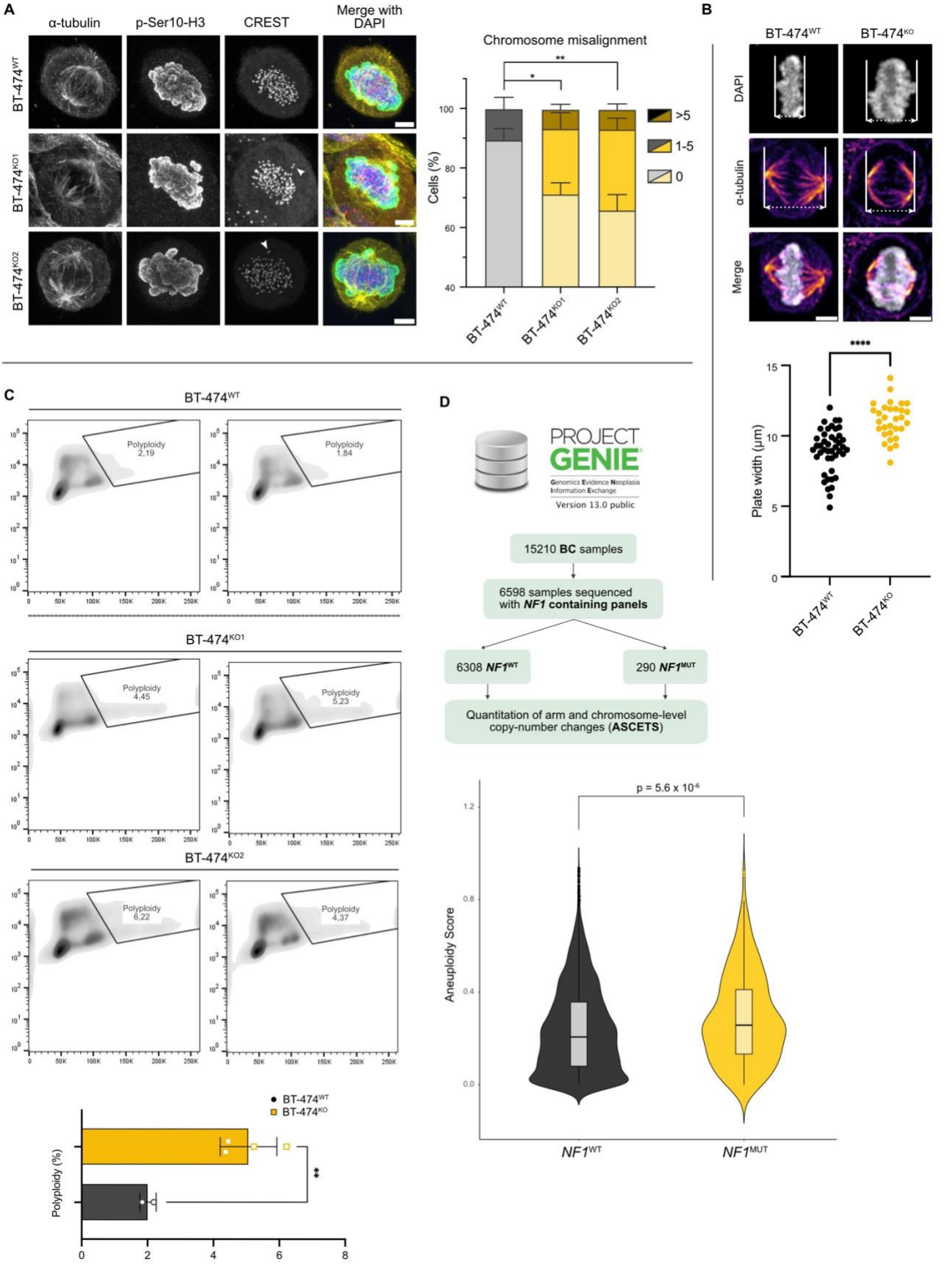

Figure R16 (*previous page*). A. Representation and quantification of chromosome alignment phenotypes of BT-47^{WT} and BT-47^{KO} metaphase-synchronised cells. Misaligned chromosomes were determined by identifying kinetochores outside the metaphase plate (white arrowheads; p = 0.0358 and 0.0083 for clones 1 and 2, respectively; error bars are SD. Student's *t*-test, two-tailed); **B.** Analysis of chromosome plate widths and their representation against the metaphase spindle length. Individual metaphase widths are plotted with mean ± SD. At least 30 metaphase plates for each genotype were measured. Metaphase spindle length could not be formally quantified. Scale bar = 5 µm; **C.** Ploidy, assessed from growing samples using flow cytometry and BrdU incorporation; error bars are SD; **D.** Workflow and aneuploidy scores calculated from targeted sequencing panels of *NF1*^{WT} patients compared to *NF1*^{MUT} in the AACR-GENIE dataset. Data were generated and analysed together with M Ippolito, a PhD student at the Department of Experimental Oncology, European Institute of Oncology, Milan, and E Bonetti, a bioinformatics PhD student within the lab.

2.2.5. *NF1* modulates microtubule dynamic instability

Having observed that proper and timely spindle organisation is impaired upon *NF1* loss, resulting in chromosomal instability (CIN), we looked into the specific role of neurofibromin in microtubular dynamics.

As mentioned in *section 1.3*, neurofibromin is known to physically interact with tubulin through both TBD and CTD, however several questions remain poorly understood, such as whether this interaction is tissue- and cell cycle-specific, what is its structural basis, and what is its functional relevance. We investigated the intracellular localisation of neurofibromin by confocal fluorescence microscopy in BT-474 cells at different time points after release from late G2 block. In interphase, neurofibromin had a diffuse pattern, most prevalently cytoplasmic. During mitosis, neurofibromin signal seems to increase by late G2 and across early mitotic phases until metaphase, to then decrease back to interphase levels (**figure R17A**). β-tubulin and neurofibromin were confirmed to physically interact by co-IP; interestingly, the strength of this interaction was cell cycle-dependent, since it could only be observed in cells enriched for mitosis by synchronization (**figure R17B**). In preliminary experiments using recombinant proteins, neurofibromin appears to interact with polymerised MTs (not shown), further suggesting that NF1 specifically interacts with the mitotic spindle.

The characteristic dynamic instability of MTs, as discussed in *section 1.3.2*, is crucial to many cellular processes, including the mitotic spindle formation[286,287]. To indirectly quantify this property upon

NF1 loss, we subjected HCC1954^{WT} and HCC1954^{KO} cells to cold-induced depolymerisation followed by repolymerisation at 37°C and measured the mean length of MT structures at different time points. HCC1954^{WT} cells showed the expected disappearance of polymerised microtubules after 60 min of cold exposure, followed by full regrowth 15 min after incubation at 37°C. This dynamics was abolished in HCC1954^{KO} cells, with multiple mature, strong-staining foci residual at T0 and T2 followed by an inability to reconstruct regular filamentous tubuli at T15 (**figure R17C**). This finding was replicated in multiple cell lines (not shown).

Hence, *NF1* absence may result in less dynamic microtubular behaviour, a phenotype that gets exacerbated by biological situations of high dynamic demands[288], such as mitosis or extreme environmental stress, like cold. Since MT dynamic instability is conditioned by several factors, including interactions with MT associated proteins (MAPs)[289,290], we assessed the status of MAPs in the context of *NF1* loss. We used the FUCCI(Ca) system to enrich BT-474^{WT} and BT-474^{KO} for mitotic cells. By immunoblotting, we consistently observed imbalanced levels of plus (i.e.: kinesin 3, Eg5)/minus (i.e.: dynactin) end motors and regulators of MT dynamic instability (i.e.: the whole CDK5-GSK-3β-CRMP2 pathway), suggesting a central role of *NF1* in a network that sustains physiological MT kinetics under pressing circumstances. Validation of these findings is ongoing.

2.2.6. *NF1* loss leads to increased abundance of GTP-tubulin

Since tubulin dynamics is conditioned by autocatalytic GTP/GDP turnover, we hypothesised that *NF1* may exert a direct role on this biochemical function similarly to its GAP activity on Ras. To support this hypothesis, we measured the global levels of GTP-tubulin in HCC1954^{WT} and HCC1954^{KO} cells using an antibody that specifically recognises the GTP-bound form of tubulin (hMB11) and requires live-cell permeabilisation[193]. To abrogate artefactual changes in intensity signal due to heterogeneity in the live-permeabilisation process[291], we carried out the staining in 1:1 co-cultures of HCC1954^{WT}-GFP and HCC1954^{KO}-mCherry cells, analysing images with a deep learning-based cell segmentation method[292] (**figure 18A**). We observed a significantly higher GTP-tubulin signal in HCC1954^{KO} cells, independently of the cell cycle state ($p = 0.01748$; Wilcoxon signed-rank, two sided; **figure 18B, C**). This difference was preserved after normalisation for both total α-tubulin ($p = 0.03458$) and cell area ($p = 0.03335$) (not shown). Signal was observed throughout the cap and the lattice of MTs. This finding was consolidated with two additional independent experiments, qualitatively identical. Appropriate quantification of the replicates is ongoing.

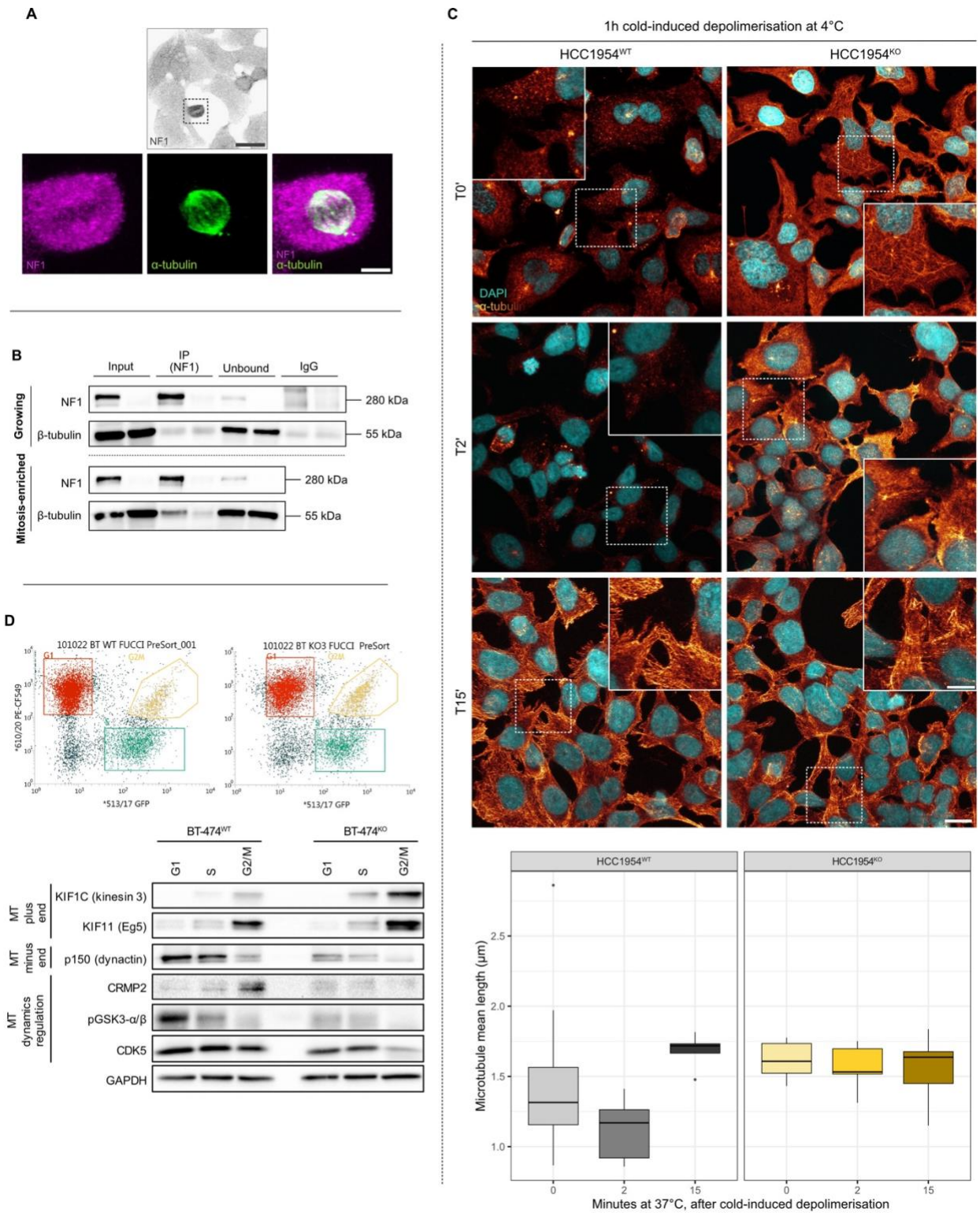

Figure R17. A. Neurofibromin shows a spread pattern in interphase cells, but signal increases during mitosis and colocalisation with the spindle becomes evident. Scale bars = 30µm (top) and 4 µm (bottom); **B.** Neurofibromin co-immunoprecipitates with β-tubulin in mitosis-enriched but not in

asynchronous cells. IP was performed with anti-neurofibromin, and then blotted with the same antibody plus an anti-β-tubulin; **C.** HCC1954^{KO} cells right after 1h of cold-induced MT depolimerisation (T0), and after 2 (T2) and 15 (T15) minutes of repolimerisation at 37°C. Mean microtubular lengths of at least 5 fields-of-view for each time point were plotted with SD. Scale bars = 20μm and 15 μm (insets); **D.** FUCCI(Ca)-based sorting and immunoblots of whole-cell lysates probed against key proteins responsible for microtubular dynamics according to cell cycle phase.

To gain structural insight of how GTP/GDP-induced conformational alterations may drive hypersensitivity to DM1, we overlapped the GTP- and GDP-bound structures of the α/β-tubulin dimer. We found that the most prominent change involves the Asp179 residue (**figure 18D**), which resides in a loop that is "closed" when the E-site is occupied by a GDP molecule, but assumes an "open" configuration upon GTP binding (**figure 18E**). A tubulin-spongistatin complex (being spongistatin a maytansin analogue) was recently resolved to a 2.4 Å resolution, demonstrating that polar contacts formed between spongistatin and the β-tubulin main chain carbonyl group of βAsp179 are crucial to stabilise the complex[293]. This suggests a model in which *NF1* loss may lead to an increased abundance of a tubulin pool with higher affinity to DM1 (**figure 18F**).

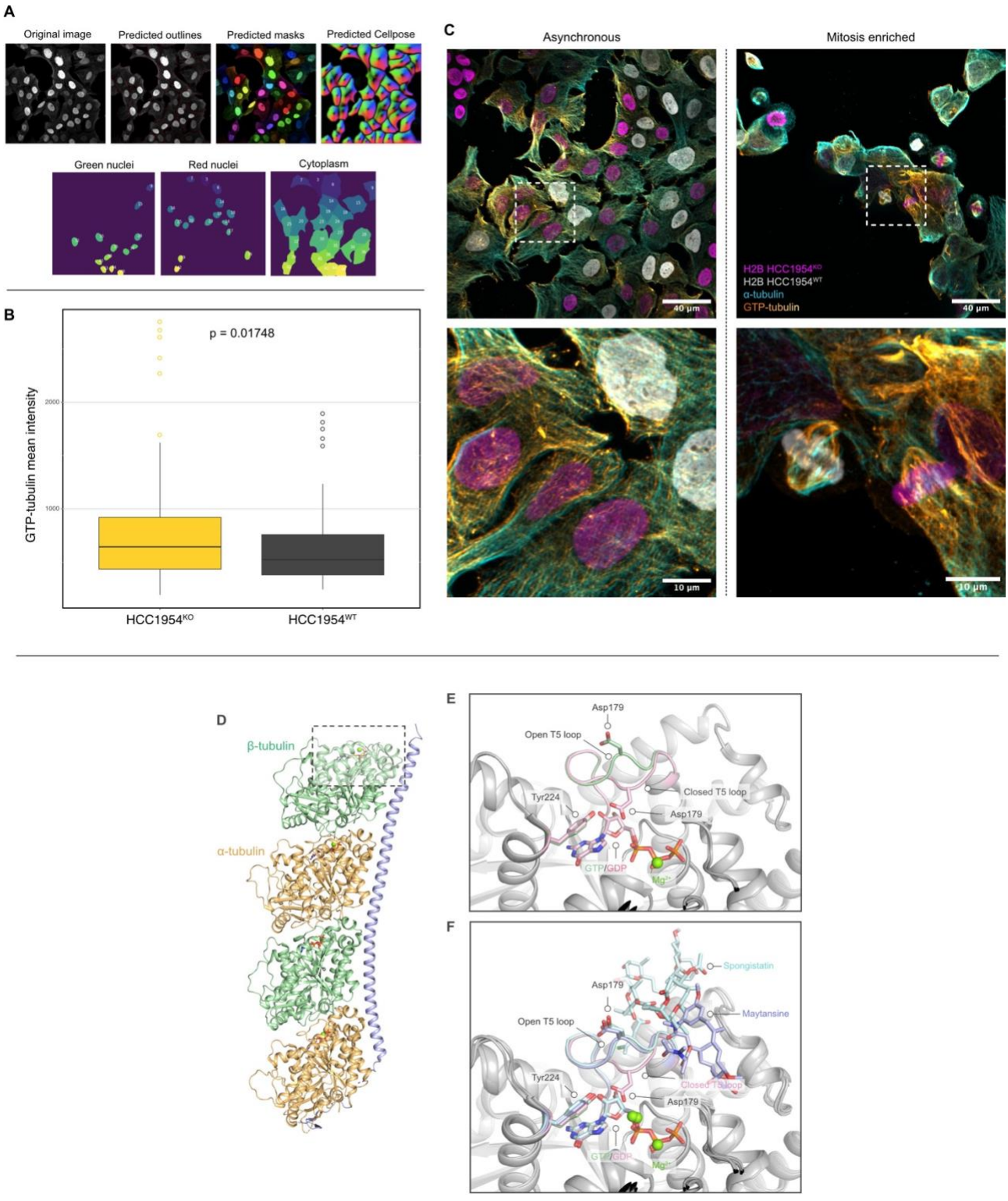

Figure 18. A. Representative images of the Cellpose-based deep learning pipeline used for cell segmentation within the co-culture; **B.** Co-culture of H2B-GFP/mCherry-tagged HCC1954^{WT} and HCC1954^{KO} cells, respectively, live-stained with anti-GTP-tubulin and counter-stained with α-tubulin after fixation, as described in *section 2.17*; **C.** Mean intensity of GTP-tubulin is plotted, with interquartile ranges; p = 0.01748, Wilcoxon signed-rank, two sided. At least 50 cells for each

genotype were analysed; **D.** Structure of an α/β-α/β tetramer. Insets are the region next to the β-tubulin E-site showing **E.** the overlap of a GTP- (light green, PDB 3ryf) and a GDP-tubulin (pink, PDB 3ryi), highlighting the conformational change of the T5 loop; and **F.** further overlap of maytansine - compound from which DM1 derives (light blue, PDB 4tv8) and spongistatin (cyan, PDB 6fii), which is known to stabilise its β-tubulin binding through the Asp179/Tyr224 residues. Data were generated and analysed together with M Marenda, a bioinformatician staff scientist, and L Scietti, head of the Biochemistry and Structural Biology Unit at the Department of Experimental Oncology, European Institute of Oncology, Milan.

2.3. *NF1* loss reorganises the actin cytoskeleton and modifies biophysical properties associated metastasis

2.3.1. *NF1* loss leads to enhanced anchorage-independent growth

The increased prevalence of *NF1* mutations in metastatic tumours led us to explore its involvement in cellular processes associated with metastatic growth. Anchorage-independent growth is one of the key initial characteristics acquired by cancer metastasis[294–296]. To assess the involvement of *NF1* in this phenotype, we grew BT-474^{KO} and SK-BR-3^{KO} cells and their WT controls in low-density, single cell suspensions on-top of a Matrigel matrix. By phase contrast imaging after 21 days, we observed a remarkable difference in size, with embedded BT-474^{KO} and SK-BR-3^{KO} spheroids' area accounting for an almost 3-fold increment compared to WT (mean 14.465 *vs* 5.021 μm^2 for BT-474 and 26.276 vs 8.068 μm^2 for SK-BR-3 cells; $p < 0.0001$ for both; Student's *t*-test, two-sided; **figure 19A**). Similarly, we plated the same models already embedded in Matrigel matrix from day 0 and treated them at day 10 with DMSO or lapatinib 0.1 μM until day 28. BT-474^{KO} and SK-BR-3^{KO} cells from DMSO groups were again fitter, starting off at similar growth rates, but diverging later on and never reaching a plateau until the end of the experiment. Lapatinib treatment completely eradicated viable parental cells, whereas in *NF1*KO spheroids growth was decreased but not abrogated, further supporting a resistant phenotype, possibly stronger than what is observed in 2D cultures (**figure 19B**).

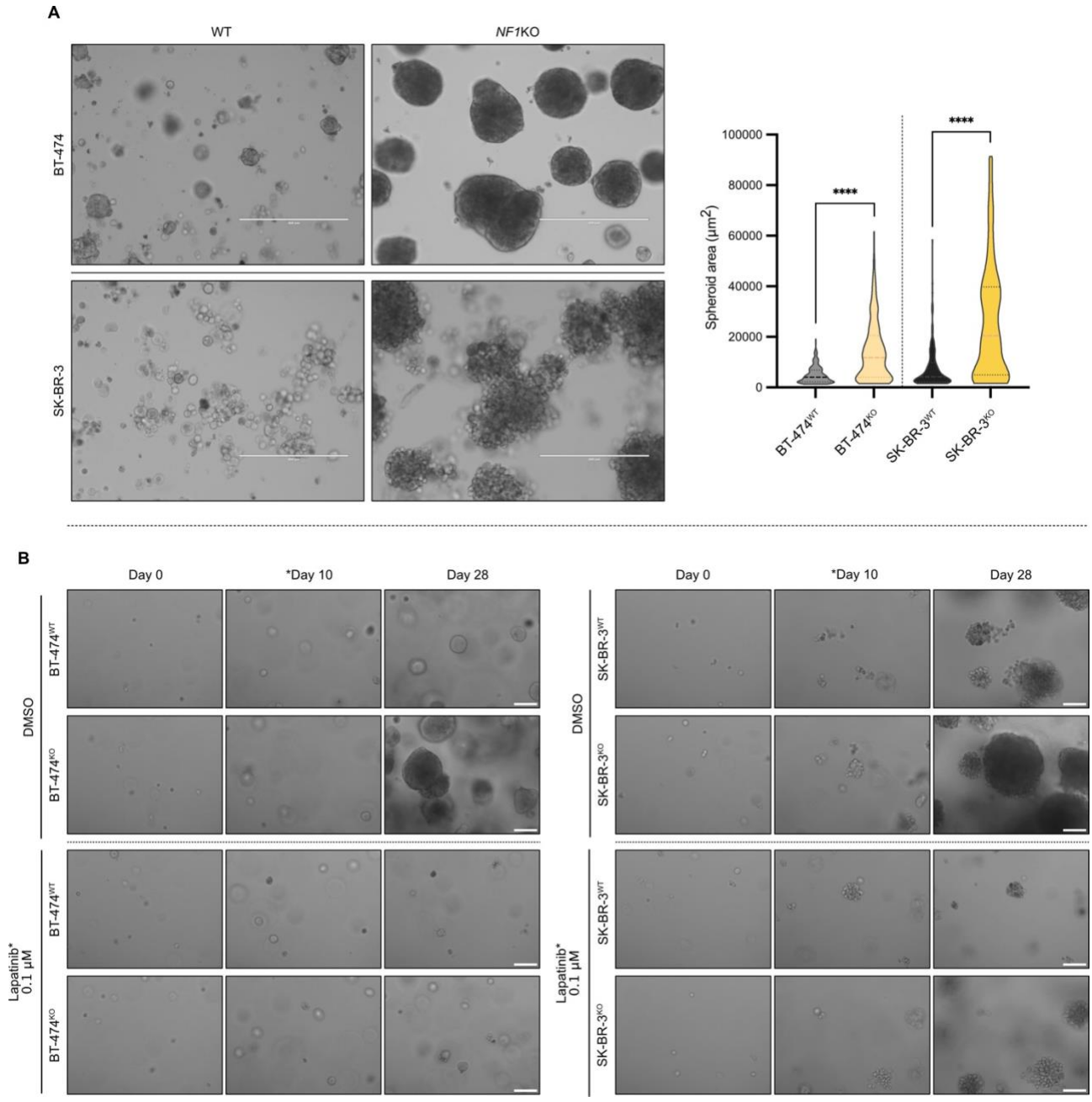

Figure 19. A. SK-BR-3 and BT-474 cells were seeded on-top of Matrigel matrix and let grow, with spent media change every three days. Phase contrast images were acquired at day 21 (n = 3). 170 and 112 spheroids were analysed for BT-474 and SK-BR-3, respectively. Violin plots comparing spheroids' area (µm^2). Scale bar = 400 µm; **B.** Cells were embedded in 50 µL of Matrigel and formed spheroids were cultured for a total of 28 days, with DMSO or lapatinib 0.1 µM added at day 10 (*). Spent media with or without the drug was changed every 72h.

2.3.2. Biophysical adaptation and actin cytoskeleton remodeling as direct consequences of *NF1 loss*

Mechanical interactions between tumour cells and their specific microenvironments are known determinants of cell phenotype and behaviour. To investigate *NF1*-dependent actin cytoskeleton remodelling, we first collected BT-474^{WT} and BT-474^{KO} spheroids grown in Matrigel matrix and stained them with fluorescent phalloidin and a nuclear marker, preserving their architecture. Under confocal IF, we observed a redistribution of the F-actin meshwork in BT-474^{KO} and SK-BR-3^{KO} cells, with a notable enrichment underlying the plasma membrane (yellow arrowheads, **figure 20A**). This rearrangement likely upregulates cortical tension and modulates global cell surface mechanics, as suggested also by immunoblotting of major epithelial and cell-cell junction markers from pooled 3D structures (**figure 20B**). To understand the extent of such phenomenon, we assessed the mechanoproperties of these cells through atomic force microscopy (AFM), in collaboration with the Podestà group at UniMi. This tool allowed us to probe the surface of growing populations with a colloidal tip within a spatial resolution suitable for accurate mapping the topographical and elastic properties of each individual cell (**figure 20C**). Using a medium indentation of ~2-3µm, BT-474^{KO} cells presented with prominent cell junctions compared to BT-474^{WT}, especially visible on mechanical maps (white arrows, **figure 20D**). Overall, these cells are significantly stiffer (~70% increment) as per Young's modulus when compared to their parental counterparts (**figure 20E,F**), a characteristic of high organotropic phenotypes[297–299].

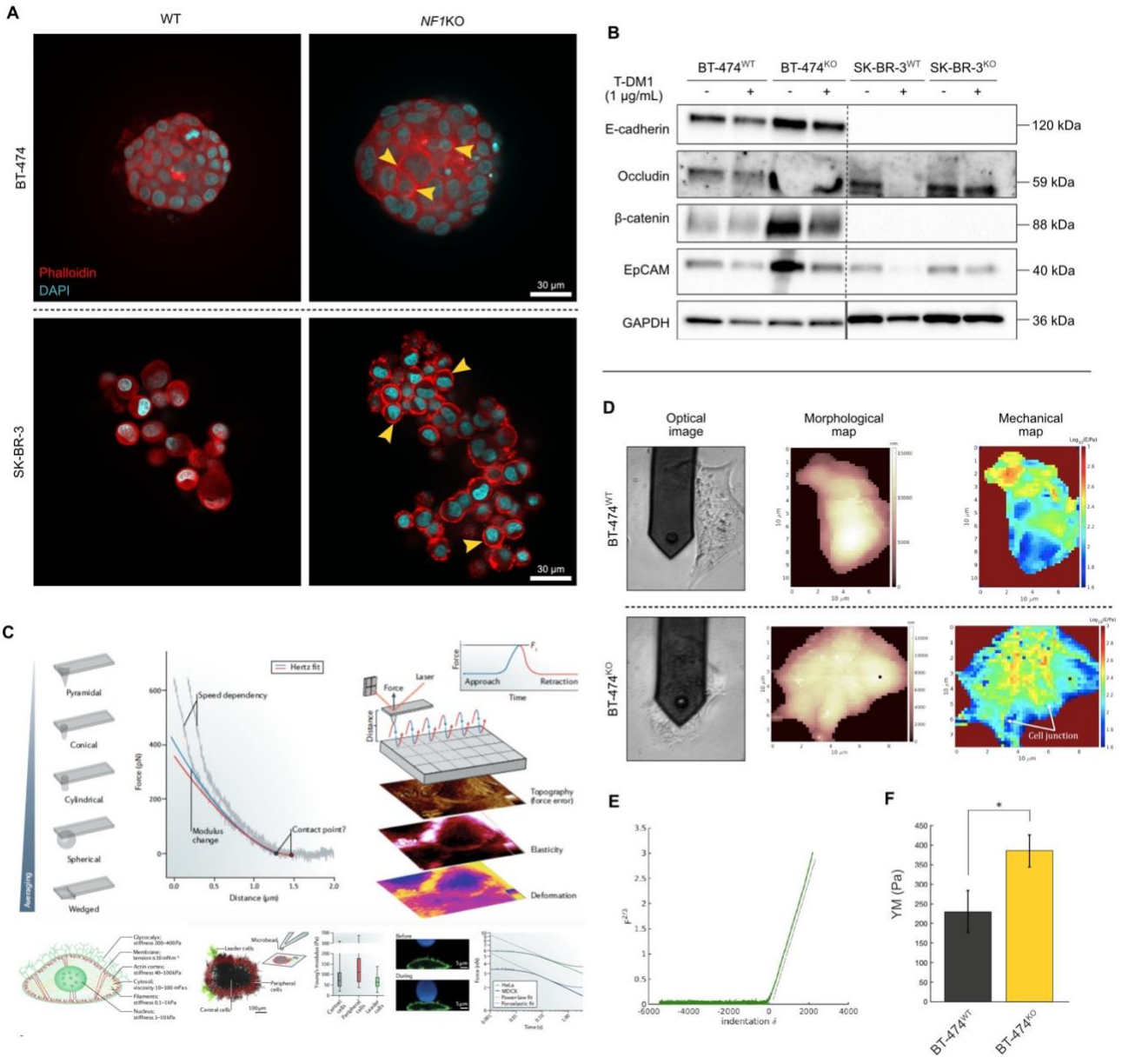

Figure 20. A. Immune-confocal microscopy of spheroids showing actin (red) reorganisation of *NF1*KO spheroids towards the cortex (yellow arrowheads); **B.** Western blot from pooled spheroids grown in Matrigel for 21 days and processed as previously described; **C.** Scheme of AFM-based probing and mapping for the assessment of mechanical properties of cellular systems; **D.** Representative optical, morphological and mechanical maps of BT-474^{WT} and BT-474^{KO} cells; **E.** Example of a linearised force-distance curve showing a single regimen (Hertzian model), which was then applied to the whole cell indentation (10-90%) and **F.** comparison of the effective elastic (Young's) modulus for each condition (n = 18-20 cells). Student's *t*-test, two-tailed. Error bars represent an effective error, resulting from the sum of instrumental error, inter- and intracell

variability. Data were generated and analysed together with M Chighizola, a physicist postdoc at the Podestà lab at the Department of Physics, University of Milan.

We are currently quantifying cortical actin with high-resolution microscopy[300] and correlating with AFM data from distinct cell lines in both 2D and 3D cultures.

3. Discussion

3.1. Rational bedside-bench-bedside circuits to uncover tumour liabilities: the case of *NF1*

Genetic alterations that are enriched in secondary compared to primary lesions may reflect properties typical of the metastatic phenotype like increased migration, adaptability to novel microenvironments and/or therapeutic resistance. *NF1* mutations are emerging as highly prevalent and potentially targetable across different tumours[303], but constrains on detecting its heterogeneous mutational spectrum, the prevalence of research on *NF1* activity as a Ras supressor[304,305] at the expenses of other functions, and the lack of evidence on highly effective *NF1*-matched drugs have prevented its wider adoption as a clinical biomarker.

In the present study, using *in silico*, *in vitro* and *in vivo* experimental systems, I uncover how the loss of *NF1* can (i) determine a prometastatic phenotype through cytoskeleton remodeling and (ii) promote selective response to T-DM1. I provide a mechanistic rationale and expand our knowledge on its previously underappreciated function in MT/actin dynamics that can be exploited therapeutically. The study is conceived within a framework for translational research, a bedside-bench-bedside circle in which a clinically relevant question is scrutinised for its molecular and mechanistic foundations to then feedback clinically useful information. I believe this process should be promoted to build therapeutic approaches that are not based on the mere historical succession of clinical trials but on multiparametric, biology-driven treatment algorithms.

In the next sections, I will first highlight how these findings can be used to inform clinical decision-making in the management of $HER2^+$ BC. I will then speculate on possible molecular mechanisms to explain *NF1* role in MT dynamics, and how this may clarify our understanding of the activity of MT targeting agents (MTAs), information that can be used for rational drug design. Finally, I will speculate on possible new lines of *NF1*-related research, including the tumour microenvironment and other tumour types.

3.2. *NF1* as a biomarker for decision-making in $HER2^+$ BC

In BC, especially in HR^+ disease, previous studies have shown that *NF1* mutations correlate with endocrine therapy resistance[121–123,306,307] and may benefit from the association of MEK and/or CDK4/6 inhibitors. However, the impact of *NF1* LoF in other BC subtypes has not been thoroughly

investigated. In HER2⁺ mBC, we find that *NF1* is one of the most common actionable mutated genes with a prevalence of ~10%, even more common than other genetic biomarkers currently under investigation in this subset like *ERBB2* mutations[308–311], PD-L1[312], TILS[313–315] or TMB[316–318]. *TP53*, the most commonly mutated gene in absolute terms, is currently not actionable. To date, there are no established reliable biomarkers of activity for anti-HER2 ADCs other than the expression profile of HER2, which almost exclusively impacts on antibody-based drug binding[19,319,320]. The HER2DX tool was able to predict response to T-DM1 based on *ERBB2* mRNA levels, with a sensitivity of 84% and 100% specificity[321]. However, emerging evidence suggests that the efficacy of an ADC is driven by antibody-, linker- and payload-related factors, each one being a function of complex interactions between the molecule, the tumour and its microenvironment[36,322,323].

In the MARIANNE trial, a randomised phase 3 study in genetically unselected patients[324], T-DM1 failed to demonstrate superiority when compared, with or without pertuzumab, to trastuzumab plus a taxane as frontline for HER2⁺ mBC, although it was better tolerated. In the EMILIA trial, which led to the approval of T-DM1 in 2013, only 43% of BC patients with high HER2-expressing tumours actually responded to T-DM1[30]. Finally, in the recently presented DESTINY-Breast03 trial, patients from the T-DM1 arm (**figure D1**, red curve) had a mean PFS rate of 26.4% at 24 months, implying a significant fraction of long-term responders (**figure D1**, yellow highlighted area) under a minimally toxic regimen.

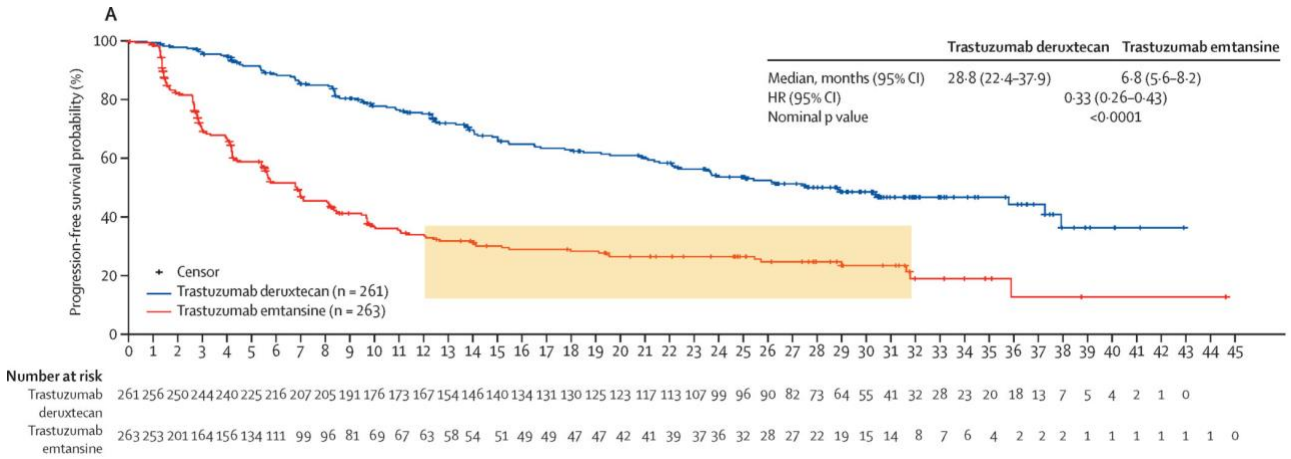

Figure D1. PFS by blinded independent central review from the DESTINY-Breast03 trial. Modified from Hurvitz et al.[33]

Although the benefits of T-DXd in terms of PFS and overall survival (OS) were clear, toxicities are still an issue in the clinics[325,326]. Within the controlled setting of the trial, drug-related adverse events that led to regimen discontinuation, dose reduction, or drug interruption were significantly higher in the T-DXd group compared to the T-DM1 group (% of all grades/grade ≥3): nausea (77/7 *vs* 30/<1) and vomiting (52/2 *vs* 11/<1), diarrhoea (32/1 *vs* 8/<1), fatigue (31/6 *vs* 20/<1), decreased appetite (30/2 *vs* 18/<1) and body weight loss (23/2 *vs* 9/<1), alopecia (40/<1 *vs* 3/0), and decreased white blood cell counts (23/6 *vs* 6/<1). Most importantly, the rate of ILD/pneumonitis, a highly morbid treatment-related adverse event, was 15% in the T-DXd *vs* 3% in the T-DM1 group at the second interim analysis. In the DESTINY-Breast04, where T-DXd was compared to treatment of physician's choice (TPC) in patients expressing low levels of HER2 (HER2-low, *see section 1.1.1*), 45 patients in the T-DXd group (~12%) developed ILD/pneumonitis, resulting in 3 deaths. Only one patient in the chemotherapy group developed this condition, in a mild form[18]. On the contrary, in the TH3RESA trial, where patients were randomised to receive T-DM1 or TPC, all of grade ≥3 adverse events were more common in the control group than in the T-DM1 group[327].

Thus, if an increased sensitivity of *NF1*-mutated patients is formally confirmed in a randomised trial, *NF1* may be proposed as a clinical biomarker to identify patients that would benefit from T-DM1 in the early lines, avoiding or delaying the significant toxicity associated with T-DXd. This approach would assist in finding the optimal sequencing of therapies according to each patient's clinicogenomic background, potentially improving general outcomes.

With increasing accessibility to NGS panels in clinical practice, the incorporation of *NF1* status in prospective trials - from tissue or plasma - as a prognostic and/or predictive marker is facilitated. Nevertheless, whole genome sequencing of 560 BC samples from Nik-Zainal et al.[328] documented a wide range of structural variants affecting *NF1* (e.g.: tandem duplications, deletions, translocations, inversions) which can be missed by usual targeted sequencing. This suggests that prevalence of somatic *NF1* alterations that lead to LoF may be currently underestimated.

Expanding the identification of *NF1* mutated cases through inexpensive assays (e.g.: IHC) for screening has been proven a successful strategy in gastrointestinal tumours using a commercially available anti-neurofibromin NFC antibody[329] and may also be suitable for further correlation of *NF1* tissue staining with specific clinical outcomes in a larger scale.

The utility of *NF1* as a biomarker is likely not limited to $HER2^+$ BC. In other tumour types, the prevalence of *NF1* mutations may arrive to over 30%, excluding desmoplastic melanoma (*see section 1.2.3 and 3.3.3 for future perspectives*).

3.3. Mechanistic basis for the activity of *NF1* on microtubular dynamics

Neurofibromin has mostly been investigated as a negative regulator of Ras through its GAP activity. However, as mentioned in *section 1.2.3.2*, there is evidence for additional activities that are Ras-independent. In particular, structural and biochemical evidence[72], including the one presented in this manuscript, indicate that *NF1* affects, directly or indirectly, other targets like tubulin, possibly through different domains and according to interphase or mitotic state.

As extensively reviewed in *section 1.3.2*, the kinetics of tubulin-intrinsic GTP hydrolysis activity governs the dynamic instability of MTs[183,240,330], which is crucial to many cellular processes, but especially to the mitotic spindle formation[286,287]. Several MAPs, including kinetochore proteins[331], dynein[332], EBs[333,334] and kinesins[180,202] are known to modulate the tubulin GTP-GDP turnover but also to have their binding dynamics dictated by the GTP conformation of tubulin and its depolymerisation rate[197]. The structural basis of the activity of *NF1* on tubulin, in particular the increased abunbdance of GTP-tubulin observed in the absence of *NF1* (**figure R18**), is currently under investigation in the lab (see *section 3.3*). Here, I will focus on models that can be proposed to explain the observed hypersensitivity to DM1.

Under unperturbed conditions, an MT constantly cycles between states of polymerisation (slower, ~10–50 nm/s^{-1}) and depolymerisation (faster, ~300–500 nm/s^{-1})[192]. During polymerisation, a new GTP-bound α/β-tubulin unit is added to the growing polymer (plus or minus end) and the GTP is hydrolysed to GDP, causing a shift to a "straighter" tubulin dimer conformation. The MT body - then prevalently constituted by GDP-bound tubulin[335,336] -, is unstable, but protected from depolymerisation by a "GTP cap" as long as it maintains a delay between addition of new GTP-bound α/β-tubulin dimers and hydrolysis, so the polymer keeps growing. When this rate inverts, the cap is lost and it rapidly triggers the protofilaments to peel off and depolymerise. This coexistence of stability- and instability-prone tubulin also happens at the mitotic spindle, with bundles of MTs linking spindle poles to the kinetochores (K-fibres), kinetochore-unrelated MTs that emanate from the poles overlapping the midspindle, and astral MTs, which radiate from the poles towards the cell cortex[337,338]. A consideration to bear in mind is that MTs turnover is way faster in living cells than *in vitro*[192], which supports the role of other cellular factors in modulating these dynamics. The likelihood of interaction for each specific conformation has been investigated not only with regard to other tubulin dimers, but to multiple MAPs and drugs as well.

Maytansine site ligands bind to the portion of β-tubulin that is involved in the formation of longitudinal contacts, destabilising MTs either by inhibiting the addition of further tubulin subunits (substoichiometric concentrations) or sequestering tubulin subunits in solution to form assembly-incompetent tubulin-maytansine complexes (high ligand concentrations)[39]. Based on our findings, we propose three non-mutually exclusive models to explain the increased activity of DM1 in *NF1* depleted cells, based respectively on structural, enzymatic and cell biology considerations, which can be independently verified using complementary experimental approaches:

- **Structure-first model**

  The maytansine binding site is located on an exposed pocket of β-tubulin, adjacent to the GTP/GDP-binding pocket and shaped by hydrophobic and polar residues of helices H3', H11, and H11', as well as the loops S3-H3' (T3-loop), S5-H5 (T5-loop), and H11-H11'[39,339]. Based on our *in silico* simulation (*figure 18*), the only conformational change in the maytansine binding site upon GTP-GDP transition involves the Asp179 within the T5 loop. Importantly, this residue seems to be highly relevant to stabilise maytansine binding, based on structural findings conducted with spongistatin-1, a natural compound that binds to the same site[293]. Thus, the increased abundance of GTP-bound tubulin observed upon *NF1* loss may lead to the increased exposure of this key residue, directly causing a higher availability of maytansine biding sites with a stronger affinity for DM1 interaction. This would be consistent with the CETSA results in *figure 8*. For an in-depth identification of diverse binding affinity profiles and to elucidate this possible dependency, we are currently working on to generate β-tubulin point-mutants[340–342] that both substitute the Asp179 or alter its three-dimensional position using a hybrid computational- and experimental-based pipeline[343,344].

- **Enzyme-first model**

  The ratio between GTP- and GDP-bound tubulin needs to be maintained within a certain equilibrium in order to ensure physiological dynamics of MT structures[345–347]. As we showed in *figure 18*, the loss of *NF1* increases significantly the amount of GTP tubulin in the cell. Evidence dating back to 1981[348] (**figure D2B**) shows that, unlike other agents with depolymerising activity, maytansine inhibits the hydrolysis of GTP to GDP tubulin (figure D2A). Thus, it may be hypothesised that the combined action of maytansine and *NF1* loss tilts the prevalence of GTP tubulin throughout the MT above a certain threshold, beyond

which MT dynamics is completely abolished. In other words, the amount of drug necessary to overcome this critical GTP-tubulin threshold is decreased by the simultaneous absence of *NF1*.

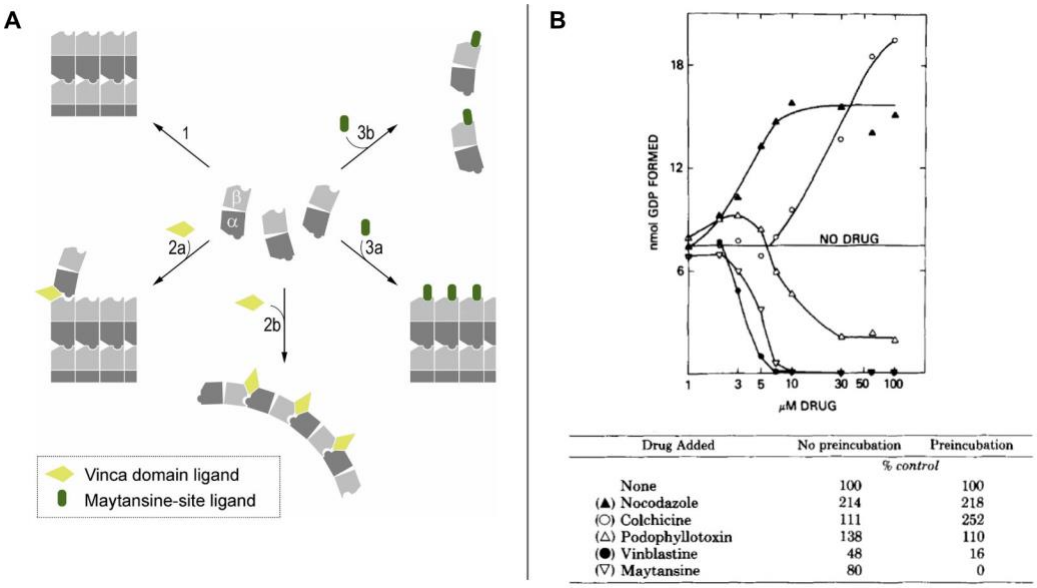

Drug Added	No preincubation	Preincubation
	% control	
None	100	100
(▲) Nocodazole	214	218
(○) Colchicine	111	252
(△) Podophyllotoxin	138	110
(●) Vinblastine	48	16
(▽) Maytansine	80	0

Figure D2. A. Shchematic representation of the different impact of the vinca- and mayntansine-binding agents on the tubulin dimer interface, but **B.** how they share a reduced effect on tubulin-dependent GTP hydrolysis. Modified from the original GTPase activity assessment of MTAs from the Ernest Hamel's and Chii M Lin's Laboratory of Pharmacology and Experimental Therapeutics at the National Cancer Institute in 1981[348].

- **Inhibition of centrosome clustering and bipolar spindle formation**

  As seen in *section 2.2.3*, cells accumulate supernumerary centrosomes upon *NF1* loss, which must be clustered into pseudo-bipolar configurations before anaphase entry in order to undergo successful cell division. By inhibiting plus end microtubular dynamics even at low concentrations[39], DM1 may specifically inhibit centrosome clustering, so that cells are forced to either indefinitely arrest in mitosis or progress to cytokinesis in a non-(pseudo)bipolar arrangement, a situation in which the uncoordinated pulling forces induce postmitotic cell death[349]. A qualitative assessment of our microscopy images shows that DM1-treated *NF1*KO cells indeed accumulate grossly abnormal, "shattered" multipolar conformations. Importantly, the inhibition of centrosome clustering would not be specific for *NF1*KO cells.

However, the significantly higher proportion of cells initiating mitosis with supernumerary centrosomes in the absence of *NF1* would explain the higher efficacy in this context.

The interaction of *NF1* with other MAPs may also occur through domains that do not directly participate in tubulin interactions. We observed imbalanced expression of MAPs, with higher expression of plus end proteins (i.e.: kinesin-3, Eg5), and reduced expression of minus end (i.e.: dynactin) and the CDK5/pGSK3-β/CRMP2 axis in *NF1*KO cells. This may help in understanding *NF1* role in MT dynamics and identify additional therapeutic targets. *KIF11* encodes for Eg5, a kinesin from the MT plus end required for bipolar spindle formation[234,350]. It plays a crucial role in correcting mitotic defects that would otherwise result in a nonviable progeny. When targeted by numerous recently developed small molecules[351–354], prolonged mitotic arrest follows, with death in mitosis or right after exiting[355], very much resembling the fate of T-DM1 treated *NF1*KO cells. Malignant peripheral nerve sheath tumour (MPNST) is a highly hyperploid condition and the leading cause of mortality in patients with neurofibromatosis type 1. By pharmacologically inhibiting Eg5 in ST88-14 and S462 MPNST cells - where *KIFF11* is highly expressed, like in our BT-474^{KO} model -, functional bipolar spindles were replaced by monopolar spindles, abrogating the alignment of chromosomes at the metaphase plate in most dividing cells[356].

Supernumerary centrosomes are an almost exclusively characteristic of neoplastic disorders and the clustering machinery becomes required for their survival[357,358]. An important consequence of this model would be that the presence of supernumerary centrosomes may itself be a highly selective biomarker for DM1 sensitivity[359].

3.4. Mechanobiological switches secondary to *NF1* loss and how they may impact the metastatic process

By genetically ablating *NF1*, we identified a clear remodelling of the actin cytoskeleton in both BT-474^{KO} and SK-BR-3^{KO} spheroids (*see section 2.3.2*), with signal enrichment towards the subcortical region. By analysing whole cell lysates of those structures by western blot, cell-cell adhesion markers of epithelial tissues (E-cadherin/β-catenin complex[360,361], occludin[362]) and EpCAM[363], were found to be increased in BT-474^{KO} and partially sustained upon T-DM1 treatment. SK-BR-3 is a cell line known to express no cadherins[364,365] yet presenting a similar phenotype, suggesting an interplay of multiple factors. Integrating AFM to assess the mechanoproperties of these cells in monolayer allowed us to observe an almost doubling of the global Young's module in BT-474^{KO}, a feature that has been

independently associated with drug resistance and metastatic patterns[297–299,366]. Prominent cell-cell junctions could also be observed upon *NF1* loss. These findings indicate a drastic reinforcement in the interactions of actin filaments to stabilise adherens junctions. Groups of cells are more likely to efficiently establish metastatic lesions[367,368], mostly by avoiding anoikis, a cell-detachment-induced apoptosis mechanism[369–371]. Aceto N et al. demonstrated that these circulating tumour cell clusters (CTC clusters) found in the blood of patients with cancer (i) carry an up to 50-fold increment in metastatic potential, and (ii) arise from oligoclonal tumour cells grouping from the primary lesion and not from intravascular aggregation events. By looking at single-cell transcriptomic data from these CTC clusters *vs* matched single CTCs from BC patients, they identified that the cell junction component plakoglobin was highly differentially expressed. By abrogating its function in mouse models, CTC cluster formation and lung metastases were supressed[372373–378].

NF1 negatively regulates many pathways that contribute to both these stimuli, mostly the Rho family small GTPases (i.e.: RAC1, ROCK) and their downstream effectors/GEFs (e.g.: LIMK2[165,169], PREX1[379]), but also PI3K/mTORC2[380], syndecans[153], FAK[175], caveolin - both directly and indirectly as a mediator of FAK[381] inhibition and MSI2 partering[145] -**,** and are found to be upregulated in *NF1* depleted models, including ours (*see section 2.2.1*). Preliminary data from RNA-seq of BT-474^{KO} and SK-BR-3^{KO} spheroids compared to their parental showed a significant differential expression of Ras effectors and the actin cytoskeletal remodeling pathways (not shown). Thus, *NF1* deficiency may be directly responsible for converging persistent interepithelial cell junction forces and Ras stimuli to endow bloodborne collective migration and a more efficient metastatic dissemination. On this front, we have two ongoing collaborations: (i) with the Podestà group at UniMi, to further characterise stiffness and adhesion forces in 3D models lacking neurofibromin. We aim to demonstrate that loss of *NF1* translates into measurable differences in stiffness and traction forces, which could provide a biophysical explanation for the enhanced 3D growth phenotype and be exploitable for diagnostic and therapeutic purposes, using accessible radiological an IHC techniques[301] as well as tight junctions and focal adhesion pharmacological targeting[302]; and (ii) with the Aceto lab at the ETH Zurich, where we are interrogating through microfluidic-based capture applied to mouse models, if *NF1* mutated tumours are indeed prone to shed CTC clusters.

3.5. *NF1* loss as a driver of chromosomal instability

In our study we provide evidence for *NF1* loss as a driver for chromosomal instability (CIN). *NF1*KO cells exhibited increased chromosomal distances from the nuclear centre (which is associated with

a propensity to missegregate[279]) and were frequently polyploid; coherently, *NF1*^{MUT} BC patients in the AACR-GENIE cohort showed significantly higher aneuploidy scores. Many tumour suppressors are involved in spindle orientation and cell polarity, like adenomatous polyposis coli (*APC*)[382], von Hippel-Lindau (*VHL*)[383], *PTEN*[384] and *BRCA1*[385]. In the case of *NF1*, many factors may contribute to the generation of CIN. Our data clearly show that *NF1*KO cells exhibit two characteristics: prolonged mitosis and supernumerary centrosomes, that can independently cause CIN[261,386–388]. It is currently unclear which of the two events causes the other. First, a marked imbalance of MAPs, potentially induced by excess of GTP-tubulin, together with the rearrangement of cortical actin would impair MT dynamics and cause a longer G2/M phase (*see section 2.2.1*). In that case, two possible explanations arise: (i) precocious activation of separase with incomplete cohesin removal from sister chromatids leading to segregation errors; or (ii) centrioles may disengage and generate fragmented centrosomes[389]. Alternatively, if supernumerary centrosomes are already present at prophase because of a direct activity of *NF1* on centrosome morphogenesis, M phase may be prolonged to allow time for correction of a non-bioriented spindle. To discriminate between these two models, it will be important to understand if CA is generated through excessive replication (which can take place in interphase, specifically at the beginning of S phase) or fragmentation (which would take place prior to cytokinesis). The temporal interplay between these events are under investigation within our lab by combining a fluorescent centriolar marker with time lapse imaging through multiple rounds of division.

Also, preliminary data from the same BT-474^{KO} models suggests a dysfunctional spindle assembly checkpoint (SAC), the surveillance mechanism that helps maintain the high fidelity of mitotic chromosome segregation by preventing cells from initiating anaphase if one or more kinetochores are not properly attached to the spindle[284,390](not shown). Proteins from this complex (e.g.: BubR1, Mad2) target the anaphase-promoting complex (APC) to halt abnormal mitosis and prevent tumourigenesis in a p53-mediated fashion[283,284]. Since BT-474 cells express exon 8-mutant p53[391] - like most advanced cancer patients -, this mechanism may be impaired, allowing for evolution of karyotypes with clonal expansion advantages. It is worth noting that budding yeast Δira1 Δira2 cells - homologous of human neurofibromin - bypassed mitotic arrest in response to spindle damage. This defective phenotype was rescued by the overexpression of the CTD but not the GRD, suggesting that neurofibromin/ira1 and ira2 are involved in SAC regulation as another Ras-independent, MT-related attribute of *NF1*[146].

Interestingly, recent findings from the Santaguida lab and collaborators demonstrate that elevated levels of CIN associate with chemoresistance in cell lines[395] and patient-derived xenografts (PDXs)[396]. That was particularly true for DNA-damage-inducig agents like topoisomerase inhibitors.

3.5. Future perspectives

The findings in the present study have generated significant interest in the lab to initiate an broad research program aimed at expanding our understanding of *NF1* biology and clinical utility. Future research will be funded through grants by Fondazione AIRC per la Ricerca sul Cancro and the Piano Nazionale di Ripresa e Resilienza (PNRR) program awarded to the host lab. I have been actively involved in the writing of these grants and plan to participate to or supervise some of the following lines of research.

3.5.1 Consolidating the role of NF1 as a biomarker for T-DM1 sensitivity

In order to consolidate the role of *NF1* as a biomarker in the clinical setting, two conditions should be supported by adequate evidence:

- A predictive value for T-DM1 should be demonstrated in an adequately sized clinical cohort. Our data from NWU provides some favourable preliminary evidence and set parameters for sample size calculations for a larger study. Current studies investigating biomarkers of T-DM1 sensitivity in the metastatic setting have not included *NF1*[394,395]; collaborations are being actively pursued.
- Sensitive, reproducible and affordable assays should be developed. Given the vast heterogeneity of molecular alterations involving *NF1*, it is likely that panel-based NGS may be insufficient to achieve maximal sensitivity. We are currently testing the feasibility of an IHC-based alternative using an antibody previously tested in the context of gastrointestinal stromal tumours (GISTs)[329]. We can rely on patient cohorts with available material and NGS information, collected within ongoing trials at the institute, as: (i) the SHARP trial, a prospective interventional trial in mBC which recently concluded accrual with a total of 114 patients. As the focus was not on $HER2^+$ disease, only 7 patients were $HER2^+$ - from which three were identified as bearing somatic *NF1* mutations, and can be used to assess IHC sensitivity; ii) the Alleanza Contro il Cancro (ACC) GerSom trial, an ongoing prospective multicentric observational trial in which genetic analysis through a large NGS panel (GerSom)

is performed on paired germline-tumour samples of 4000 patients with ovarian, colorectal (aged<50) and breast (TNBC and under-40) disease.

3.5.2 Investigating the impact of *NF1* loss on tumour immune microenvironment composition and response to immunotherapy

Although largerly unexplored, *NF1* LoF may influence the tumour immune microenvironment (TIME) through distinct mechanisms. Secondary to Ras hyperactivation, two events are to be considered: PD-L1 mRNA stabilisation through MEK-ERK signalling[396], and a stricter reliance on the non-receptor protein tyrosine phosphatase SHP2 for constant GTP loading[397,398]. Inhibition of the latter has been demonstrated to increase T cell-mediated tumour killing and T cell proliferation/activation *in vitro*[399]. Its effectiveness, alone or in combination with immune checkpoint inhibition (ICPi), will be tested on the *in vivo NF1*KO models described below.

On the other hand, with the comprehensive data presented in the current study suggesting that *NF1* loss leads to CIN and aneuploidy, we can speculate that this phenotype may have a distinct susceptibility profile to ICPi or other immune modulating agents. Aneuploidy has demonstrated conflicting clinical and preclinical data regarding cytotoxic drugs, immunotherapy and multimodality treatment[400–403] sensitivity. The idea behind this controversy is that, despite triggering off inflammatory signaling by the presence of cytoplasmic DNA at first[404,405], aneuploidy does not follow arbitrarily. Long-term selection in a given microenvironment or therapeutic context can lead to amplification of a mutated oncogene or a dosage-sensitive WT gene, loss of a tumour suppressor and/or augmented mechanisms of immune evasion[392,406–408].

In the KATE2 trial, the combination of the anti-PD-L1 antibody atezolizumab to T-DM1 - which had already being credited for triggering both innate and adaptive immunity in the early setting[409,410] - was evaluated in HER2$^+$ advanced BC patients who have progressed under treatment with trastuzumab and a taxane[411]. The study did not demonstrate a clinically meaningful improvement in PFS nor OS in the intent-to-treat population at 1 year, but suggested a benefit in the latter for a subgroup of patients with PD-L1 immune cell (IC) status ≥ 1%. *NF1* status was not available. Waks AG et al. also evaluated such combination in a phase Ib trial of patients with HER2$^+$ mBC previously treated with a taxane, trastuzumab, and pertuzumab[412]. Among 20 patients who received the T-DM1 and atezolizumab combination, ORR was of 20%, with a mean PFS varying from 2.8 to 16 months, with no dose-limiting toxicities. In this small cohort, one patient (8%) carried a nonsynonimos mutation in *NF1* and sustained stable disease (SD) as best response. Here, neither PD-L1 status, TILs, TMB nor tumour ploidy correlated with response. This is a setting with limited

statistical power, where conclusions cannot be drawn. Another opportunity to look at this combination will be in the ongoing ASTEFANIA trial, a phase III study evaluating the addition of atezolizumab to the standard of care T-DM1 for patients with HER2$^+$ BC with residual disease after preoperative systemic therapy[413]. To clarify the immunomodulation secondary to *NF1* LoF, we plan to use machine learning (ML) algorithms[414] to model drug-response in correlation to aneuploidy scores, specific drug resistance- and immune evasion-related signatures from patients within the cohorts mentioned in *section 3.3.1.*

3.5.3. Expanding the role of *NF1* as a biomarker beyond HER2$^+$ BC

To investigate the hypothesis that *NF1* loss and hypersensitivity to maytansinoids may work in a tumour-agnostic manner, we are engineering multiple *NF1*KO cell lines from other BC subtypes (i.e.: luminal A, TNBC and HER2-low/ultra-low), as well as melanoma and gastrointestinal cancers, independent of HER2 expression. There is a possibility that the *NF1* role on cytoskeletal dynamics is HER2-dependent, since there is evidence of a HER2/GSK3-β/ACF7 signalling pathway controlling a specific modality of MT and F-actin crosslinking.[415–417].

3.5.4. Towards a deeper understanding of the biochemical basis of *NF1* role on microtubular dynamics

As highlighted throughout this work, the role of *NF1* on microtubular dynamics is likely to be mediated by poorly understood interactions with a complex network of cytoskeleton-binding proteins. We are currently exploring the structure-function relationship using a combination of biochemistry and forward genetics. We have successfully purified recombinant neurofibromin using a baculovirus-mediated expression system in insect cells and we have preliminary evidence showing that neurofibromin co-sediments with polymerised MTs and modulates *in vitro* tubulin polymerisation (with Eleonora Messuti, a junior PhD in the lab, and in collaboration with the IEO biochemistry unit). This reductionist *in vitro* system will allow us to identify residues responsible for neurofibromin-tubulin interaction, using CryoEM and crosslinking-based mass spectrometry, and to verify their essentiality through *in vitro* mutagenesis. A complementary approach will be through CRISPR scanning[418] using a tiling array of guides for CRISPR-based base editing, exploiting the differential sensitivity to T-DM1 in cells in which the edited base results in *NF1* LoF.

3.5.5 *In vivo* models to study metastatic potential and the tumour immune microenvironment in the absence of *NF1*

In order to interrogate the behavior of CTCs and the impact of *NF1* loss on the tumour immune microenvironment, we are generating the following models:

- A *NF1*KO syngeneic HER2^{+} mouse cell lines (EMT6). This model was recently shown to be relevant for the study of anti-HER2 ADC-induced immune activation[419].
- A transgenic conditional *NF1*KO/HER2^{+} mice. This model will allow us to investigate the impact of *NF1* loss on HER2-dependent mammary tumourigenesis, the metastatic process and immune infiltration in a native environment, without the confounding factors associated with transplantable models, which may be of particular relevance in immunology studies. The mouse will be a triple transgenic bearing MMTV-cre, MMTV-erbB2 and *NF1*$^{fl/fl}$ alleles. The conditional floxing strategy is necessary to selectively ablate *NF1* in the adult tissue of interest because constitutive *NF1*KO embryos fail to develop[420].

4. MATERIALS AND METHODS

4.1. Cell culture and generation of *NF1*KO models

BT-474, SK-BR-3 and HCC1954 cells were purchased from American Type Culture Collection (ATCC). The two formers were cultured in Dulbecco's modified Eagle's medium (DMEM, 12800-017; Gibco, Grand Island, NY, USA) while the latter in RPMI-1640 (GE healthcare, Memphis, TN, USA). Both were supplemented with 10% fetal bovine serum (FBS, 10099-141; Life Technologies, Carlsbad, CA, USA), 100 U/mL penicillin and 100 mg/mL streptomycin and kept in a humidified 5% CO_2 atmosphere at 37°C. All cells were tested regularly for mycoplasma contamination with MycoAlert (Lonza). An sgNF1 (FWD: ACGGCCTGGACCCATTCCAC; REV: GTGGAATGGGTCCAGGCCGT) targeting exon 1 was selected based on best on-target/off-target scores provided by Benchling (https://benchling.com/), San Francisco, CA, USA. The guide was cloned into pSpCas9(BB) 2A-GFP (PX458) plasmid[421], a gift from Feng Zhang (Addgene #48138). A DNA fragment containing 248nt of the *NF1* coding region of interest was PCR-amplified from single-strand cDNA obtained from parental and clonal cells using QIAquick Gel Extraction Kit (QIAGEN). Incorporation was confirmed by Sanger sequencing the amplicon. All three cell lines were subsequently transfected with the plasmid containing the *NF1* gRNA in parallel with empty vector controls using Lipofectamine 2000 according to manufacturer's instructions. Seventy-two hours later, GFP-positive cells were single-cell sorted in 96-well plates. For the ribonucleoprotein (RNP)-mediated knockout of *NF1* performed on BT-474 cells, Gene Knockout Kit v2 was ordered from Synthego (https://www.synthego.com/) and the Cas9 protein was purified in the institute, as a gift of L Rizzuti (Department of Experimental Oncology, European Institute of Oncology, Milan). RNPs were assembled and lipofected into cells following the manufacturer's instruction. After clonal expansion, knockout efficiency was analysed by western blot against neurofibromin and further characterised with NGS.

4.2. NGS-based CRISPR/Cas9 validation

Genomic DNA extraction was performed using the DNeasy Blood & Tissue Kit (Qiagen), in accordance with the manufacturer's instructions. DNA concentrations were carried out using Qubit dsDNA Broad Range quantification assay kit (Thermo Fisher Scientific). Libraries were generated using TruSight Rapid Capture kit in combination with the TruSight Cancer Sequencing Panel (Illumina) according to the manufacturer's protocol. Briefly, 50 ng of gDNA was enzymatically

fragmented and adaptor sequences were added to the ends. The tagmented DNA was amplified by PCR followed by purification. Target regions were captured with Cancer Sequencing Panel probes followed by PCR amplification and purification of the enriched library. Quantification of enriched libraries was performed with Qubit dsDNA High Sensitivity quantification assay kit (Thermo Fisher Scientific) and library size distribution was measured with Bioanalyzer 2100 and High Sensitivity DNA Kit (Agilent Technologies). Final DNA libraries sequencing was performed in Illumina NovaSeq 6000 platform using the NovaSeq 6000 S1 Reagent Kit 300 cycles (2 x 150 paired-end reads) (Illumina). Sequencing data were analysed with Illumina DRAGEN Bio-IT Platform v4.0 using proprietary pipelines for variant calling. The resulting VCF with detected variants files were were annotated and classified with the GATK-Funcotator**.**

4.3. High-throughput compound screen

BT-474^{KO} and BT-474^{WT} cells were seeded (1 x 10^4) in 96-well, white-bottom plates (Corning), in triplicates, and incubated overnight. Then, specified compounds were added in 9 dilutions plus their respective vehicle. After 96h, BrdU reagent was incorporated for additional 24h followed by fixation and detection according to manufacturer's instructions (Cell Signalling Technology, #5492). Luminescence was read using a PHERAstar FSX Microplate Reader under a 425nm wavelength. The relative response was corrected compound-wise to the average vehicle response for each replicate. Data were analyzed in GraphPad Prism 9, and IC_{50} values were generated from best-fit curves. Data represent the mean ± SD.

4.4. Competitive co-culture

- *Vectors:* the Tet-Off-H2B-GFP lentiviral vector[422] and the H2B-mCherry retroviral vector[423] were kindly provided by N Roda (Department of Experimental Oncology, European Institute of Oncology, Milan) and used in the following co-culture experiments. Tet-Off-H2B-GFP lentiviral vector was transfected in HEK293T cells together with 3rd generation packaging plasmids pMD2.G, pRSV-REV, and pMDLg/pRRE; H2B-mCherry retroviral vector was transfected in Phoenix-AMPHO cells instead. Viral supernatants were collected 2-4 days post-transfection and filtered through 0.45 mm filters. Filtered supernatants were concentrated by

ultracentrifugation at 22.000 rpm for 2h at 4°C with OptimaTM L-90K ultracentrifuge (Beckman Coulter) and stored at -80°C (never refrozen).

- *Competitive co-culture:* HCC1954^{WT} cells were infected with Tet-Off-H2B-GFP lentiviral vector while HCC1954^{KO} cells were infected with H2B-mCherry retroviral vector. Multiplicity of infection (MOI) = 2 and 8 µg/mL of Polybrene (Sigma-Aldrich) were used in both cases. Infected cells were selected via fluorescence activated cell sorting (FACS) using a BD FACSAria II. Sorted cells were subsequently mixed 1:1 and allowed to grow for up to 5 days in the presence or absence of 0.1 µg/mL of T-DM1. At day 0 (plating), 3, and 5, co-cultures were investigated by FACS to determine the fraction of wt and *NF1*KO cells. Doublets of cells and cells with abnormal morphology were excluded for the analysis.

To assess the effect of T-DM1 treatment on cell cycle distribution, harvested cells were fixed with 70% cold ethanol (Panreac Applichem) in PBS (Thermo Fisher Scientific), and stored at 4°C. After 8h, cells were centrifuged and resuspended in PBS (Thermo Fisher Scientific). DAPI (Sigma-Aldrich) was then added at the final concentration of 50 µM overnight at 4°C. Cell cycle distribution was analysed by FACS and differences in cell cycle distribution were evaluated through the χ^2-test.

4.5. Colony formation assay

Duplicates of 6 x 10^2 HCC1954^{WT} or HCC1954^{KO} cells were seeded in 12-well-plates and left undisturbed at 37°, 5% CO_2 for 4 days. Then, cells were treated with vehicle control (DMSO for DM1 and rituximab for both ADCs), T-DM1, DM1 or T-DXd at the indicated concentrations for 21 days, with weekly change of spent media. At the end of treatment, cells were washed twice with ice-cold PBS and fixed with ice-cold methanol for 15 min. Afterwards, 0.5% crystal violet solution (Sigma V5265) was added to the plates and incubated at room temperature for 15 min. Plates were then washed with ddH_2O, until the unbound crystal violet was removed and plates were dried at room temperature. Images were processed using the ColonyArea ImageJ plugin[250].

4.6. Active Ras pull-down

Levels of active Ras were determined using the Active Ras Detection Kit (#8821, Cell Signalling Technology). Briefly, cell lysates (500 µL at 1 mg/mL) were treated *in vitro* with GTPγS or GDP to activate or inactivate Ras, respectively. The lysates were then incubated with glutathione resin and GST-Raf1-RBD for 1h at 4°C, washed and the resulting RAS-RAF1 complexes eluted from the resin by boiling in 2X SDS sample buffer. Proteins were resolved by SDS-PAGE, transferred to nitrocellulose and western blot analysis (20 µL of the eluted samples) was performed using the anti-RAS antibody supplied by the manufacturer. An anti-mouse IgG, HRP-linked Antibody (#7076) was used as the secondary antibody.

4.7. Ras^{G12V} overexpression

KRASG12V from pDONR223_KRAS_p.G12V (Addgene #81665) was cloned on the lentiviral backbone pLenti CMV hygro dest (Addgene #17454), a gift from C Toscani (Department of Experimental Oncology, European Institute of Oncology, Milan). HEK293T cell transfection and infection of target cells were performed as in 2.5, followed by hygromycin B (InvivoGen) 0.5 mg/mL selection for 8 days.

4.8. Growth curves

Cells were plated in triplicate at a density of 2×10^5 cells/well for BT-474 and 1×10^5 cells/well for HCC1954 in 12-well plates. After 24h, cells were treated with control (rituximab 10 µg/mL or DMSO), trastuzumab (10 µg/mL), T-DM1 (0.1 µg/mL), mertansine (5 nM) or T-DXd (0.1 µg/mL). For time point 0 (24h after seeding), and subsequently for all other time points (day 2, day 4, day 6, and occasionaly day 8), cells were washed twice with PBS, trypsinized, counted using a hemocytometer and then treated again with fresh media containing the respective drugs. Cell counting was normalised according to the number of cells at day 0.

4.9. Immunoblot analyses

Cells were lysed in RIPA buffer (20 mM TrisHCL, pH 7.6; 5 mM EDTA; 150 mM NaCl; 0.5% NP-40; 50 mM NaF; 1 mM beta-glycerophosphate) supplemented with PhosSTOP (Roche) and protease inhibitors (Roche). A protein fraction was obtained by centrifuging at 10.000 × g for 30 min at 4 °C. Supernatant was collected and protein concentration was determined using the Pierce™ BCA

protein assay kit following manufacturer's instructions (Thermo Fisher Scientific, Massachusetts, USA). Each sample was separated by non-reducing SDS-PAGE with Precision Plus Protein Dual Color Standards (Bio-Rad) and transferred to nitrocellulose membrane overnight at 4 °C. Where applicable, western blots were cut horizontally to allow the detection of different proteins within a single experiment**.** Blots presented in figure panels were derived from the same experiment and processed in parallel. The rest of the antibodies utilised herein are: rabbit anti-cleaved PARP (Asp214, D64E10, XP® 5625); mouse anti-Bcl-2 (100/D5); mouse anti-GAPDH (6C5); rabbit anti- β-Tubulin (9F3); rabbit anti-E-Cadherin (24E10); rabbit anti- Occludin (E6B4R); rabbit anti-β-Catenin (9562); mouse anti-EpCAM (VU1D9); mouse anti-vinculin (A250291); rabbit anti-KIFC1 (11445); rabbit anti-KIF11 (PA5115164); mouse anti-p150 (610474); mouse anti-CRPM2 (C4G); rabbit anti-phospho-GSK-3α/β (Ser21/9, 9331), and rabbit anti-CDK5 (2506). Donkey anti-mouse IgG or goat anti-rabbit IgG secondary antibody conjugated to horse-radish peroxidase (Jackson ImmunoResearch Laboratories, Inc., Pennsylvania, USA) were probed against primaries overnight at 4 °C and detected bands were visualised using ECL reagent (Novex™ ECL Chemiluminescent Substrate Reagent Kit, Thermo Fisher Scientific, Massachusetts, USA) and processed using Image Lab™ software 6.0.1 (Bio-Rad).

4.10. CETSA melting curves

Growing BT-474 cells were harvested, washed once with PBS, and diluted in Hanks' Balanced Salt Solution (HBSS, Thermo Fisher Scientific) supplemented with PhosSTOP (Roche) and protease inhibitors (Roche) to 4 x 10^6 cells/mL. The cell suspension was then mixed with DMSO or DM1 1 µM and kept on a wheel at 37°C for 2.5 h before aliquoting into PCR-tubes. Melting curves were generated by heating samples for 3 min in a Veriti Thermal cycler (Applied Biosystems) at the following stepwise temperature range: 57°C, 59°C, 61°C, 63°C, 65°C, 67°C. Cells were subsequently lysed with three rounds of freeze-thaw by alternating exposure of the samples to liquid nitrogen and 20°C in a PCR-machine. Samples were then resolved by SDS-PAGE gel, transferred to nitrocellulose and analysed by immunoblotting against β-tubulin (9F3). For the quantitative analysis, we first normalised mean band intensities obtained for temperatures within our range on the mean band intensity obtained at the starting temperature (57°C), considering the treatment (DMSO or DM1). To understand which factors affected most the differences observed in *figure 8*, we performed a two-way ANOVA separately for BT-474^{WT} and BT-474^{KO} normalised data. We considered as factors the treatment, the temperature and their combination.

4.11. RNA-seq

mRNA-seq libraries were prepared according to the TruSeq low sample protocol (Illumina, San Diego, CA, USA), starting with 1 µg of total RNA per sample and pair-end sequenced on an Illumina NovaSeq 6000 sequencing platform. Data were mapped using the STAR aligner version 2.7.1a[424] against the human genome (hg19)[425]. Read counts were calculated with htseq-counts[426]. Differential analysis has been done via DESeq2 R package version 1.36.0[427] and genes of interest were selected using a false discovery rate (FDR) cut-off of 1 x 10^{-4}[428]. Functional enrichment analysis was performed using EnrichR R package version 3.1[257,429,430] on differentially expressed genes (DEGs) with log2foldchange < -1 in BT-474^{KO} treated with T-DM1 *vs* BT-474^{KO} treated with vehicle and log2foldchange > -1 and < 1 in BT-474^{MOCK} treated T-DM1 *vs* BT-474^{MOCK} treated with vehicle. Queries were performed over four different molecular signatures: Gene Ontology Biological Process, Gene Ontology Molecular Function, Gene Ontology Cellular Component (*https://www.gsea-msigdb.org/gsea/msigdb/download_file.jsp?filePath=/msigdb/release/2022.1.Hs/c5.go.v2022.1.Hs.symbols.gmt*) and Hallmark (*https://www.gsea-msigdb.org/gsea/msigdb/download_file.jsp?filePath=/msigdb/release/2022.1.Hs/h.all.v2022.1.Hs.symbols.gmt*)[431–433]. Enriched terms were selected using a standard FDR cut-off of 1x10^{-2}. Hierarchical clustering analysis was performed using the gene expression values from Hallmark mitotic spindle molecular signature. Specifically, we used Ward's criterion for genes with 1 - (correlation coefficient) as a distance measure and clustering heatmap was drawn using z-score across samples for each gene[428].

4.12. Single-cell fate analysis using FUCCI(Ca) cell cycle reporter

- *Model generation and data acquisition:* 293T cells were co-transfected with the pCSII-EF-MCS vector encoding the FUCCI(Ca)[258] probe (**figure M1A**) with the packaging plasmid (pCAG-HIVgp) and the VSV-G-/Rev-expressing plasmid (pCMV-VSV-G-RSVRev). High-titer viral solutions were prepared and used for transduction into both BT-474^{WT} and BT-474^{KO} cells by two rounds of infection of 4 viral particles per cell (MOI = 1) followed by FACS (FACSAria cell sorter, BD) all positive events. For live-cell imaging, 0.5 x 10^5 cells were seeded in µ-Slide 8-well glass bottom chambers (80827, Ibidi). Twenty-four hours later, T-DM1 or control (rituximab) were added at

the indicated concentrations 30 min before starting acquisition. Images were acquired with a Spinning Disk Confocal Microscope (Nikon) at 10x for 90h.

- *Database generation:* for each experimental condition, we tracked cells in the mCherry and mVenus channels using TrackMate 7.2.0[434,435] on nine different fields of view (FoV), for a maximum of 530 frames, 10 min apart from each other, over 90h. Only cells that remained alive for at least 12h were followed by the tracker. For those, intensities on both channels were measured for each time frame starting from time 0 (T0).

- *Preprocessing:* we first removed cells showing channel intensities lower than 200 for all the observed time lapse. Then, we applied a sliding average (window width = 5 points) to reduce noise and to smooth intensity signaling.

- *Algorithm to identify cell cycle phase:* this was developed in collaboration with G Tini, a mathematician within the lab. Using the the sliding average values of both channel intensities for a cell of interest as input, we identified the cell cycle phase (G1, S, G2/M) for each time point in the observed time lapse. To train our algorithm, we randomly selected three FoV for each condition, removing FoV with clusters of cells difficult to identify. Following the FUCCI(Ca) fluorochrome architecture[258], we will refer to the G1 phase as "Red" (R), the S phase as "Green" (G), and the G2/M phase as "Yellow" (Y). The first step is the identification of preliminary R and G frames, considering the channel intensities: if R>G, the frame is classified as R, otherwise as G. Integrating the behaviour of channel intensities with tracker movies, we observed that the G2/M phase corresponds to a sharp increase in the red channel intensity when the cell is still in the S phase, matching to a decrease in the green channel intensity. The G2/M phase stops whit a sharp decrease of the green channel intensity coupled with an increase in the red channel intensity, which determines the G1 entry. We thus set several rules to identify G2/M frames, studying the derivatives of red and green intensities for each frame x_i at time point i ($d_{red}(x_i)$ and $d_{green}(x_i)$).

  We classified as Y the frames x_j where:

  - $d_{red}(x_i) > 1$ and x_j was previously classified G. To avoid the identification of small fluctuation as Y, we selected only groups of consecutive frames longer than 6 (equivalent

to an hour) or, if none of those sequence is available, we selected only the longest sequence of consecutive frames;

- $d_{red}(x_{i-1}) < 1$ and i is the last available time point;
- $d_{green}(x_i) < (-5)$ and x_i was previously classified as R;
- $d_{green}(x_i) < (-1)$ with x_i previously classified as G and $i > j$ where $j = \max_k\{x_k \text{ such that } x_k \text{ is classified as Y}\}$

After that, each frame is classified as Y, G or R. We then checked frame by frame whether the order of phases in the cell cycle (G1 → S → G2/M) was respected. Residual misclassifications were further fixed with the following set of rules:

- in YGG sequences, the first G is replaced by Y;
- in YGY sequences, G is replaced by Y;
- in RY sequences, Y is replaced by R;
- in RGR sequences, G is replaced by R.

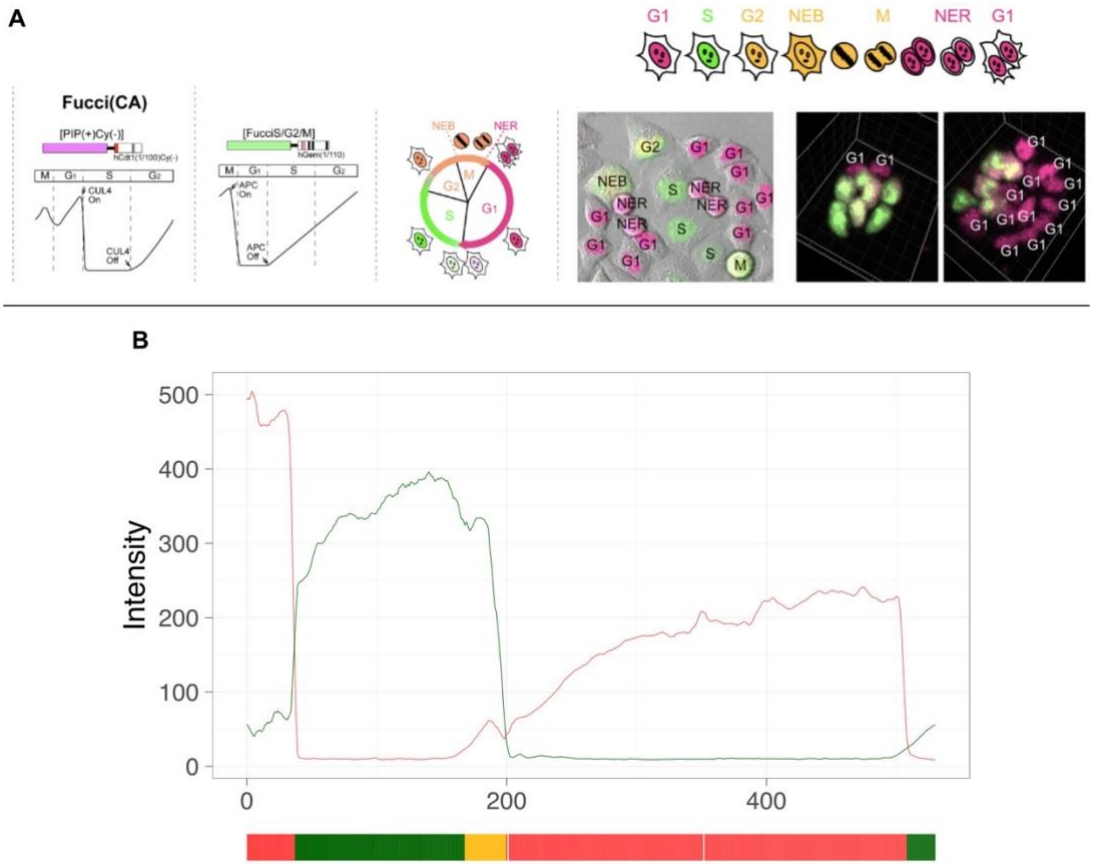

Figure M1. A. Schematic representation of the FUCCI(CA) system with its domain structure consisting of a $CUL4^{Ddb1}$-sensitive hCdt1-based probe and an APC^{Cdh1}-sensitive hGem-based

probe that labels nuclei in G1, S, and G2 phases with red (mCherry), green (mVenus), and yellow (mCherry + mVenus) fluorescence, respectively; **B.** Output intensity levels of mCherry (red curve) and mVenus (green curve) of a tracked cell. The intensities were measured at specific time points, taken every 10 minutes and represented on the x axis. The colored stripe below the x axis represents the cell phase identified for the corresponding time interval: red for G1, green for S, and yellow for G2/M. Modified from Sakaue-Sawano A et al.[258].

- *Analysis of identified cell cycle phases:* we applied our algorithm to all the available FoV for each condition. Once we assigned a phase to each frame, we dissected the complete cell cycles identified. Then we compared the percentage of frames assigned to the G2/M phase in *NF1*KO cells (vehicle, T-DM1 0.1 μg/mL and T-DM1 1 μg/mL) with the corresponding percentage in the wt population. We used one-tailed Wilcoxon test for statistical analysis.

4.13. β-Galactosidase staining

In parallel with live-cell imaging, FUCCI(Ca)-tagged BT-474^{WT} and BT-474^{KO} cells were seeded at low-density in 6-well plates and treated with vehicle, T-DM1 (0.2 μg/mL) or doxorubicin (200nM) as positive control, for the same 90h. The senescence β-Galactosidase staining kit (#9860, Cell Signaling Technology) was used according to manufacturer's instructions**.** Images were evaluated using Invitrogen™ EVOS™ XL Core microscope through a 10X 0.4 NA air objective. All images were analysed using imageJ software; the signal of the stained cells was extrapolated using Colour Deconvolution2 plugin and the Integrated density was evaluated for each FoV.

4.14. Mouse xenograft models

- *Engineering of Luc-tagged HCC1954 cells (HCC1954-Luc) and tumour implantation*: the pLenti CMV Puro LUC (w168-1) was purchased from Addgene (#17477) and used in all *in vivo* experiments. This 3rd generation lentiviral vector allows for the constitutive expression of firefly luciferase under the CMV promoter. The vector also contains genes that encode for puromycin and ampicillin resistance. Both HCC1954^{WT} and HCC1954^{KO} cells were transduced with the pLenti CMV Puro LUC reporter vector at MOI = 5 in the presence of 8 μg/mL of Polybrene (Sigma-Aldrich). Infected cells were selected by puromycin (2.5 μg/mL for 72h; Vinci-Biochem) and allowed to expand for additional 8 days post selection. Tumours were implanted in 9-week-old

NOD scid γ (NSG) mice, acquired from Charles River Laboratories) by intra-fat pad orthotopic injection of 10^6 HCC1954^{WT}-Luc on the 9th mammary gland – left; and 10^6 HCC1954^{KO}-Luc on the 5th - right) resuspended in sterile PBS (Thermo Fisher Scientific) and pre-mixed at a 1:1 dilution with growth-factor-reduced Matrigel (Corning) in a total volume of 30 µL. Tumour volume was weekly assessed via bioluminescence imaging (BLI) (IVIS-Lumina, Perkin Elmer). On day 14, once tumours were palpable (≥4 mm^3), mice received a single intravenous injection of 4 mg/kg T-DM1 or NaCl 0.9%. Mice were weighed when cells were implanted (Day 0) and then twice weekly during the study. Experiment was terminated after 35 days.

- *Bioluminescence imaging (BLI), acquisition and analysis:* the images were acquired using PerkinElmer's IVIS Lumina Series III instrument wavelengths (600- 800 nm). Scans were taken with an integrated CCD camera (Andor, Belfast, UK) supercooled down to −80 °C, with a 25 mm focal length lens (Navitar, Rochester, NY). The camera pointed straight down and was focused 10 mm above the imaging membrane. The F-number was kept at f/0.95 throughout the study. Prior to imaging, 200 µL of D-Luciferin (10 mg/mL, XenoLight, Perkin Elmer) were injected intraperitoneally and mice were anesthetized in induction chambers with 1-4% isofluorane. With animals in the supine position, BLI images were acquired after 10 min after luciferin injection. An exposure time of 2s and binning of 4 was used at the beginning of the study, and imaging parameters were updated as the tumours became brighter throughout the study, in order to maximize sensitivity of bioluminescence and avoid pixel saturation. Tumour burden was represented as total flux (photons/s), which is average radiance (flux per unit area and unit solid angle) integrated over the region of interest, using the Living Image v4.7.3 in vivo software package (Perkin Elmer Inc).

4.15. ctDNA collection and analysis

- *Patient population:* under a prospective clinical trial (a single Institution Investigator Initiated Trial (IIT); protocol number: NU16B06), we analysed blood samples of patients with mBC enrolled before starting a new line of therapy. Samples were collected from patients treated at the Northwestern University (Chicago, IL) between 2016 and 2021. The main information collected for each patient was demographic and clinical information about diagnosis,

recurrences, treatments (chosen according to the best clinical practice), and follow-up. A written informed consent was obtained from each participant for ctDNA draws.

- *ctDNA analysis:* Guardant Health performed the plasma analysis (Guardant360). The test was designed to analyse ctDNA in 5 to 10 mL of blood. Two 10 mL standard Streck tubes of whole blood were used for each patient. The plasma was stored at room temperature for 24 to 48h before the final analysis. We used 5 to 30 ng of ctDNA for the sequencing (sample requirements >5 ng cell-free DNA) and the mean amount was 22 ng. Guardant360 sequencing technique is based on NGS technology (Guardant Digital Sequencing) with a single molecule analytical sensitivity and a 99.9999% specificity. It detects various types of alterations, including single nucleotide variants (SNV), insertions/deletions (indels), gene fusions/rearrangements and copy number variations (CNV) present in genes linked to cancer (clinical actionable mutations, including *NF1*) with a reportable range of ≥0.04%, ≥0.02%, ≥0.04%, and ≥2.12 copies, respectively. The genomic analysis was performed at a central CLIA (Clinical Laboratory Improvement Amendments)-certified laboratory (Guardant Health).

4.16. Immunofluorescence and confocal microscopy

- *Internalisation assay:* three batches of 7.5 x 10^5 BT-474 cells were seeded on 0.5% gelatin-coated coverslips and allowed do attach overnight. After a 15 min T-DM1 or T-DXd pulse (1.5 µg/mL), drugs were washed off and one batch of cells was immediately fixed with PFA 4% for 15 min RT and analysed for baseline membrane impregnation. The remaining batches received fresh warm media and were incubated at 37°C for 24 h, with or without chloroquine (CQ, 5 µM). Cell were then fixed as previously described and all three batches were permeabilised with Triton X-100 0.5% in PBS and a Cy5-conjugated anti-human (AC112S, Sigma) was used for the detection of T-DM1 and T-DXd; a FITC-phalloidin (P5282, Sigma) was used for actin and nuclear counterstaining was done with DAPI. Images were acquired with an SP8 confocal microscope (Leica Microsystems GmbH, Wetzlar, Germany) and a 63x/1.4NA oil immersion objective lens. Multichannel, Z-stack images were acquired with a voxel size of 72x72x200 nm^3 by 3 different PMT detectors. To determine internalisation, single cells

were segmented and the mean cytosol fluorescence signal of each single cell was evaluated (n = 28). Statistical analyses were performed using the Student's *t*-test, two-tailed.

- *Chromosome misalignment analysis and centriolar quantification:* BT-474^{WT} and BT-474^{KO} cells were seeded as per internalisation assay. After 24h, cells were synchronised with RO3306 (Sigma-Aldrich) at 9 µM for 39 or 22.5h, respectively (half their doubling time[436]) at 37°C. Cells were then washed three times with warm media for late G2 block release and put back at 37°C. After 50 min, cells were treated with MG-132 (Tocris) 10 µM for 90 min at 37°C. Finally, cells were fixed either by immersion in cold methanol at -20°C for 4 min followed by rehydration in PBS for 10 min or with 4% paraformaldehyde (PFA) for 15 min followed by permeabilisation with 0.5% Triton X-100 for 20 min. For double thymidine block (DTB), SK-BR-3 cells were grown to a 40% confluence instead and 2 mM of thymidine was added. After incubation at 37°C for 18h, cells were washed with PBS and put back in culture with fresh media for 9h. After that, thymidine was added again for another 15h. Cells were then washed three times with warm media for release and fixed after 8h with 4% paraformaldehyde. Fixed cells were all blocked with 3% BSA for 1h and incubated in primary antibodies diluted in PBS-Tween20 0.1%, 3% BSA and 0.02% NaN_3. Primary antibodies used for immunofluorescence (IF) analysis included mouse anti-a-tubulin (T5168), human anti-centromere protein (15-234), rabbit anti-phospho-histone H3(Ser10) (06-570), and rabbit anti-CEP63 (06-1292). Primary antibodies were detected using Alexa Fluor-labelled secondary antibodies (Life Technologies) while DAPI (D9542) was used for nucleic staining. Coverslips were mounted using Mowiol and images were achquired as previously reported. Cell phenotypes were scored visually by counting non-overlapping FoVs in a raster scan pattern across the coverslip.

- *Chromosomal and microtubular dynamics during mitosis*: BT-474^{WT}-H2B-GFP and BT-474^{KO}-H2B-mCherry cells were seeded (40 x 10^3 cells) in µ-Slide 8-well glass bottom chambers (80827, Ibidi). Twenty-four hours later, growing cells were stained for 1.5h before acquisition with the SiR-tubulin probe (#SC002, Spirochrome; λabs 652 nm/λfl 674 nm) at 1 µM. Time-lapse microscopy was performed using an inverted microscope (Nikon Eclipse Ti) with a 20X objective. The microscope was equipped with an incubation chamber maintained at 37°C in

an atmosphere of 5% CO_2 and acquisitions were made every 4 min. A total of 28 cells were analysed for BT-474^{WT} and 38 for BT-474^{KO}.

- *Cold-induced depolymerisation assay:* HCC1954 cells were grown overnight on 0.5% gelatin-coated coverslips at 37°C. The cultures were then shifted to an incubator at 4°C for 1h. After that period, one batch of cells was immediately fixed with ice-cold methanol (T0), while the other two were returned to 37°C incubation with pre-warmed media for 2 (T2) and 15 (T15) min. After fixation of all three batches, cells were stained with anti-a-tubulin (Sigma, T5168; 1:1000) and costained with DAPI.

- *GTP-bound tubulin live-cell permeabilisation, staining and analysis:* a 1:1 coculture of HCC1954^{WT} and HC1954^{KO} cells was grown at 37°C, 5% CO_2 until ~70% confluence. Culture medium was then replaced by warm permeabilisation buffer (80 mM PIPES, 1 mM EGTA, 1 mM MgCl2, 10% glycerol, 0.03% Triton X-100, pH 6.9) and incubate for 3 min at 37°C. After two cautiously 1s washes with PEM-G buffer (80 mM PIPES, 1 mM EGTA, 1 mM MgCl2, 10% glycerol + taxol 1 mM), coverslips were directly put, facing down, on drops of human anti-MB11 (AdipoGen), in a wet chamber at 37°C, and incubated for 15 min. After 3x gentle washes with PEM-G buffer, coverslips were put on anti-human secondary antibody drops, in the same humid chamber at 37°C, for another 15 min. After washing once with PEM-G, cells were fixed with cold methanol (-20°C) for 4 min. After washing once with 1x PBS, cells were colabeled with anti-a-tubulin (T5168) and DAPI. Images were acquired under the same microscopical conditions as per internalisation assay. Analysis were performed with Python 3.8, using the following workflow:
    - Segmentation of cells

      Segmentation of tubulin signal: by Gamma correction with exponent 0.1 and Gaussian Blur 5.0 to make signal more homogeneous followed by segmentation with Cellpose with pre-trained model "cyto" (https://github.com/mouseland/cellpose). Flow threshold 3.5 and cellular diameter 200px were used. Other paramethers left at their default value.

      Segmentation of nuclei: background correction with rolling ball 100px, Gamma correction with exponent 0.1, Gaussian Blur 7.0 and segmentation with Otsu algorithm.
    - Filters on nuclear segmentation

1. Removal of superposed green and red nuclei;
2. Removal of small objects (errors in segmentation). Removal of objects with area < 4000 px^2;
3. Fill Holes in case of inhomogeneus nuclear segmentation;
4. Watershed correction to divide touching nuclei. Nuclei radius parameter set at 80px;
5. Removal of small objects (errors in watershed) and with high eccentricity (elongated ellipses). Removal of objects with area < 4000 px^2 and eccentricity >0.85.

- Filters on nuclei inside cells

  Remove a nucleus if:

  1. It is shared by 2 cells;
  2. There is a single nucleus inside a cell and it is small (errors in segmentation + external nucleus "invading" a cell);
  3. The area of the nucleus is the same size as the area of the cell (errors in segmentation);
  4. The nucleus is not inside a segmented cell;
  5. If nuclei of different colours are found within the same cell. Two nuclei with same colour inside the same cell are accepted.

- Properties

  Nuclei are associated to the cell they belong to. It is therefore possible to have multiple nuclei of the same color within the same cell. Cells without a nucleus inside are not taken into account. For every coupled cell/nucleus (or nuclei), the nuclear, cytoplasmic and cellular mean intensity of tubulin and GTP-bound tubulin are printed.

- Data analysis

  GTP-bound tubulin signal and ration GTP-bound tubulin/α-tubulin were compared, removing outliers using the Wilcoxon signed-rank test.

4.17. Autophagy activity

1 x 10^6 cells, *NF1*KO and their respective parentals, were seeded in 60 mm plates and let grow overnight. DM1 was added to the media for 12h (1 nM for BT-474; 0.1 nM for HCC1954 and 0.01 nM for SK-BR-3), with CQ added during the last 4h. Cells were then scrapped with RIPA buffer,

lysed on ice for 30 min and proceeded with standard western blot as previously described using a 14% gel. LC3B protein (I and II) was analysed with the rabbit anti-LC3B (L7543).

4.18. Polyploidy assessment

BrdU was pulsed for 1h on growing BT-474^{WT} and BT-474^{KO} cells before fixation and staining according to manufacturer's instructions (FITC BrdU Flow Kit, BD Biosciences). Samples were manually loaded, with acquisition criteria of 10.000 events or 3 minutes for each tube. Data was analysed using FlowJo x.10.0.7r2 software (Tree Star).

4.19. Aneuploidy estimation from AACR-GENIE dataset

AACR-GENIE data were retrieved from GENIE cbioportal webserver version 13.0 public (https://genie.cbioportal.org/) and filtered for BC samples (n = 15210). We further selected those that had been sequenced with the following *NF1*-containing panels: MSK-IMPACT341, MSK-IMPACT410, MSK-IMPACT468, GRCC-MOSC3, UCSF-NIMV4-TN, UCSF-NIMV4-TO. Resulting sample size was 6598. Of these, 290 consisted of *NF1* mutated patients. Aneuploidy scores (AS) were quantified on segmentation data downloaded from cBioPortal using ASCETS (Arm-level Somatic Copy-number Events in Targeted Sequencing)[285]. ASCETS was run using UCSC cytoband coordinates (reference build hg19) provided in the ASCETS *github* repository (https://github.com/beroukhim-lab/ascets/blob/master/cytoband_coordinates_hg19.txt). AS was calculated with standard parameters with a minimum depth of coverage of 0.5 and alteration threshold of 0.7.

4.20. Atomic force microscopy (AFM)

BT-474^{WT} and BT-474^{KO} cells growing at ~50% confluence in phenol-red free, 25mM HEPES-complemented media (Lonza) were analysed (13-20 cells per condition), generating ~200/300 force-distance curves per cell. Loading force was applied above the nuclear region with a spheroidal colloid probe (Pr1: R = 3499 nm, K = 0.0208 N/m) at a ~2-3 µm median indentation. From each curve, topography/mechanical maps were reconstructed[437]. All measurements were conducted at room temperature (~25 °C) on a with a Bioscope Catalyst AFM (Bruker) equipped with a Nanoscope V controller, by means of the force volume technique, with the following parameters: 64 × 64 force

curves, each of them characterised by 2048 points, a ramp length L = 5 µm, a maximum applied force F ≈10–15 nN, a global ramp frequency f = 7.10 Hz composed by an approaching velocity vappr = 43.4 µm/s, and a retracting velocity vretr = 195 µm/s. Cantilever was calibrated before all acquisitions using thermal noise amplitude analysis[438,439].

ACKNLOWLEDGEMENTS

I would like to, first of all, thank Luca Mazzarella, for doing the seemingly impossible job of incarnating one perfect balance between a PI and a good friend. He gave me sharp, honest criticism when needed as well as freedom and encouragement to persue my own ideas; and believe me, this is a gem. His wits were fundamental for writting this thesis - perhaps especially, when he did not agree with what/how I have written it.

To all the members of the Laboratory of Translational Oncology at IEO and external collaborators - which, luckily, are too many for single references and due tributes. My humble appreciation for your unsparing insights and genuine will for making science together. To all the facilities who took never ending experimental schemes from my part without a glimpse of hesitation, my full admiration and gratitude.

To Fabrice André and Marina Mapelli, from whom I completely concealed the option of saying no to being my examiners.

To my merciful friends, hoping they have not given up on me for good.

And finally, to my other half on this life, my wife Camila, who is an endless source of forbearance, covered in righteous questions like “when are you going to finish that #&!* thesis?”; and to my 1-day old daughter Yolanda, who just made me rediscover love. You inspire me in ways you cannot even imagine.

From a piece of Lewis Thomas’ The Lives of a Cell (1993), one of the books that changed my understanding of what we do:

> *“Stigmergy” is a new word, invented recently by Grassé to explain the nest-building behaviour of termites, perhaps generalisable to other complex activities of social animals. The word is made of Greek roots meaning “to incite to work”, and Grassé’s intention was to indicate that is the product of work itself that provides both the stimulus and instructions for further work.*

If the air is right, let new questions interrupt us and tumbling activities begin once more, out of control all over again.

REFERENCES

1. Lima, S. M., Kehm, R. D. & Terry, M. B. Global breast cancer incidence and mortality trends by region, age-groups, and fertility patterns. *eClinicalMedicine* **38**, 100985 (2021).
2. Sung, H. *et al.* Global Cancer Statistics 2020: GLOBOCAN Estimates of Incidence and Mortality Worldwide for 36 Cancers in 185 Countries. *CA. Cancer J. Clin.* **71**, 209–249 (2021).
3. Arnold, M. *et al.* Current and future burden of breast cancer: Global statistics for 2020 and 2040. *The Breast* **66**, 15–23 (2022).
4. Anderson, B. O. *et al.* The Global Breast Cancer Initiative: a strategic collaboration to strengthen health care for non-communicable diseases. *Lancet Oncol.* **22**, 578–581 (2021).
5. Perou, C. M. *et al.* Molecular portraits of human breast tumours. *Nature* **533**, 747–752 (2000).
6. Sørlie, T. *et al.* Gene expression patterns of breast carcinomas distinguish tumor subclasses with clinical implications. *Proc. Natl. Acad. Sci.* **98**, 10869–10874 (2001).
7. Curtis, C. *et al.* The genomic and transcriptomic architecture of 2 , 000 breast tumours reveals novel subgroups. *Nature* **486**, 346–352 (2012).
8. Dawson, S. J., Rueda, O. M., Aparicio, S. & Caldas, C. A new genome-driven integrated classification of breast cancer and its implications. *EMBO J.* **32**, 617–628 (2013).
9. Ali, H. R. *et al.* Genome-driven integrated classification of breast cancer validated in over 7,500 samples. *Genome Biol.* **15**, 431 (2014).
10. Russnes, H. G., Lingjærde, O. C., Børresen-Dale, A. L. & Caldas, C. Breast Cancer Molecular Stratification: From Intrinsic Subtypes to Integrative Clusters. *Am. J. Pathol.* **187**, 2152–2162 (2017).
11. Aure, M. R. *et al.* Integrative clustering reveals a novel split in the luminal A subtype of breast cancer with impact on outcome. *Breast Cancer Res.* **19**, 44 (2017).
12. Bartlett, J. M. S. *et al.* Comparing Breast Cancer Multiparameter Tests in the OPTIMA Prelim Trial: No Test Is More Equal Than the Others. *J. Natl. Cancer Inst.* **108**, djw050 (2016).
13. Burstein, H. J. *et al.* Customizing local and systemic therapies for women with early breast cancer: the St. Gallen International Consensus Guidelines for treatment of early breast cancer 2021. *Ann. Oncol.* **32**, 1216–1235 (2021).
14. Andre, F. *et al.* Biomarkers for Adjuvant Endocrine and Chemotherapy in Early-Stage Breast Cancer: ASCO Guideline Update. *J. Clin. Oncol.* **40**, 1816–1837 (2022).

15. Bianchini, G., De Angelis, C., Licata, L. & Gianni, L. Treatment landscape of triple-negative breast cancer — expanded options, evolving needs. *Nat. Rev. Clin. Oncol.* **19**, 91–113 (2022).
16. Jiang, C., Perimbeti, S., Deng, L., Shapiro, C. L. & Gandhi, S. Clinical outcomes of de novo metastatic HER2-low breast cancer: a National Cancer Database Analysis. *npj Breast Cancer* **8**, 135 (2022).
17. Allison, K. H. & Wolff, A. C. ERBB2-Low Breast Cancer—Is It a Fact or Fiction, and Do We Have the Right Assay? *JAMA Oncol.* **8**, 610 (2022).
18. Modi, S. *et al.* Trastuzumab Deruxtecan in Previously Treated HER2-Low Advanced Breast Cancer. *N. Engl. J. Med.* **387**, 9–20 (2022).
19. Guarneri, V. *et al.* HER2DX genomic test in HER2-positive/hormone receptor-positive breast cancer treated with neoadjuvant trastuzumab and pertuzumab: A correlative analysis from the PerELISA trial. *eBioMedicine* **85**, 104320 (2022).
20. de Haas, S. L. *et al.* Tumor biomarkers and efficacy in patients treated with trastuzumab emtansine + pertuzumab versus standard of care in HER2-positive early breast cancer: an open-label, phase III study (KRISTINE). *Breast Cancer Res.* **25**, 2 (2023).
21. Tang, M. *et al.* Treatment patterns and survival in HER2-positive early breast cancer: a whole-of-population Australian cohort study (2007–2016). *Br. J. Cancer* **121**, 904–911 (2019).
22. Loibl, S., Poortmans, P., Morrow, M., Denkert, C. & Curigliano, G. Breast cancer. *Lancet* **397**, 1750–1769 (2021).
23. Yang, S. X., Hewitt, S. M. & Yu, J. Locoregional tumor burden and risk of mortality in metastatic breast cancer. *npj Precis. Oncol.* **6**, 22 (2022).
24. Siegel, R. L., Miller, K. D., Wagle, N. S. & Jemal, A. Cancer statistics, 2023. *CA. Cancer J. Clin.* **73**, 17–48 (2023).
25. Oh, D.-Y. & Bang, Y.-J. HER2-targeted therapies — a role beyond breast cancer. *Nat. Rev. Clin. Oncol.* **17**, 33–48 (2020).
26. Shah, C., Al-Hilli, Z. & Vicini, F. Advances in Breast Cancer Radiotherapy: Implications for Current and Future Practice. *JCO Oncol. Pract.* **17**, 697–706 (2021).
27. Giordano, S. H. *et al.* Systemic Therapy for Advanced Human Epidermal Growth Factor Receptor 2–Positive Breast Cancer: ASCO Guideline Update. *J. Clin. Oncol.* **40**, 2612–2635 (2022).

28. Gennari, A. *et al.* ESMO Clinical Practice Guideline for the diagnosis, staging and treatment of patients with metastatic breast cancer. *Ann. Oncol.* **32**, 1475–1495 (2021).
29. Ramakrishna, N. *et al.* Management of Advanced Human Epidermal Growth Factor Receptor 2–Positive Breast Cancer and Brain Metastases: ASCO Guideline Update. *J. Clin. Oncol.* **40**, 2636–2655 (2022).
30. Verma, S. *et al.* Trastuzumab Emtansine for HER2-Positive Advanced Breast Cancer. *N. Engl. J. Med.* **367**, 1783–1791 (2012).
31. Amiri-Kordestani, L. *et al.* FDA Approval: Ado-Trastuzumab Emtansine for the Treatment of Patients with HER2-Positive Metastatic Breast Cancer. *Clin. Cancer Res.* **20**, 4436–4441 (2014).
32. Cortés, J. *et al.* Trastuzumab Deruxtecan versus Trastuzumab Emtansine for Breast Cancer. *N. Engl. J. Med.* **386**, 1143–1154 (2022).
33. Hurvitz, S. A. *et al.* Trastuzumab deruxtecan versus trastuzumab emtansine in patients with HER2-positive metastatic breast cancer: updated results from DESTINY-Breast03, a randomised, open-label, phase 3 trial. *Lancet* **401**, 105–117 (2023).
34. Powell, C. A. *et al.* Pooled analysis of drug-related interstitial lung disease and/or pneumonitis in nine trastuzumab deruxtecan monotherapy studies. *ESMO Open* **7**, 100554 (2022).
35. Jabbour, E., Paul, S. & Kantarjian, H. The clinical development of antibody–drug conjugates — lessons from leukaemia. *Nat. Rev. Clin. Oncol.* **18**, 418–433 (2021).
36. Drago, J. Z., Modi, S. & Chandarlapaty, S. Unlocking the potential of antibody–drug conjugates for cancer therapy. *Nat. Rev. Clin. Oncol.* **18**, 327–344 (2021).
37. Hurvitz, S. A. Recent progress in antibody–drug conjugate therapy for cancer. *Nat. Cancer* **3**, 1412–1413 (2022).
38. Lopus, M. *et al.* Maytansine and Cellular Metabolites of Antibody-Maytansinoid Conjugates Strongly Suppress Microtubule Dynamics by Binding to Microtubules. *Mol. Cancer Ther.* **9**, 2689–2699 (2010).
39. Prota, A. E. *et al.* A new tubulin-binding site and pharmacophore for microtubule-destabilizing anticancer drugs. *Proc. Natl. Acad. Sci.* **111**, 13817–13821 (2014).
40. Mitsui, I. *et al.* A New Water-soluble Camptothecin Derivative, DX-8951f, Exhibits Potent Antitumor Activity against Human Tumors in vitro and in vivo. *Japanese J. Cancer Res.* **86**, 776–782 (1995).

41. Garrison, M. A. *et al.* A Phase I and pharmocokinetic study of exatecan mesylate administered as a protracted 21-day infusion in patients with advanced solid malignancies. *Clin. Cancer Res.* **9**, 2527–37 (2003).
42. Makawita, S. & Meric-Bernstam, F. Antibody-Drug Conjugates: Patient and Treatment Selection. *Am. Soc. Clin. Oncol. Educ. B.* 105–114 (2020) doi:10.1200/EDBK_280775.
43. Andre, F. *et al.* Mechanism of action and resistance to Trastuzumab Deruxtecan in patients with metastatic breast cancer: the DAISY trial. (2022) doi:10.21203/rs.3.rs-2083650/v1.
44. Pereira, B. *et al.* The somatic mutation profiles of 2,433 breast cancers refines their genomic and transcriptomic landscapes. *Nat. Commun.* **7**, (2016).
45. Chakravarty, D. *et al.* OncoKB: A Precision Oncology Knowledge Base. *JCO Precis. Oncol.* 1–16 (2017) doi:10.1200/PO.17.00011.
46. Mateo, J. *et al.* A framework to rank genomic alterations as targets for cancer precision medicine: the ESMO Scale for Clinical Actionability of molecular Targets (ESCAT). *Ann. Oncol.* 1895–1902 (2018) doi:10.1093/annonc/mdy263.
47. Andre, F. *et al.* Genomics to select treatment for patients with metastatic breast cancer. *Nature* **610**, 343–348 (2022).
48. Henry, N. L. *et al.* Biomarkers for Systemic Therapy in Metastatic Breast Cancer: ASCO Guideline Update. *J. Clin. Oncol.* **40**, 3205–3221 (2022).
49. Bidard, F.-C. *et al.* Elacestrant (oral selective estrogen receptor degrader) Versus Standard Endocrine Therapy for Estrogen Receptor–Positive, Human Epidermal Growth Factor Receptor 2–Negative Advanced Breast Cancer: Results From the Randomized Phase III EMERALD Trial. *J. Clin. Oncol.* **40**, 3246–3256 (2022).
50. FDA. FDA approves elacestrant for ER-positive, HER2-negative, ESR1-mutated advanced or metastatic breast cancer. *News release* https://www.fda.gov/drugs/resources-information-approved-drugs/ (2023).
51. Berger, A. C. *et al.* A Comprehensive Pan-Cancer Molecular Study of Gynecologic and Breast Cancers. *Cancer Cell* **33**, 690-705.e9 (2018).
52. Pugh, T. J. *et al.* AACR Project GENIE: 100,000 Cases and Beyond. *Cancer Discov.* **12**, 2044–2057 (2022).
53. Weinstein, J. N. *et al.* The Cancer Genome Atlas Pan-Cancer analysis project. *Nat. Genet.* **45**, 1113–1120 (2013).
54. Nguyen, B. *et al.* Genomic characterization of metastatic patterns from prospective clinical

sequencing of 25,000 patients. *Cell* **185**, 563-575.e11 (2022).

55. Fountain, J. W. *et al.* Physical mapping of the von Recklinghausen neurofibromatosis region on chromosome 17. *Am. J. Hum. Genet.* **44**, 58–67 (1989).
56. Ballester, R. *et al.* The NF1 locus encodes a protein functionally related to mammalian GAP and yeast IRA proteins. *Cell* **63**, 851–859 (1990).
57. Wallace, M. R. *et al.* Type 1 Neurofibromatosis Gene: Identification of a Large Transcript Disrupted in Three NF1 Patients. *Science (80-.).* **249**, 181–186 (1990).
58. Viskochil, D. *et al.* Deletions and a translocation interrupt a cloned gene at the neurofibromatosis type 1 locus. *Cell* **62**, 187–192 (1990).
59. Cawthon, R. M. *et al.* A major segment of the neurofibromatosis type 1 gene: cDNA sequence, genomic structure, and point mutations. *Cell* **62**, 193–201 (1990).
60. Martin, G. A. *et al.* The GAP-related domain of the neurofibromatosis type 1 gene product interacts with ras p21. *Cell* **63**, 843–849 (1990).
61. Marchuk, D. A. *et al.* cDNA cloning of the type 1 neurofibromatosis gene: Complete sequence of the NF1 gene product. *Genomics* **11**, 931–940 (1991).
62. Li, Y. *et al.* Genomic organization of the neurofibromatosis 1 gene (NF1). *Genomics* **25**, 9–18 (1995).
63. Anastasaki, C., Le, L. Q., Kesterson, R. A. & Gutmann, D. H. Updated nomenclature for human and mouse neurofibromatosis type 1 genes. *Neurol. Genet.* **3**, e169 (2017).
64. Gutmann, D. H. *et al.* Neurofibromatosis type 1. *Nat. Rev. Dis. Prim.* **3**, 1–18 (2017).
65. Gutmann, D. H. Neurofibromatosis Type 1. *Arch. Neurol.* **50**, 1185 (1993).
66. Bloomfield, G. *et al.* Neurofibromin controls macropinocytosis and phagocytosis in Dictyostelium. *Elife* **2015**, 1–25 (2015).
67. King, L. B. *et al.* Neurofibromin Loss of Function Drives Excessive Grooming in Drosophila. *G3 Genes|Genomes|Genetics* **6**, 1083–1093 (2016).
68. Bartelt-Kirbach, B. & Kaufmann, D. Insights into NF1 from Evolution. in *Neurofibromatosis Type 1* 253–268 (Springer Berlin Heidelberg, 2012). doi:10.1007/978-3-642-32864-0_17.
69. Assum, G. & Schmegner, C. NF1 Gene Evolution in Mammals. in *Neurofibromatoses* 103–112 (KARGER, 2008). doi:10.1159/000126548.
70. Philpott, C., Tovell, H., Frayling, I. M., Cooper, D. N. & Upadhyaya, M. The NF1 somatic mutational landscape in sporadic human cancers. *Hum. Genomics* **11**, 13 (2017).
71. Koster, R. *et al.* Pathogenic neurofibromatosis type 1 (NF1) RNA splicing resolved by

targeted RNAseq. *npj Genomic Med.* **6**, 95 (2021).

72. Lupton, C. J. *et al.* The cryo-EM structure of the human neurofibromin dimer reveals the molecular basis for neurofibromatosis type 1. *Nat. Struct. Mol. Biol.* **28**, 982–988 (2021).
73. Messiaen, L. M. & Wimmer, K. NF1 Mutational Spectrum. in *Neurofibromatoses* 63–77 (KARGER, 2008). doi:10.1159/000126545.
74. Gutmann, D. H., Wood, D. L. & Collins, F. S. Identification of the neurofibromatosis type 1 gene product. *Proc. Natl. Acad. Sci.* **88**, 9658–9662 (1991).
75. Buchberg, A. M., Cleveland, L. S., Jenkins, N. A. & Copeland, N. G. Sequence homology shared by neurofibromatosis type-1 gene and IRA-1 and IRA-2 negative regulators of the RAS cyclic AMP pathway. *Nature* **347**, 291–294 (1990).
76. Xu, G. *et al.* The neurofibromatosis type 1 gene encodes a protein related to GAP. *Cell* **62**, 599–608 (1990).
77. Basu, T. N. *et al.* Aberrant regulation of ras proteins in malignant tumour cells from type 1 neurofibromatosis patients. *Nature* **356**, 713–715 (1992).
78. Xu, G. *et al.* The catalytic domain of the neurofibromatosis type 1 gene product stimulates ras GTPase and complements ira mutants of S. cerevisiae. *Cell* **63**, 835–841 (1990).
79. Daston, M. M. *et al.* The protein product of the neurofibromatosis type 1 gene is expressed at highest abundance in neurons, Schwann cells, and oligodendrocytes. *Neuron* **8**, 415–428 (1992).
80. DeClue, J. E., Cohen, B. D. & Lowy, D. R. Identification and characterization of the neurofibromatosis type 1 protein product. *Proc. Natl. Acad. Sci.* **88**, 9914–9918 (1991).
81. Vandenbroucke, I., Vandesompele, J., De Paepe, A. & Messiaen, L. Quantification of NF1 transcripts reveals novel highly expressed splice variants. *FEBS Lett.* **522**, 71–76 (2002).
82. Mo, J., Moye, S. L., McKay, R. M. & Le, L. Q. Neurofibromin and suppression of tumorigenesis: beyond the GAP. *Oncogene* **41**, 1235–1251 (2022).
83. Vandenbroucke, I., Van Oostveldt, P., Coene, E., De Paepe, A. & Messiaen, L. Neurofibromin is actively transported to the nucleus. *FEBS Lett.* **560**, 98–102 (2004).
84. Peta, C., Tsirimonaki, E., Samouil, D., Georgiadou, K. & Mangoura, D. Nuclear Isoforms of Neurofibromin Are Required for Proper Spindle Organization and Chromosome Segregation. *Cells* **9**, (2020).
85. Gutmann, D. H., Geist, R. T., Rose, K. & Wright, D. E. Expression of two new protein isoforms of the neurofibromatosis type 1 gene product, neurofibromin, in muscle tissues. *Dev. Dyn.*

202, 302–311 (1995).

86. Dischinger, P. S. *et al.* NF1 deficiency correlates with estrogen receptor signaling and diminished survival in breast cancer. *npj Breast Cancer* **4**, 29 (2018).
87. Scheffzek, K. Structural analysis of the GAP-related domain from neurofibromin and its implications. *EMBO J.* **17**, 4313–4327 (1998).
88. D'angelo, I., Welti, S., Bonneau, F. & Scheffzek, K. A novel bipartite phospholipid-binding module in the neurofibromatosis type 1 protein. *EMBO Rep.* **7**, 174–179 (2006).
89. Naschberger, A., Baradaran, R., Rupp, B. & Carroni, M. The structure of neurofibromin isoform 2 reveals different functional states. *Nature* **599**, 315–319 (2021).
90. Carnes, R. M., Kesterson, R. A., Korf, B. R., Mobley, J. A. & Wallis, D. Affinity purification of NF1 protein–protein interactors identifies keratins and neurofibromin itself as binding partners. *Genes (Basel).* **10**, (2019).
91. Sherekar, M. *et al.* Biochemical and structural analyses reveal that the tumor suppressor neurofibromin (NF1) forms a high-affinity dimer. *J. Biol. Chem.* **295**, 1105–1119 (2020).
92. Wang, H.-F. *et al.* Valosin-containing protein and neurofibromin interact to regulate dendritic spine density. *J. Clin. Invest.* **121**, 4820–4837 (2011).
93. Li, C., Cheng, Y., Gutmann, D. A. & Mangoura, D. Differential localization of the neurofibromatosis 1 (NF1) gene product, neurofibromin, with the F-actin or microtubule cytoskeleton during differentiation of telencephalic neurons. *Dev. Brain Res.* **130**, 231–248 (2001).
94. Chaker-Margot, M. *et al.* Structural basis of activation of the tumor suppressor protein neurofibromin. *Mol. Cell* **82**, 1288-1296.e5 (2022).
95. Welti, S. *et al.* Structural and biochemical consequences of NF1 associated nontruncating mutations in the Sec14-PH module of neurofibromin. *Hum. Mutat.* **32**, 191–197 (2011).
96. Evans, D. G. *et al.* Birth incidence and prevalence of tumor-prone syndromes: Estimates from a UK family genetic register service. *Am. J. Med. Genet. Part A* **152A**, 327–332 (2010).
97. Uusitalo, E. *et al.* Incidence and Mortality of Neurofibromatosis: A Total Population Study in Finland. *J. Invest. Dermatol.* **135**, 904–906 (2015).
98. Ratner, N. & Miller, S. J. A RASopathy gene commonly mutated in cancer: The neurofibromatosis type 1 tumour suppressor. *Nat. Rev. Cancer* **15**, 290–301 (2015).
99. Pan-cancer analysis of whole genomes. *Nature* **578**, 82–93 (2020).
100. Mo, J., Moye, S. L., McKay, R. M. & Le, L. Q. Neurofibromin and suppression of

tumorigenesis: beyond the GAP. *Oncogene* **41**, 1235–1251 (2022).

101. Gasper, R., Meyer, S., Gotthardt, K., Sirajuddin, M. & Wittinghofer, A. It takes two to tango: regulation of G proteins by dimerization. *Nat. Rev. Mol. Cell Biol.* **10**, 423–429 (2009).
102. Vetter, I. R. & Wittinghofer, A. The Guanine Nucleotide-Binding Switch in Three Dimensions. *Science (80-.).* **294**, 1299–1304 (2001).
103. Bos, J. L., Rehmann, H. & Wittinghofer, A. GEFs and GAPs: Critical Elements in the Control of Small G Proteins. *Cell* **129**, 865–877 (2007).
104. Aoki, Y., Niihori, T., Inoue, S. & Matsubara, Y. Recent advances in RASopathies. *J. Hum. Genet.* **61**, 33–39 (2016).
105. Hebron, K. E., Hernandez, E. R. & Yohe, M. E. The RASopathies: from pathogenetics to therapeutics. *Dis. Model. Mech.* **15**, (2022).
106. Simanshu, D. K., Nissley, D. V. & McCormick, F. RAS Proteins and Their Regulators in Human Disease. *Cell* **170**, 17–33 (2017).
107. Rezaei Adariani, S. *et al.* A comprehensive analysis of RAS-effector interactions reveals interaction hotspots and new binding partners. *J. Biol. Chem.* **296**, 100626 (2021).
108. Hiatt, K. K., Ingram, D. A., Zhang, Y., Bollag, G. & Clapp, D. W. Neurofibromin GTPase-activating Protein-related Domains Restore Normal Growth in Nf1−/− Cells. *J. Biol. Chem.* **276**, 7240–7245 (2001).
109. Wellbrock, C., Karasarides, M. & Marais, R. The RAF proteins take centre stage. *Nat. Rev. Mol. Cell Biol.* **5**, 875–885 (2004).
110. Jessen, W. J. *et al.* MEK inhibition exhibits efficacy in human and mouse neurofibromatosis tumors. *J. Clin. Invest.* **123**, 340–347 (2013).
111. Chen, Z. *et al.* Cells of Origin in the Embryonic Nerve Roots for NF1-Associated Plexiform Neurofibroma. *Cancer Cell* **26**, 695–706 (2014).
112. Gross, A. M. *et al.* Selumetinib in Children with Inoperable Plexiform Neurofibromas. *N. Engl. J. Med.* **382**, 1430–1442 (2020).
113. Casey, D. *et al.* FDA Approval Summary: Selumetinib for Plexiform Neurofibroma. *Clin. Cancer Res.* **27**, 4142–4146 (2021).
114. Nissan, M. H. *et al.* Loss of NF1 in cutaneous melanoma is associated with RAS activation and MEK dependence. *Cancer Res.* **74**, 2340–2350 (2014).
115. Rajkumar, S. *et al.* Melanomas with concurrent BRAF non-p.V600 and NF1 loss-of-function mutations are targetable by BRAF/MEK inhibitor combination therapy. *Cell Rep.* **39**, 110634

(2022).

116. Kiuru, M. & Busam, K. J. The NF1 gene in tumor syndromes and melanoma. *Lab. Investig.* **97**, 146–157 (2017).
117. Whittaker, S. R. *et al.* A Genome-Scale RNA Interference Screen Implicates NF1 Loss in Resistance to RAF Inhibition. *Cancer Discov.* **3**, 350–362 (2013).
118. Redig, A. J. *et al.* Clinical and Molecular Characteristics of NF1 -Mutant Lung Cancer. *Clin. Cancer Res.* **22**, 3148–3156 (2016).
119. Tlemsani, C. *et al.* NF1 mutations identify molecular and clinical subtypes of lung adenocarcinomas. *Cancer Med.* **8**, 4330–4337 (2019).
120. de Bruin, E. C. *et al.* Reduced NF1 Expression Confers Resistance to EGFR Inhibition in Lung Cancer. *Cancer Discov.* **4**, 606–619 (2014).
121. Razavi, P. *et al.* The Genomic Landscape of Endocrine-Resistant Advanced Breast Cancers. *Cancer Cell* **34**, 427-438.e6 (2018).
122. Dischinger, P. S. *et al.* NF1 deficiency correlates with estrogen receptor signaling and diminished survival in breast cancer. *NPJ Breast Cancer* (2018) doi:10.1038/s41523-018-0080-8.
123. Zheng, Z.-Y. *et al.* Neurofibromin Is an Estrogen Receptor-α Transcriptional Co-repressor in Breast Cancer. *Cancer Cell* **37**, 387-402.e7 (2020).
124. Pearson, A. *et al.* Inactivating NF1 mutations are enriched in advanced breast cancer and contribute to endocrine therapy resistance. *Clin. Cancer Res.* clincanres.4044.2018 (2019) doi:10.1158/1078-0432.ccr-18-4044.
125. Turner, N. C. *et al.* Overall Survival with Palbociclib and Fulvestrant in Advanced Breast Cancer. *N. Engl. J. Med.* **379**, 1926–1936 (2018).
126. Sokol, E. S. *et al.* Loss of function of NF1 is a mechanism of acquired resistance to endocrine therapy in lobular breast cancer. *Ann. Oncol.* **30**, 115–123 (2019).
127. Smith, A. E. *et al.* HER2 + breast cancers evade anti-HER2 therapy via a switch in driver pathway. *Nat. Commun.* **12**, 6667 (2021).
128. Johannessen, C. M. *et al.* The NF1 tumor suppressor critically regulates TSC2 and mTOR. *Proc. Natl. Acad. Sci.* **102**, 8573–8578 (2005).
129. Li, X. *et al.* Clustered, Regularly Interspaced Short Palindromic Repeats (CRISPR)/Cas9-coupled Affinity Purification/Mass Spectrometry Analysis Revealed a Novel Role of Neurofibromin in mTOR Signaling. *Mol. Cell. Proteomics* **16**, 594–607 (2017).

130. Johannessen, C. M. *et al.* The NF1 tumor suppressor critically regulates TSC2 and mTOR. *Proc. Natl. Acad. Sci.* **102**, 8573–8578 (2005).
131. Dasgupta, B., Yi, Y., Chen, D. Y., Weber, J. D. & Gutmann, D. H. Proteomic Analysis Reveals Hyperactivation of the Mammalian Target of Rapamycin Pathway in Neurofibromatosis 1–Associated Human and Mouse Brain Tumors. *Cancer Res.* **65**, 2755–2760 (2005).
132. Ghadimi, M. P. *et al.* Targeting the PI3K/mTOR Axis, Alone and in Combination with Autophagy Blockade, for the Treatment of Malignant Peripheral Nerve Sheath Tumors. *Mol. Cancer Ther.* **11**, 1758–1769 (2012).
133. Johansson, G. *et al.* Effective in vivo targeting of the mammalian target of rapamycin pathway in malignant peripheral nerve sheath tumors. *Mol. Cancer Ther.* **7**, 1237–1245 (2008).
134. Weiss, B. *et al.* Sirolimus for progressive neurofibromatosis type 1-associated plexiform neurofibromas: a Neurofibromatosis Clinical Trials Consortium phase II study. *Neuro. Oncol.* **17**, 596–603 (2015).
135. Turke, A. B. *et al.* MEK Inhibition Leads to PI3K/AKT Activation by Relieving a Negative Feedback on ERBB Receptors. *Cancer Res.* **72**, 3228–3237 (2012).
136. van der Noord, V. E. *et al.* An increased cell cycle gene network determines MEK and Akt inhibitor double resistance in triple-negative breast cancer. *Sci. Rep.* **9**, 13308 (2019).
137. Stuhlmiller, T. J. *et al.* Inhibition of Lapatinib-Induced Kinome Reprogramming in ERBB2-Positive Breast Cancer by Targeting BET Family Bromodomains. *Cell Rep.* **11**, 390–404 (2015).
138. Rozengurt, E., Soares, H. P. & Sinnet-Smith, J. Suppression of Feedback Loops Mediated by PI3K/mTOR Induces Multiple Overactivation of Compensatory Pathways: An Unintended Consequence Leading to Drug Resistance. *Mol. Cancer Ther.* **13**, 2477–2488 (2014).
139. Sathe, A. *et al.* Parallel PI3K, AKT and mTOR inhibition is required to control feedback loops that limit tumor therapy. *PLoS One* **13**, e0190854 (2018).
140. Haas, L. *et al.* Acquired resistance to anti-MAPK targeted therapy confers an immune-evasive tumor microenvironment and cross-resistance to immunotherapy in melanoma. *Nat. Cancer* **2**, 693–708 (2021).
141. Anastasaki, C., Orozco, P. & Gutmann, D. H. RAS and beyond: the many faces of the neurofibromatosis type 1 protein. *DMM Dis. Model. Mech.* **15**, (2022).
142. Stowe, I. B. *et al.* A shared molecular mechanism underlies the human rasopathies Legius

syndrome and Neurofibromatosis-1. *Genes Dev.* **26**, 1421–1426 (2012).

143. Lim, J. *et al.* The Cysteine-Rich Sprouty Translocation Domain Targets Mitogen-Activated Protein Kinase Inhibitory Proteins to Phosphatidylinositol 4,5-Bisphosphate in Plasma Membranes. *Mol. Cell. Biol.* **22**, 7953–7966 (2002).
144. Boyanapalli, M. *et al.* Neurofibromin binds to caveolin-1 and regulates ras, FAK, and Akt. *Biochem. Biophys. Res. Commun.* **340**, 1200–1208 (2006).
145. Yang, K. *et al.* Knockdown of MSI2 inhibits metastasis by interacting with caveolin-1 and inhibiting its ubiquitylation in human NF1-MPNST cells. *Cell Death Dis.* **11**, 489 (2020).
146. Luo, G., Kim, J. & Song, K. The C-terminal domains of human neurofibromin and its budding yeast homologs Ira1 and Ira2 regulate the metaphase to anaphase transition. *Cell Cycle* **13**, 2780–2789 (2014).
147. Beausoleil, S. A. *et al.* Large-scale characterization of HeLa cell nuclear phosphoproteins. *Proc. Natl. Acad. Sci.* **101**, 12130–12135 (2004).
148. Nousiainen, M., Silljé, H. H. W., Sauer, G., Nigg, E. A. & Körner, R. Phosphoproteome analysis of the human mitotic spindle. *Proc. Natl. Acad. Sci.* **103**, 5391–5396 (2006).
149. Koliou, X., Fedonidis, C., Kalpachidou, T. & Mangoura, D. Nuclear import mechanism of neurofibromin for localization on the spindle and function in chromosome congression. *J. Neurochem.* **136**, 78–91 (2016).
150. Koliou, X., Fedonidis, C., Kalpachidou, T. & Mangoura, D. Nuclear import mechanism of neurofibromin for localization on the spindle and function in chromosome congression. *J. Neurochem.* **136**, 78–91 (2016).
151. Rodriguez, F. J. N for nucleus in neurofibromin: New role for an old tumor suppressor? *J. Neurochem.* **136**, 11–12 (2016).
152. Hsueh, Y.-P., Roberts, A. M., Volta, M., Sheng, M. & Roberts, R. G. Bipartite Interaction between Neurofibromatosis Type I Protein (Neurofibromin) and Syndecan Transmembrane Heparan Sulfate Proteoglycans. *J. Neurosci.* **21**, 3764–3770 (2001).
153. Lin, Y.-L., Lei, Y.-T., Hong, C.-J. & Hsueh, Y.-P. Syndecan-2 induces filopodia and dendritic spine formation via the neurofibromin–PKA–Ena/VASP pathway. *J. Cell Biol.* **177**, 829–841 (2007).
154. Volta, M., Calza, S., Roberts, A. M. & Roberts, R. G. Characterisation of the interaction between syndecan-2, neurofibromin and CASK: Dependence of interaction on syndecan dimerization. *Biochem. Biophys. Res. Commun.* **391**, 1216–1221 (2010).

155. Afratis, N. A. *et al.* Syndecans – key regulators of cell signaling and biological functions. *FEBS J.* **284**, 27–41 (2017).
156. Kim, J.-M., Lee, K., Kim, M. Y., Shin, H.-I. & Jeong, D. Suppressive effect of syndecan ectodomains and N-desulfated heparins on osteoclastogenesis via direct binding to macrophage-colony stimulating factor. *Cell Death Dis.* **9**, 1119 (2018).
157. Meyer, H., Bug, M. & Bremer, S. Emerging functions of the VCP/p97 AAA-ATPase in the ubiquitin system. *Nat. Cell Biol.* **14**, 117–123 (2012).
158. Yi, P. *et al.* Sorafenib-Mediated Targeting of the AAA+ ATPase p97/VCP Leads to Disruption of the Secretory Pathway, Endoplasmic Reticulum Stress, and Hepatocellular Cancer Cell Death. *Mol. Cancer Ther.* **11**, 2610–2620 (2012).
159. Hänzelmann, P. & Schindelin, H. Structural Basis of ATP Hydrolysis and Intersubunit Signaling in the AAA+ ATPase p97. *Structure* **24**, 127–139 (2016).
160. Rizzelli, F., Malabarba, M. G., Sigismund, S. & Mapelli, M. The crosstalk between microtubules, actin and membranes shapes cell division. *Open Biol.* **10**, (2020).
161. Gibieža, P. & Petrikaitė, V. The regulation of actin dynamics during cell division and malignancy. *Am. J. Cancer Res.* **11**, 4050–4069 (2021).
162. Gudimchuk, N. B. *et al.* Mechanisms of microtubule dynamics and force generation examined with computational modeling and electron cryotomography. *Nat. Commun.* **11**, 1–15 (2020).
163. Bollag, G., McCormick, F. & Clark, R. Characterization of full-length neurofibromin: Tubulin inhibits Ras GAP activity. *EMBO J.* **12**, 1923–1927 (1993).
164. Gregory, P. E. *et al.* Neurofibromatosis type 1 gene product (neurofibromin) associates with microtubules. *Somat. Cell Mol. Genet.* **19**, 265–274 (1993).
165. Ozawa, T. *et al.* The Neurofibromatosis Type 1 Gene Product Neurofibromin Enhances Cell Motility by Regulating Actin Filament Dynamics via the Rho-ROCK-LIMK2-Cofilin Pathway. *J. Biol. Chem.* **280**, 39524–39533 (2005).
166. Mangoura, D. *et al.* Phosphorylation of neurofibromin by PKC is a possible molecular switch in EGF receptor signaling in neural cells. *Oncogene* **25**, 735–745 (2006).
167. Gudimchuk, N. B. & McIntosh, J. R. Regulation of microtubule dynamics, mechanics and function through the growing tip. *Nat. Rev. Mol. Cell Biol.* **22**, 777–795 (2021).
168. Dominguez, R. & Holmes, K. C. Actin Structure and Function. *Annu. Rev. Biophys.* **40**, 169–186 (2011).

169. Vallée, B. *et al.* Nf1 RasGAP Inhibition of LIMK2 Mediates a New Cross-Talk between Ras and Rho Pathways. *PLoS One* **7**, (2012).
170. Starinsky-Elbaz, S., Faigenbloom, L., Friedman, E., Stein, R. & Kloog, Y. The pre-GAP-related domain of neurofibromin regulates cell migration through the LIM kinase/cofilin pathway. *Mol. Cell. Neurosci.* **42**, 278–287 (2009).
171. Pollard, T. D. & Borisy, G. G. Cellular Motility Driven by Assembly and Disassembly of Actin Filaments. *Cell* **112**, 453–465 (2003).
172. Scott, R. W. & Olson, M. F. LIM kinases: function, regulation and association with human disease. *J. Mol. Med.* **85**, 555–568 (2007).
173. Kweh, F. *et al.* Neurofibromin physically interacts with the N-terminal domain of focal adhesion kinase. *Mol. Carcinog.* **48**, 1005–1017 (2009).
174. Errico, A. *et al.* Neurofibromin Deficiency and Extracellular Matrix Cooperate to Increase Transforming Potential through FAK-Dependent Signaling. *Cancers (Basel).* **13**, 2329 (2021).
175. Sulzmaier, F. J., Jean, C. & Schlaepfer, D. D. FAK in cancer: mechanistic findings and clinical applications. *Nat. Rev. Cancer* **14**, 598–610 (2014).
176. Berger, A. C. *et al.* A Comprehensive Pan-Cancer Molecular Study of Gynecologic and Breast Cancers. *Cancer Cell* **33**, 690-705.e9 (2018).
177. Xu, H. & Gutmann, D. H. Mutations in the GAP-related domain impair the ability of neurofibromin to associate with microtubules. *Brain Res.* **759**, 149–152 (1997).
178. Arpağ, G., Lawrence, E. J., Farmer, V. J., Hall, S. L. & Zanic, M. Collective effects of XMAP215, EB1, CLASP2, and MCAK lead to robust microtubule treadmilling. *Proc. Natl. Acad. Sci.* **117**, 12847–12855 (2020).
179. Michaels, T. C., Feng, S., Liang, H. & Mahadevan, L. Mechanics and kinetics of dynamic instability. *Elife* **9**, (2020).
180. Vale, R. D., Coppin, C. M., Malik, F., Kull, F. J. & Milligan, R. A. Tubulin GTP hydrolysis influences the structure, mechanical properties, and kinesin-driven transport of microtubules. *J. Biol. Chem.* **269**, 23769–75 (1994).
181. Hyman, A. A., Salser, S., Drechsel, D. N., Unwin, N. & Mitchison, T. J. Role of GTP hydrolysis in microtubule dynamics: Information from a slowly hydrolyzable analogue, GMPCPP. *Mol. Biol. Cell* **3**, 1155–1167 (1992).
182. Piedra, F. A. *et al.* GDP-To-GTP exchange on the microtubule end can contribute to the frequency of catastrophe. *Mol. Biol. Cell* **27**, 3515–3525 (2016).

183. Roostalu, J. *et al.* The speed of GTP hydrolysis determines GTP cap size and controls microtubule stability. *Elife* **9**, 1–22 (2020).
184. Akhmanova, A. & Steinmetz, M. O. Control of microtubule organization and dynamics: two ends in the limelight. *Nat. Rev. Mol. Cell Biol.* **16**, 711–726 (2015).
185. Jiang, K. *et al.* TIP150 interacts with and targets MC AK at the microtubule plus ends. *EMBO Rep.* **10**, 857–865 (2009).
186. Manka, S. W. & Moores, C. A. The role of tubulin–tubulin lattice contacts in the mechanism of microtubule dynamic instability. *Nat. Struct. Mol. Biol.* **25**, 607–615 (2018).
187. Janke, C. & Magiera, M. M. The tubulin code and its role in controlling microtubule properties and functions. *Nat. Rev. Mol. Cell Biol.* **21**, 307–326 (2020).
188. Roll-Mecak, A. The Tubulin Code in Microtubule Dynamics and Information Encoding. *Dev. Cell* **54**, 7–20 (2020).
189. Nogales, E., Wolf, S. G. & Downing, K. H. Structure of the αβ tubulin dimer by electron crystallography. *Nature* **391**, 199–203 (1998).
190. Walker, R. A. *et al.* Dynamic instability of individual microtubules analyzed by video light microscopy: rate constants and transition frequencies. *J. Cell Biol.* **107**, 1437–1448 (1988).
191. Howard, J. & Hyman, A. A. Dynamics and mechanics of the microtubule plus end. *Nature* **422**, 753–758 (2003).
192. Desai, A. & Mitchison, T. J. MICROTUBULE POLYMERIZATION DYNAMICS. *Annu. Rev. Cell Dev. Biol.* **13**, 83–117 (1997).
193. Dimitrov, A. *et al.* Detection of GTP-tubulin conformation in vivo reveals a role for GTP remnants in microtubule rescues. *Science (80-.).* **322**, 1353–1356 (2008).
194. Cassimeris, L. Microtubule Assembly: Lattice GTP to the Rescue. *Curr. Biol.* **19**, R174–R176 (2009).
195. Gardner, M. K. *et al.* Rapid Microtubule Self-Assembly Kinetics. *Cell* **146**, 582–592 (2011).
196. Tropini, C., Roth, E. A., Zanic, M., Gardner, M. K. & Howard, J. Islands containing slowly hydrolyzable GTP analogs promote microtubule rescues. *PLoS One* **7**, (2012).
197. Bollinger, J. A., Imam, Z. I., Stevens, M. J. & Bachand, G. D. Tubulin islands containing slowly hydrolyzable GTP analogs regulate the mechanism and kinetics of microtubule depolymerization. *Sci. Rep.* **10**, 1–11 (2020).
198. Nogales, E., Downing, K. H., Amos, L. A. & L**?**we, J. Tubulin and FtsZ form a distinct family of GTPases. *Nat. Struct. Biol.* **5**, 451–458 (1998).

199. Murphy, D. B. & Borisy, G. G. Association of high-molecular-weight proteins with microtubules and their role in microtubule assembly in vitro. *Proc. Natl. Acad. Sci.* **72**, 2696–2700 (1975).

200. Castle, B. T., McKibben, K. M., Rhoades, E. & Odde, D. J. Tau Avoids the GTP Cap at Growing Microtubule Plus-Ends. *iScience* **23**, 101782 (2020).

201. Cleary, J. M. & Hancock, W. O. Molecular mechanisms underlying microtubule growth dynamics. *Curr. Biol.* **31**, R560–R573 (2021).

202. Nakata, T., Niwa, S., Okada, Y., Perez, F. & Hirokawa, N. Preferential binding of a kinesin-1 motor to GTP-tubulin-rich microtubules underlies polarized vesicle transport. *J. Cell Biol.* **194**, 245–255 (2011).

203. Kwok, B. H. & Paydar, M. Evidence for Conformational Change-Induced Hydrolysis of β-Tubulin-GTP. *SSRN Electron. J.* (2020) doi:10.2139/ssrn.3687033.

204. Prota, A. E. *et al.* Molecular Mechanism of Action of Microtubule-Stabilizing Anticancer Agents. *Science (80-.).* **339**, 587–590 (2013).

205. Steinmetz, M. O. & Prota, A. E. Microtubule-Targeting Agents: Strategies To Hijack the Cytoskeleton. *Trends Cell Biol.* **28**, 776–792 (2018).

206. Brouhard, G. J. & Rice, L. M. The contribution of αβ-tubulin curvature to microtubule dynamics. *J. Cell Biol.* **207**, 323–334 (2014).

207. Hernandez, P. & Tirnauer, J. S. Tumor suppressor interactions with microtubules: keeping cell polarity and cell division on track. *Dis. Model. Mech.* **3**, 304–315 (2010).

208. Arun, V., Worrell, L., Wiley, J. C., Kaplan, D. R. & Guha, A. Neurofibromin interacts with the cytoplasmic Dynein Heavy Chain 1 in melanosomes of human melanocytes. *FEBS Lett.* **587**, 1466–1473 (2013).

209. Hakimi, M.-A., Speicher, D. W. & Shiekhattar, R. The Motor Protein Kinesin-1 Links Neurofibromin and Merlin in a Common Cellular Pathway of Neurofibromatosis. *J. Biol. Chem.* **277**, 36909–36912 (2002).

210. Miki, H. & Hirokawa, N. Kinesin Superfamily Classification. in *Encyclopedia of Biophysics* 1191–1200 (Springer Berlin Heidelberg, 2013). doi:10.1007/978-3-642-16712-6_762.

211. Bringmann, H. *et al.* A Kinesin-like Motor Inhibits Microtubule Dynamic Instability. *Science (80-.).* **303**, 1519–1522 (2004).

212. Sharp, D. J., Rogers, G. C. & Scholey, J. M. Microtubule motors in mitosis. *Nature* **407**, 41–47 (2000).

213. Daire, V. *et al.* Kinesin-1 regulates microtubule dynamics via a c-Jun N-terminal kinase-dependent mechanism. *J. Biol. Chem.* **284**, 31992–32001 (2009).
214. Zheng, R. *et al.* KIF2C regulates synaptic plasticity and cognition in mice through dynamic microtubule depolymerization. *Elife* **11**, (2022).
215. Niwa, S. *et al.* KIF19A Is a Microtubule-Depolymerizing Kinesin for Ciliary Length Control. *Dev. Cell* **23**, 1167–1175 (2012).
216. Hunter, A. W. *et al.* The kinesin-related protein MCAK is a microtubule depolymerase that forms an ATP-hydrolyzing complex at microtubule ends. *Mol. Cell* **11**, 445–457 (2003).
217. Wagenbach, M., Domnitz, S., Wordeman, L. & Cooper, J. A kinesin-13 mutant catalytically depolymerizes microtubules in ADP. *J. Cell Biol.* **183**, 617–623 (2008).
218. Moore, A. T. *et al.* MCAK associates with the tips of polymerizing microtubules. *J. Cell Biol.* **169**, 391–397 (2005).
219. Walczak, C. E., Mitchison, T. J. & Desai, A. XKCM1: A Xenopus Kinesin-Related Protein That Regulates Microtubule Dynamics during Mitotic Spindle Assembly. *Cell* **84**, 37–47 (1996).
220. Du, Y., English, C. A. & Ohi, R. The Kinesin-8 Kif18A Dampens Microtubule Plus-End Dynamics. *Curr. Biol.* **20**, 374–380 (2010).
221. Su, X. *et al.* Mechanisms Underlying the Dual-Mode Regulation of Microtubule Dynamics by Kip3/Kinesin-8. *Mol. Cell* **43**, 751–763 (2011).
222. Blangy, A. *et al.* Phosphorylation by p34cdc2 regulates spindle association of human Eg5, a kinesin-related motor essential for bipolar spindle formation in vivo. *Cell* **83**, 1159–1169 (1995).
223. Walczak, C. E., Vernos, I., Mitchison, T. J., Karsenti, E. & Heald, R. A model for the proposed roles of different microtubule-based motor proteins in establishing spindle bipolarity. *Curr. Biol.* **8**, 903–913 (1998).
224. Suzuki, A. *et al.* A Kinesin-5, Cin8, Recruits Protein Phosphatase 1 to Kinetochores and Regulates Chromosome Segregation. *Curr. Biol.* **28**, 2697-2704.e3 (2018).
225. Mann, B. J. & Wadsworth, P. Kinesin-5 Regulation and Function in Mitosis. *Trends Cell Biol.* **29**, 66–79 (2019).
226. Tanenbaum, M. E. *et al.* Kif15 Cooperates with Eg5 to Promote Bipolar Spindle Assembly. *Curr. Biol.* **19**, 1703–1711 (2009).
227. Drechsler, H. & McAinsh, A. D. Kinesin-12 motors cooperate to suppress microtubule catastrophes and drive the formation of parallel microtubule bundles. *Proc. Natl. Acad. Sci.*

113, (2016).

228. Gomes, A. M. *et al.* Micronuclei from misaligned chromosomes that satisfy the spindle assembly checkpoint in cancer cells. *Curr. Biol.* **32**, 4240-4254.e5 (2022).
229. Marquis, C. *et al.* Chromosomally unstable tumor cells specifically require KIF18A for proliferation. *Nat. Commun.* **12**, (2021).
230. Stumpff, J., von Dassow, G., Wagenbach, M., Asbury, C. & Wordeman, L. The Kinesin-8 Motor Kif18A Suppresses Kinetochore Movements to Control Mitotic Chromosome Alignment. *Dev. Cell* **14**, 252–262 (2008).
231. Stout, J. R. *et al.* Kif18B interacts with EB1 and controls astral microtubule length during mitosis. *Mol. Biol. Cell* **22**, 3070–3080 (2011).
232. Zhou, J. *et al.* KIF11 functions as an oncogene and is associated with poor outcomes from breast cancer. *Cancer Res. Treat.* **51**, 1207–1221 (2019).
233. Zhou, Y. *et al.* KIF11 is upregulated in colorectal cancer and silencing of it impairs tumor growth and sensitizes colorectal cancer cells to oxaliplatin via p53/GSK3β signaling. *J. Cancer* **12**, 3741–3753 (2021).
234. Venere, M. *et al.* The mitotic kinesin KIF11 is a driver of invasion, proliferation, and self-renewal in glioblastoma. *Sci. Transl. Med.* **7**, (2015).
235. Niwa, S. *et al.* Structural basis for CRMP2-induced axonal microtubule formation. *Sci. Rep.* **7**, 1–17 (2017).
236. Patrakitkomjorn, S. *et al.* Neurofibromatosis type 1 (NF1) tumor suppressor, neurofibromin, regulates the neuronal differentiation of PC12 cells via its associating protein, CRMP-2. *J. Biol. Chem.* **283**, 9399–9413 (2008).
237. Zheng, Y. *et al.* Tuning microtubule dynamics to enhance cancer therapy by modulating FER-mediated CRMP2 phosphorylation. *Nat. Commun.* **9**, 1–12 (2018).
238. Fukata, Y. *et al.* CRMP-2 binds to tubulin heterodimers to promote microtubule assembly. *Nat. Cell Biol.* **4**, 583–591 (2002).
239. Lin, P. C., Chan, P. M., Hall, C. & Manser, E. Collapsin response mediator proteins (CRMPs) are a new class of microtubule-associated protein (MAP) that selectively interacts with assembled microtubules via a taxol-sensitive binding interaction. *J. Biol. Chem.* **286**, 41466–41478 (2011).
240. Brouhard, G. J. & Rice, L. M. Microtubule dynamics: An interplay of biochemistry and mechanics. *Nat. Rev. Mol. Cell Biol.* **19**, 451–463 (2018).

241. Eli, S., Castagna, R., Mapelli, M. & Parisini, E. Recent Approaches to the Identification of Novel Microtubule-Targeting Agents. *Front. Mol. Biosci.* **9**, (2022).
242. Yoshimura, T. *et al.* GSK-3β regulates phosphorylation of CRMP-2 and neuronal polarity. *Cell* **120**, 137–149 (2005).
243. Grant, N. J. *et al.* Phosphorylation of a splice variant of collapsin response mediator protein 2 in the nucleus of tumour cells links cyclin dependent kinase-5 to oncogenesis. *BMC Cancer* **15**, 885 (2015).
244. TAN, F., THIELE, C. J. & LI, Z. Collapsin response mediator proteins: Potential diagnostic and prognostic biomarkers in cancers (Review). *Oncol. Lett.* **7**, 1333–1340 (2014).
245. Moutal, A. *et al.* CRMP2 Phosphorylation Drives Glioblastoma Cell Proliferation. *Mol. Neurobiol.* **55**, 4403–4416 (2018).
246. Moutal, A. *et al.* CRMP2–Neurofibromin Interface Drives NF1-related Pain. *Neuroscience* **381**, 79–90 (2018).
247. Moutal, A. *et al.* CRISPR/Cas9 editing of Nf1 gene identifies CRMP2 as a therapeutic target in neurofibromatosis type 1-related pain that is reversed by (S)-Lacosamide. *Pain* **158**, 2301–2319 (2017).
248. Vogelstein, B. *et al.* Cancer genome landscapes. *Science (80-.).* **340**, 1546–1558 (2013).
249. Melloni, G. E. M. *et al.* A knowledge-based framework for the discovery of cancer-predisposing variants using large-scale sequencing breast cancer data. *Breast Cancer Res.* **19**, 1–14 (2017).
250. Guzmán, C., Bagga, M., Kaur, A., Westermarck, J. & Abankwa, D. ColonyArea: An ImageJ plugin to automatically quantify colony formation in clonogenic assays. *PLoS One* **9**, 14–17 (2014).
251. Casadevall, D. *et al.* mTOR Inhibition and T-DM1 in HER2-Positive Breast Cancer. *Mol. Cancer Res.* **20**, 1108–1121 (2022).
252. Molina, D. M. *et al.* Monitoring drug target engagement in cells and tissues using the cellular thermal shift assay. *Science (80-.).* **341**, 84–87 (2013).
253. Jafari, R. *et al.* The cellular thermal shift assay for evaluating drug target interactions in cells. *Nat. Protoc.* **9**, 2100–2122 (2014).
254. Langebäck, A. *et al.* CETSA-based target engagement of taxanes as biomarkers for efficacy and resistance. *Sci. Rep.* **9**, 1–17 (2019).
255. Lanman, R. B. *et al.* Analytical and Clinical Validation of a Digital Sequencing Panel for

Quantitative, Highly Accurate Evaluation of Cell-Free Circulating Tumor DNA. *PLoS One* **10**, e0140712 (2015).

256. Vitale, I., Galluzzi, L., Castedo, M. & Kroemer, G. Mitotic catastrophe: a mechanism for avoiding genomic instability. **12**, 1–8 (2011).
257. Chen, E. Y. *et al.* Enrichr: interactive and collaborative HTML5 gene list enrichment analysis tool. *BMC Bioinformatics* **14**, 128 (2013).
258. Sakaue-Sawano, A. *et al.* Genetically Encoded Tools for Optical Dissection of the Mammalian Cell Cycle. *Mol. Cell* **68**, 626-640.e5 (2017).
259. Roninson, I. B., Broude, E. V. & Chang, B.-D. If not apoptosis, then what? Treatment-induced senescence and mitotic catastrophe in tumor cells. *Drug Resist. Updat.* **4**, 303–313 (2001).
260. Mercadante, D. L., Crowley, E. A. & Manning, A. L. Live cell imaging to assess the dynamics of metaphase timing and cell fate following mitotic spindle perturbations. *J. Vis. Exp.* **2019**, 1–9 (2019).
261. Ganem, N. J., Godinho, S. A. & Pellman, D. A mechanism linking extra centrosomes to chromosomal instability. *Nature* **460**, 278–282 (2009).
262. Ogden, A., Rida, P. C. G. & Aneja, R. Let's huddle to prevent a muddle: Centrosome declustering as an attractive anticancer strategy. *Cell Death Differ.* **19**, 1255–1267 (2012).
263. Chavali, P. L. *et al.* A CEP215–HSET complex links centrosomes with spindle poles and drives centrosome clustering in cancer. *Nat. Commun.* **7**, 11005 (2016).
264. Quintyne, N. J., Reing, J. E., Hoffelder, D. R., Gollin, S. M. & Saunders, W. S. Spindle multipolarity is prevented by centrosomal clustering. *Science (80-.).* **307**, 127–129 (2005).
265. Cosenza, M. R. *et al.* Asymmetric Centriole Numbers at Spindle Poles Cause Chromosome Missegregation in Cancer. *Cell Rep.* **20**, 1906–1920 (2017).
266. Vassilev, L. T. *et al.* Selective small-molecule inhibitor reveals critical mitotic functions of human CDK1. *Proc. Natl. Acad. Sci.* **103**, 10660–10665 (2006).
267. Hanashiro, K., Kanai, M., Geng, Y., Sicinski, P. & Fukasawa, K. Roles of cyclins A and E in induction of centrosome amplification in p53-compromised cells. *Oncogene* **27**, 5288–5302 (2008).
268. Steere, N. *et al.* Centrosome amplification in CHO and DT40 cells by inactivation of cyclin-dependent kinases. *Cytoskeleton* **68**, 446–458 (2011).
269. Gavilan, M. P. *et al.* The dual role of the centrosome in organizing the microtubule network in interphase. *EMBO Rep.* **19**, (2018).

270. Jackson, J. R., Patrick, D. R., Dar, M. M. & Huang, P. S. Targeted anti-mitotic therapies: can we improve on tubulin agents? *Nat. Rev. Cancer* **7**, 107–117 (2007).
271. Huang, H.-C., Shi, J., Orth, J. D. & Mitchison, T. J. Evidence that Mitotic Exit Is a Better Cancer Therapeutic Target Than Spindle Assembly. *Cancer Cell* **16**, 347–358 (2009).
272. Serpico, A. F., Visconti, R. & Grieco, D. Exploiting immune-dependent effects of microtubule-targeting agents to improve efficacy and tolerability of cancer treatment. *Cell Death Dis.* **11**, 361 (2020).
273. Watanabe, Y. *et al.* Autophagy controls centrosome number by degrading Cep63. *Nat. Commun.* **7**, 13508 (2016).
274. Holdgaard, S. G. *et al.* Selective autophagy maintains centrosome integrity and accurate mitosis by turnover of centriolar satellites. *Nat. Commun.* **10**, 1–19 (2019).
275. Silkworth, W. T., Nardi, I. K., Scholl, L. M. & Cimini, D. Multipolar spindle pole coalescence is a major source of kinetochore mis-attachment and chromosome mis-segregation in cancer cells. *PLoS One* **4**, (2009).
276. Silkworth, W. T. & Cimini, D. Transient defects of mitotic spindle geometry and chromosome segregation errors. *Cell Div.* **7**, 1–8 (2012).
277. Godinho, S. A. & Pellman, D. Causes and consequences of centrosome abnormalities in cancer. *Philos. Trans. R. Soc. B Biol. Sci.* **369**, (2014).
278. Pihan, G. A. Centrosome Dysfunction Contributes to Chromosome Instability, Chromoanagenesis, and Genome Reprograming in Cancer. *Front. Oncol.* **3**, (2013).
279. Klaasen, S. J. *et al.* Nuclear chromosome locations dictate segregation error frequencies. *Nature* **607**, 604–609 (2022).
280. Franco, S. *et al.* H2AX Prevents DNA Breaks from Progressing to Chromosome Breaks and Translocations. *Mol. Cell* **21**, 201–214 (2006).
281. Gulluni, F. *et al.* Mitotic Spindle Assembly and Genomic Stability in Breast Cancer Require PI3K-C2α Scaffolding Function. *Cancer Cell* **32**, 444-459.e7 (2017).
282. Musacchio, A. & Salmon, E. D. The spindle-assembly checkpoint in space and time. *Nat. Rev. Mol. Cell Biol.* **8**, 379–393 (2007).
283. Meraldi, P., Draviam, V. M. & Sorger, P. K. Timing and checkpoints in the regulation of mitotic progression. *Dev. Cell* **7**, 45–60 (2004).
284. Vogel, C., Kienitz, A., Hofmann, I., Müller, R. & Bastians, H. Crosstalk of the mitotic spindle assembly checkpoint with p53 to prevent polyploidy. *Oncogene* **23**, 6845–6853 (2004).

285. Spurr, L. F. *et al.* Quantification of aneuploidy in targeted sequencing data using ASCETS. *Bioinformatics* **37**, 2461–2463 (2021).
286. Horio, T., Murata, T. & Murata, T. The role of dynamic instability in microtubule organization. *Front. Plant Sci.* **5**, 1–10 (2014).
287. Michaels, T. C. T., Feng, S., Liang, H. & Mahadevan, L. Mechanics and kinetics of dynamic instability. *Elife* **9**, 1–29 (2020).
288. Li, G. & Moore, J. K. Microtubule dynamics at low temperature: evidence that tubulin recycling limits assembly. *Mol. Biol. Cell* **31**, 1154–1166 (2020).
289. Goodson, H. V. & Jonasson, E. M. Microtubules and Microtubule-Associated Proteins. *Cold Spring Harb. Perspect. Biol.* **10**, a022608 (2018).
290. Wloga, D., Joachimiak, E. & Fabczak, H. Tubulin Post-Translational Modifications and Microtubule Dynamics. *Int. J. Mol. Sci.* **18**, 2207 (2017).
291. de Forges, H., Pilon, A., Poüs, C. & Perez, F. Imaging GTP-Bound Tubulin. in 139–153 (2013). doi:10.1016/B978-0-12-407757-7.00010-4.
292. Stringer, C., Wang, T., Michaelos, M. & Pachitariu, M. Cellpose: a generalist algorithm for cellular segmentation. *Nat. Methods* **18**, 100–106 (2021).
293. Menchon, G. *et al.* A fluorescence anisotropy assay to discover and characterize ligands targeting the maytansine site of tubulin. *Nat. Commun.* **9**, 2106 (2018).
294. Deng, Z., Wang, H., Liu, J., Deng, Y. & Zhang, N. Comprehensive understanding of anchorage-independent survival and its implication in cancer metastasis. *Cell Death Dis.* **12**, 629 (2021).
295. Valastyan, S. & Weinberg, R. A. Tumor metastasis: Molecular insights and evolving paradigms. *Cell* **147**, 275–292 (2011).
296. Yamada, K. M. & Cukierman, E. Modeling Tissue Morphogenesis and Cancer in 3D. *Cell* **130**, 601–610 (2007).
297. Staunton, J. R., Doss, B. L., Lindsay, S. & Ros, R. Correlating confocal microscopy and atomic force indentation reveals metastatic cancer cells stiffen during invasion into collagen i matrices. *Sci. Rep.* **6**, 1–15 (2016).
298. Tang, K., Xin, Y., Li, K., Chen, X. & Tan, Y. Cell Cytoskeleton and Stiffness Are Mechanical Indicators of Organotropism in Breast Cancer. *Biology (Basel).* **10**, 259 (2021).
299. Plodinec, M. *et al.* The nanomechanical signature of breast cancer. *Nat. Nanotechnol.* **7**, 757–765 (2012).

300. Garlick, E., Faulkner, E. L., Briddon, S. J. & Thomas, S. G. Simple methods for quantifying super-resolved cortical actin. *Sci. Rep.* **12**, 2715 (2022).
301. Acerbi, I. *et al.* Human breast cancer invasion and aggression correlates with ECM stiffening and immune cell infiltration. *Integr. Biol.* **7**, 1120–1134 (2015).
302. Hensley, P. J. *et al.* Novel pharmacologic targeting of tight junctions and focal adhesions in prostate cancer cells. *PLoS One* **9**, (2014).
303. Ratner, N. & Miller, S. J. A RASopathy gene commonly mutated in cancer: The neurofibromatosis type 1 tumour suppressor. *Nat. Rev. Cancer* **15**, 290–301 (2015).
304. Akcakanat, A. *et al.* Genomic, Transcriptomic, and Proteomic Profiling of Metastatic Breast Cancer. *Clin. Cancer Res.* **27**, 3243–3252 (2021).
305. Keene, K. S. *et al.* Molecular determinants of post-mastectomy breast cancer recurrence. *npj Breast Cancer* **4**, 34 (2018).
306. Pearson, A. *et al.* Inactivating NF1 Mutations Are Enriched in Advanced Breast Cancer and Contribute to Endocrine Therapy Resistance. *Clin. Cancer Res.* **26**, 608–622 (2020).
307. Sokol, E. S. *et al.* Loss of function of NF1 is a mechanism of acquired resistance to endocrine therapy in lobular breast cancer. *Ann. Oncol.* **30**, 115–123 (2019).
308. Xu, X. *et al.* HER2 reactivation through acquisition of the HER2 L755S mutation as a mechanism of acquired resistance to HER2-targeted therapy in HER2 + breast cancer. *Clin. Cancer Res.* **23**, 5123–5134 (2017).
309. Cocco, E. *et al.* Neratinib is effective in breast tumors bearing both amplification and mutation of ERBB2 (HER2). *Sci. Signal.* **11**, 1–8 (2018).
310. Yi, Z. *et al.* Impact of HER2 mutation status on personalized molecular targeted therapy in advanced breast cancers. *J. Clin. Oncol.* **36**, 1039–1039 (2018).
311. Yi, Z. *et al.* Molecular landscape and efficacy of HER2-targeted therapy in patients with HER2-mutated metastatic breast cancer. *npj Breast Cancer* **6**, 59 (2020).
312. Kurozumi, S. *et al.* Clinicopathological values of PD-L1 expression in HER2-positive breast cancer. *Sci. Rep.* **9**, 16662 (2019).
313. Saito, K. *et al.* Tumor infiltrating lymphocytes as a predictive factor in Pertuzumab/Trastuzumab-treated HER2-positive breast cancer. *Ann. Oncol.* **28**, ix104 (2017).
314. Nuciforo, P. *et al.* Tumor-infiltrating lymphocytes (TILs) in HER2-positive (HER2+) early breast cancer treated with neoadjuvant lapatinib and trastuzumab without chemotherapy

in the PAMELA Trial. *Ann. Oncol.* **28**, v46 (2017).

315. El Bairi, K. *et al.* The tale of TILs in breast cancer: A report from The International Immuno-Oncology Biomarker Working Group. *npj Breast Cancer* **7**, 150 (2021).
316. Dawood, S., Schuster, K. & Fedlman, R. Comparison of tumor mutational burden and pd-l1 between 2797 primary and metastatic breast cancer samples. *Ann. Oncol.* **29**, ix117 (2018).
317. Barroso-Sousa, R. *et al.* Prevalence and mutational determinants of high tumor mutation burden in breast cancer. *Ann. Oncol.* **31**, 387–394 (2020).
318. Sammons, S. *et al.* Genomic evaluation of tumor mutational burden-high (TMB-H) versus TMB-low (TMB-L) metastatic breast cancer to reveal unique mutational features. *J. Clin. Oncol.* **39**, 1091–1091 (2021).
319. Lambert, J. M. & Morris, C. Q. Antibody–Drug Conjugates (ADCs) for Personalized Treatment of Solid Tumors: A Review. *Adv. Ther.* **34**, 1015–1035 (2017).
320. Diéras, V. *et al.* Abstract PD8-02: Trastuzumab deruxtecan (T-DXd) for advanced breast cancer patients (ABC), regardless HER2 status: A phase II study with biomarkers analysis (DAISY). *Cancer Res.* **82**, PD8-02-PD8-02 (2022).
321. Prat, A. *et al.* Development and validation of the new HER2DX assay for predicting pathological response and survival outcome in early-stage HER2-positive breast cancer. *eBioMedicine* **75**, 103801 (2022).
322. Drake, P. M. & Rabuka, D. Recent Developments in ADC Technology: Preclinical Studies Signal Future Clinical Trends. *BioDrugs* **31**, 521–531 (2017).
323. Hedrich, W. D., Fandy, T. E., Ashour, H. M., Wang, H. & Hassan, H. E. Antibody–Drug Conjugates: Pharmacokinetic/Pharmacodynamic Modeling, Preclinical Characterization, Clinical Studies, and Lessons Learned. *Clin. Pharmacokinet.* **57**, 687–703 (2018).
324. Perez, E. A. *et al.* Trastuzumab Emtansine With or Without Pertuzumab Versus Trastuzumab Plus Taxane for Human Epidermal Growth Factor Receptor 2–Positive, Advanced Breast Cancer: Primary Results From the Phase III MARIANNE Study. *J. Clin. Oncol.* **35**, 141–148 (2017).
325. Swain, S. M. *et al.* Multidisciplinary clinical guidance on trastuzumab deruxtecan (T-DXd)–related interstitial lung disease/pneumonitis—Focus on proactive monitoring, diagnosis, and management. *Cancer Treat. Rev.* **106**, 102378 (2022).
326. Rugo, H. S., Bianchini, G., Cortes, J., Henning, J.-W. & Untch, M. Optimizing treatment management of trastuzumab deruxtecan in clinical practice of breast cancer. *ESMO Open* **7**,

100553 (2022).

327. Krop, I. E. *et al.* Trastuzumab emtansine versus treatment of physician's choice in patients with previously treated HER2-positive metastatic breast cancer (TH3RESA): final overall survival results from a randomised open-label phase 3 trial. *Lancet Oncol.* **18**, 743–754 (2017).
328. Nik-Zainal, S. *et al.* Landscape of somatic mutations in 560 breast cancer whole-genome sequences. *Nature* **534**, 47–54 (2016).
329. Rossi, S. *et al.* Neurofibromin C terminus-specific antibody (clone NFC) is a valuable tool for the identification of NF1-inactivated GISTs. *Mod. Pathol.* **31**, 160–168 (2018).
330. Bollinger, J. A., Imam, Z. I., Stevens, M. J. & Bachand, G. D. Tubulin islands containing slowly hydrolyzable GTP analogs regulate the mechanism and kinetics of microtubule depolymerization. *Sci. Rep.* **10**, 13661 (2020).
331. Severin, F. F., Sorger, P. K. & Hyman, A. A. Kinetochores distinguish GTP from GDP forms of the microtubule lattice. *Nature* **388**, 888–890 (1997).
332. Redwine, W. B. *et al.* Structural Basis for Microtubule Binding and Release by Dynein. *Science (80-.).* **337**, 1532–1536 (2012).
333. Gireesh, K. K. *et al.* Microtubule +TIP Protein EB1 Binds to GTP and Undergoes Dissociation from Dimer to Monomer on Binding GTP. *Biochemistry* **53**, 5551–5557 (2014).
334. Gireesh, K. K., Shine, A., Lakshmi, R. B., Vijayan, V. & Manna, T. K. GTP-binding facilitates EB1 recruitment onto microtubules by relieving its auto-inhibition. *Sci. Rep.* **8**, 1–13 (2018).
335. Kwok, B. H. & Paydar, M. Evidence for Conformational Change-Induced Hydrolysis of β-Tubulin-GTP. *SSRN Electron. J.* (2020) doi:10.2139/ssrn.3687033.
336. Alushin, G. M. *et al.* High-Resolution microtubule structures reveal the structural transitions in αβ-tubulin upon GTP hydrolysis. *Cell* **157**, 1117–1129 (2014).
337. Petry, S. Mechanisms of Mitotic Spindle Assembly. *Annu. Rev. Biochem.* **85**, 659–683 (2016).
338. Prosser, S. L. & Pelletier, L. Mitotic spindle assembly in animal cells: a fine balancing act. *Nat. Rev. Mol. Cell Biol.* **18**, 187–201 (2017).
339. Cormier, A., Marchand, M., Ravelli, R. B. G., Knossow, M. & Gigant, B. Structural insight into the inhibition of tubulin by vinca domain peptide ligands. *EMBO Rep.* **9**, 1101–1106 (2008).
340. Després, P. C., Dubé, A. K., Seki, M., Yachie, N. & Landry, C. R. Perturbing proteomes at single residue resolution using base editing. *Nat. Commun.* **11**, 1871 (2020).
341. Rees, H. A. & Liu, D. R. Base editing: precision chemistry on the genome and transcriptome

of living cells. *Nat. Rev. Genet.* **19**, 770–788 (2018).

342. Hess, G. T., Tycko, J., Yao, D. & Bassik, M. C. Methods and Applications of CRISPR-Mediated Base Editing in Eukaryotic Genomes. *Mol. Cell* **68**, 26–43 (2017).
343. Natarajan, K. & Senapati, S. Understanding the Basis of Drug Resistance of the Mutants of αβ-Tubulin Dimer via Molecular Dynamics Simulations. *PLoS One* **7**, e42351 (2012).
344. Attard, T. J., Welburn, J. P. I. & Marsh, J. A. Understanding molecular mechanisms and predicting phenotypic effects of pathogenic tubulin mutations. *PLOS Comput. Biol.* **18**, e1010611 (2022).
345. Lin, C. M. & Hamel, E. Interrelationships of tubulin-GDP and tubulin-GTP in microtubule assembly. *Biochemistry* **26**, 7173–7182 (1987).
346. Ayukawa, R. *et al.* GTP-dependent formation of straight tubulin oligomers leads to microtubule nucleation. *J. Cell Biol.* **220**, (2021).
347. Jonasson, E. M. *et al.* Behaviors of individual microtubules and microtubule populations relative to critical concentrations: dynamic instability occurs when critical concentrations are driven apart by nucleotide hydrolysis. *Mol. Biol. Cell* **31**, 589–618 (2020).
348. Lin, C. M. & Hamel, E. Effects of inhibitors of tubulin polymerization on GTP hydrolysis. *J. Biol. Chem.* **256**, 9242–9245 (1981).
349. Ganem, N. J., Godinho, S. A. & Pellman, D. A mechanism linking extra centrosomes to chromosomal instability. *Nature* **460**, 278–282 (2009).
350. Wojcik, E. J. *et al.* Kinesin-5: Cross-bridging mechanism to targeted clinical therapy. *Gene* **531**, 133–149 (2013).
351. Daigo, K. *et al.* Characterization of KIF11 as a novel prognostic biomarker and therapeutic target for oral cancer. *Int. J. Oncol.* **52**, 155–165 (2018).
352. Jungwirth, G. *et al.* KIF11 inhibitors filanesib and ispinesib inhibit meningioma growth in vitro and in vivo. *Cancer Lett.* **506**, 1–10 (2021).
353. Masanas, M. *et al.* The oral KIF11 inhibitor 4SC-205 exhibits antitumor activity and potentiates standard and targeted therapies in primary and metastatic neuroblastoma models. *Clin. Transl. Med.* **11**, (2021).
354. Shahin, R. & Aljamal, S. Kinesin spindle protein inhibitors in cancer: from high throughput screening to novel therapeutic strategies. *Futur. Sci. OA* **8**, (2022).
355. Sarli, V. & Giannis, A. Targeting the Kinesin Spindle Protein: Basic Principles and Clinical Implications. *Clin. Cancer Res.* **14**, 7583–7587 (2008).

356. Terribas, E. *et al.* KIF11 and KIF15 mitotic kinesins are potential therapeutic vulnerabilities for malignant peripheral nerve sheath tumors. *Neuro-Oncology Adv.* **2**, i62–i74 (2020).
357. Nigg, E. A. Centrosome aberrations: cause or consequence of cancer progression? *Nat. Rev. Cancer* **2**, 815–825 (2002).
358. Brinkley, B. Managing the centrosome numbers game: from chaos to stability in cancer cell division. *Trends Cell Biol.* **11**, 18–21 (2001).
359. Krämer, A., Maier, B. & Bartek, J. Centrosome clustering and chromosomal (in)stability: A matter of life and death. *Mol. Oncol.* **5**, 324–335 (2011).
360. Rubtsova, S. N., Zhitnyak, I. Y. & Gloushankova, N. A. A novel role of e-cadherin-based adherens junctions in neoplastic cell dissemination. *PLoS One* **10**, 1–17 (2015).
361. Kota, P. *et al.* M-Ras/Shoc2 signaling modulates E-cadherin turnover and cell–cell adhesion during collective cell migration. *Proc. Natl. Acad. Sci.* **116**, 3536–3545 (2019).
362. Karagiannis, G. S. *et al.* Collective migration of cancer-associated fibroblasts is enhanced by overexpression of tight junction-associated proteins claudin-11 and occludin. *Mol. Oncol.* **8**, 178–195 (2014).
363. Barth, A. I. M., Kim, H. & Riedel-Kruse, I. H. Regulation of epithelial migration by epithelial cell adhesion molecule requires its Claudin-7 interaction domain. *PLoS One* **13**, 1–24 (2018).
364. Pierceall, W. E., Woodard, A. S., Morrow, J. S., Rimm, D. & Fearon, E. R. Frequent alterations in E-cadherin and alpha- and beta-catenin expression in human breast cancer cell lines. *Oncogene* **11**, 1319–26 (1995).
365. Karcini, A. & Lazar, I. M. The SKBR3 cell-membrane proteome reveals telltales of aberrant cancer cell proliferation and targets for precision medicine applications. *Sci. Rep.* **12**, 10847 (2022).
366. Krieg, M. *et al.* Atomic force microscopy-based mechanobiology. *Nat. Rev. Phys.* **1**, 41–57 (2018).
367. Fidler, I. J. The pathogenesis of cancer metastasis: the 'seed and soil' hypothesis revisited. *Nat. Rev. Cancer* **3**, 453–458 (2003).
368. Gkountela, S., Szczerba, B., Donato, C. & Aceto, N. Recent advances in the biology of human circulating tumour cells and metastasis. *ESMO Open* **1**, e000078 (2016).
369. Guadamillas, M. C., Cerezo, A. & del Pozo, M. A. Overcoming anoikis – pathways to anchorage-independent growth in cancer. *J. Cell Sci.* **124**, 3189–3197 (2011).
370. Yu, M. *et al.* RNA sequencing of pancreatic circulating tumour cells implicates WNT

signalling in metastasis. *Nature* **487**, 510–513 (2012).

371. Paoli, P., Giannoni, E. & Chiarugi, P. Anoikis molecular pathways and its role in cancer progression. *Biochim. Biophys. Acta - Mol. Cell Res.* **1833**, 3481–3498 (2013).
372. Aceto, N. *et al.* Circulating tumor cell clusters are oligoclonal precursors of breast cancer metastasis. *Cell* **158**, 1110–1122 (2014).
373. Suhail, Y. *et al.* Systems Biology of Cancer Metastasis. *Cell Syst.* **9**, 109–127 (2019).
374. Carstens, J. L. *et al.* Stabilized epithelial phenotype of cancer cells in primary tumors leads to increased colonization of liver metastasis in pancreatic cancer. *Cell Rep.* **35**, 108990 (2021).
375. Nyga, A., Ganguli, S., Matthews, H. K. & Baum, B. The role of RAS oncogenes in controlling epithelial mechanics. *Trends Cell Biol.* **33**, 60–69 (2023).
376. Stuelten, C. H., Parent, C. A. & Montell, D. J. Cell motility in cancer invasion and metastasis: insights from simple model organisms. *Nat. Rev. Cancer* **18**, 296–312 (2018).
377. Elisha, Y., Kalchenko, V., Kuznetsov, Y. & Geiger, B. Dual role of E-cadherin in the regulation of invasive collective migration of mammary carcinoma cells. *Sci. Rep.* **8**, 4986 (2018).
378. Huang, B. *et al.* Modeling the Transitions between Collective and Solitary Migration Phenotypes in Cancer Metastasis. *Sci. Rep.* **5**, 17379 (2015).
379. Larribère, L. *et al.* NF1-RAC1 axis regulates migration of the melanocytic lineage. *Transl. Oncol.* **13**, 100858 (2020).
380. Collins, S. E. *et al.* Ras-mediated activation of mTORC2 promotes breast epithelial cell migration and invasion. *Mol. Biol. Cell* **34**, (2023).
381. Boyanapalli, M. *et al.* Neurofibromin binds to caveolin-1 and regulates ras, FAK, and Akt. *Biochem. Biophys. Res. Commun.* **340**, 1200–1208 (2006).
382. Kaplan, K. B. *et al.* A role for the Adenomatous Polyposis Coli protein in chromosome segregation. *Nat. Cell Biol.* **3**, 429–432 (2001).
383. Pease, J. C. & Tirnauer, J. S. Mitotic spindle misorientation in cancer - out of alignment and into the fire. *J. Cell Sci.* **124**, 1007–1016 (2011).
384. He, J. *et al.* PTEN regulates EG5 to control spindle architecture and chromosome congression during mitosis. *Nat. Commun.* **7**, (2016).
385. Ban, S. *et al.* Chromosomal instability in BRCA1- or BRCA2-defective human cancer cells detected by spontaneous micronucleus assay. *Mutat. Res. Mol. Mech. Mutagen.* **474**, 15–23 (2001).
386. Shindo, N., Otsuki, M., Uchida, K. S. K. & Hirota, T. Prolonged mitosis causes separase

deregulation and chromosome nondisjunction. *Cell Rep.* **34**, 108652 (2021).

387. Silkworth, W. T., Nardi, I. K., Scholl, L. M. & Cimini, D. Multipolar Spindle Pole Coalescence Is a Major Source of Kinetochore Mis-Attachment and Chromosome Mis-Segregation in Cancer Cells. *PLoS One* **4**, e6564 (2009).
388. Lingle, W. L. *et al.* Centrosome amplification drives chromosomal instability in breast tumor development. *Proc. Natl. Acad. Sci.* **99**, 1978–1983 (2002).
389. Karki, M., Keyhaninejad, N. & Shuster, C. B. Precocious centriole disengagement and centrosome fragmentation induced by mitotic delay. *Nat. Commun.* **8**, 15803 (2017).
390. Weaver, R. L. *et al.* BubR1 alterations that reinforce mitotic surveillance act against aneuploidy and cancer. *Elife* **5**, (2016).
391. Soto, D. & Sukumar, S. Improved detection of mutations in the p53 gene in human tumors as single-stranded conformation polymorphs and double-stranded heteroduplex DNA. *Genome Res.* **2**, 96–98 (1992).
392. Ippolito, M. R. *et al.* Gene copy-number changes and chromosomal instability induced by aneuploidy confer resistance to chemotherapy. *Dev. Cell* **56**, 2440-2454.e6 (2021).
393. Ben-David, U. *et al.* Patient-derived xenografts undergo mouse-specific tumor evolution. *Nat. Genet.* **49**, 1567–1575 (2017).
394. Wuerstlein, R. *et al.* Final results of the global and Asia cohorts of KAMILLA, a phase IIIB safety trial of trastuzumab emtansine in patients with HER2-positive advanced breast cancer. *ESMO Open* **7**, 100561 (2022).
395. Brasó-Maristany, F. *et al.* HER2DX ERBB2 mRNA expression in advanced HER2-positive breast cancer treated with T-DM1. *JNCI J. Natl. Cancer Inst.* (2022) doi:10.1093/jnci/djac227.
396. Coelho, M. A. *et al.* Oncogenic RAS Signaling Promotes Tumor Immunoresistance by Stabilizing PD-L1 mRNA. *Immunity* **47**, 1083-1099.e6 (2017).
397. Nichols, R. J. *et al.* RAS nucleotide cycling underlies the SHP2 phosphatase dependence of mutant BRAF-, NF1- and RAS-driven cancers. *Nat. Cell Biol.* **20**, 1064–1073 (2018).
398. Bunda, S. *et al.* Inhibition of SHP2-mediated dephosphorylation of Ras suppresses oncogenesis. *Nat. Commun.* **6**, (2015).
399. Wang, Y. *et al.* SHP2 blockade enhances anti-tumor immunity via tumor cell intrinsic and extrinsic mechanisms. *Sci. Rep.* **11**, 1399 (2021).
400. Scribano, C. M. *et al.* Chromosomal instability sensitizes patient breast tumors to multipolar

divisions induced by paclitaxel. *Sci. Transl. Med.* **13**, (2021).

401. Gordon, D. J., Resio, B. & Pellman, D. Causes and consequences of aneuploidy in cancer. *Nat. Rev. Genet.* **13**, 189–203 (2012).
402. Lukow, D. A. *et al.* Chromosomal instability accelerates the evolution of resistance to anti-cancer therapies. *Dev. Cell* **56**, 2427-2439.e4 (2021).
403. Spurr, L. F. *et al.* Highly aneuploid non-small cell lung cancer shows enhanced responsiveness to concurrent radiation and immune checkpoint blockade. *Nat. Cancer* **3**, 1498–1512 (2022).
404. Kwon, J. & Bakhoum, S. F. The Cytosolic DNA-Sensing cGAS–STING Pathway in Cancer. *Cancer Discov.* **10**, 26–39 (2020).
405. Kwon, M., Leibowitz, M. L. & Lee, J.-H. Small but mighty: the causes and consequences of micronucleus rupture. *Exp. Mol. Med.* **52**, 1777–1786 (2020).
406. Davoli, T., Uno, H., Wooten, E. C. & Elledge, S. J. Tumor aneuploidy correlates with markers of immune evasion and with reduced response to immunotherapy. *Science (80-.).* **355**, (2017).
407. Spurr, L. F., Weichselbaum, R. R. & Pitroda, S. P. Tumor aneuploidy predicts survival following immunotherapy across multiple cancers. *Nat. Genet.* **54**, 1782–1785 (2022).
408. Kuang, X. & Li, J. Chromosome instability and aneuploidy as context-dependent activators or inhibitors of antitumor immunity. *Front. Immunol.* **13**, (2022).
409. Müller, P. *et al.* Trastuzumab emtansine (T-DM1) renders HER2+ breast cancer highly susceptible to CTLA-4/PD-1 blockade. *Sci. Transl. Med.* **7**, (2015).
410. Harbeck, N. *et al.* Immune Markers and Tumor-Related Processes Predict Neoadjuvant Therapy Response in the WSG-ADAPT HER2-Positive/Hormone Receptor-Positive Trial in Early Breast Cancer. *Cancers (Basel).* **13**, 4884 (2021).
411. Emens, L. A. *et al.* Trastuzumab emtansine plus atezolizumab versus trastuzumab emtansine plus placebo in previously treated, HER2-positive advanced breast cancer (KATE2): a phase 2, multicentre, randomised, double-blind trial. *Lancet Oncol.* **21**, 1283–1295 (2020).
412. Waks, A. G. *et al.* Phase Ib study of pembrolizumab in combination with trastuzumab emtansine for metastatic HER2-positive breast cancer. *J. Immunother. Cancer* **10**, e005119 (2022).
413. Hurvitz, S. A. *et al.* ASTEFANIA: adjuvant ado-trastuzumab emtansine and atezolizumab for high-risk, HER2-positive breast cancer. *Futur. Oncol.* **18**, 3563–3572 (2022).

414. Shukla, A. *et al.* Chromosome arm aneuploidies shape tumour evolution and drug response. *Nat. Commun.* **11**, 1–14 (2020).
415. Wu, X. *et al.* Skin Stem Cells Orchestrate Directional Migration by Regulating Microtubule-ACF7 Connections through GSK3β. *Cell* **144**, 341–352 (2011).
416. Zaoui, K., Benseddik, K., Daou, P., Salaün, D. & Badache, A. ErbB2 receptor controls microtubule capture by recruiting ACF7 to the plasma membrane of migrating cells. *Proc. Natl. Acad. Sci.* **107**, 18517–18522 (2010).
417. Ma, Y. *et al.* ACF7 regulates inflammatory colitis and intestinal wound response by orchestrating tight junction dynamics. *Nat. Commun.* **8**, 15375 (2017).
418. Shi, J. *et al.* Discovery of cancer drug targets by CRISPR-Cas9 screening of protein domains. *Nat. Biotechnol.* **33**, 661–667 (2015).
419. D'Amico, L. *et al.* A novel anti-HER2 anthracycline-based antibody-drug conjugate induces adaptive anti-tumor immunity and potentiates PD-1 blockade in breast cancer. *J. Immunother. cancer* **7**, 16 (2019).
420. Zhu, Y. *et al.* Ablation of NF1 function in neurons induces abnormal development of cerebral cortex and reactive gliosis in the brain. *Genes Dev.* **15**, 859–876 (2001).
421. Ran, F. A. *et al.* Genome engineering using the CRISPR-Cas9 system. **8**, 2281–2308 (2013).
422. Falkowska-Hansen, B. *et al.* An inducible Tet-Off-H2B-GFP lentiviral reporter vector for detection and in vivo isolation of label-retaining cells. *Exp. Cell Res.* **316**, 1885–1895 (2010).
423. Nam, H. & Benezra, R. High Levels of Id1 Expression Define B1 Type Adult Neural Stem Cells. *Cell Stem Cell* **5**, 515–526 (2009).
424. Dobin, A. *et al.* STAR: ultrafast universal RNA-seq aligner. *Bioinformatics* **29**, 15–21 (2013).
425. Church, D. M. *et al.* Modernizing Reference Genome Assemblies. *PLoS Biol.* **9**, e1001091 (2011).
426. Anders, S., Pyl, P. T. & Huber, W. HTSeq—a Python framework to work with high-throughput sequencing data. *Bioinformatics* **31**, 166–169 (2015).
427. Love, M. I., Huber, W. & Anders, S. Moderated estimation of fold change and dispersion for RNA-seq data with DESeq2. *Genome Biol.* **15**, 550 (2014).
428. Kim, D. *et al.* PKCα-LSD1-NF-κB-Signaling Cascade Is Crucial for Epigenetic Control of the Inflammatory Response. *Mol. Cell* **69**, 398-411.e6 (2018).
429. Kuleshov, M. V. *et al.* Enrichr: a comprehensive gene set enrichment analysis web server 2016 update. *Nucleic Acids Res.* **44**, W90–W97 (2016).

430. Xie, Z. *et al.* Gene Set Knowledge Discovery with Enrichr. *Curr. Protoc.* **1**, (2021).
431. Subramanian, A. *et al.* Gene set enrichment analysis: A knowledge-based approach for interpreting genome-wide expression profiles. *Proc. Natl. Acad. Sci.* **102**, 15545–15550 (2005).
432. Liberzon, A. *et al.* Molecular signatures database (MSigDB) 3.0. *Bioinformatics* **27**, 1739–1740 (2011).
433. Liberzon, A. *et al.* The Molecular Signatures Database Hallmark Gene Set Collection. *Cell Syst.* **1**, 417–425 (2015).
434. Tinevez, J.-Y. *et al.* TrackMate: An open and extensible platform for single-particle tracking. *Methods* **115**, 80–90 (2017).
435. Ershov, D. *et al.* Bringing TrackMate into the era of machine-learning and deep-learning. *bioRxiv* 2021.09.03.458852 (2021).
436. Cowley, G. S. *et al.* Parallel genome-scale loss of function screens in 216 cancer cell lines for the identification of context-specific genetic dependencies. *Sci. Data* **1**, 140035 (2014).
437. Puricelli, L., Galluzzi, M., Schulte, C., Podestà, A. & Milani, P. Nanomechanical and topographical imaging of living cells by atomic force microscopy with colloidal probes. *Rev. Sci. Instrum.* **86**, 033705 (2015).
438. Hutter, J. L. & Bechhoefer, J. Calibration of atomic-force microscope tips. *Rev. Sci. Instrum.* **64**, 1868–1873 (1993).
439. Butt, H.-J. & Jaschke, M. Calculation of thermal noise in atomic force microscopy. *Nanotechnology* **6**, 1–7 (1995).

APPENDIX

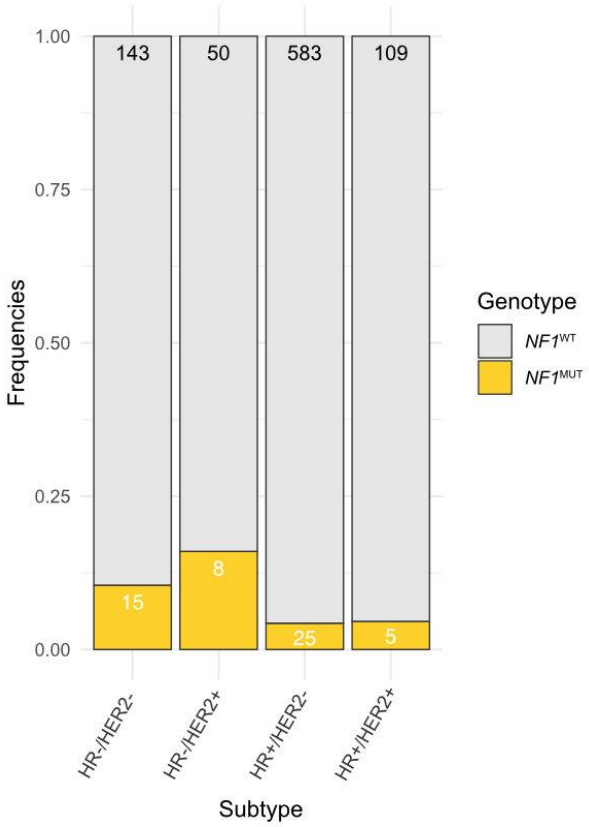

Figure A1. *NF1* mutational prevalence according to IHC-derived BC subtype classification, from the AACR-GENIE dataset. Numbers are absolute samples and bars are proportions within each subtype.

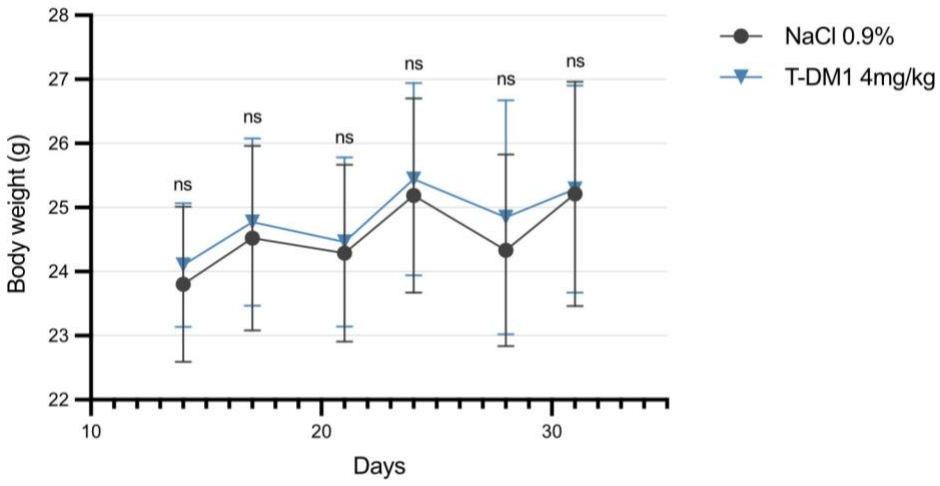

Figure A2. Body weight of mice throughout experiment, treated with vehicle or T-DM1 4mg/kg IV.

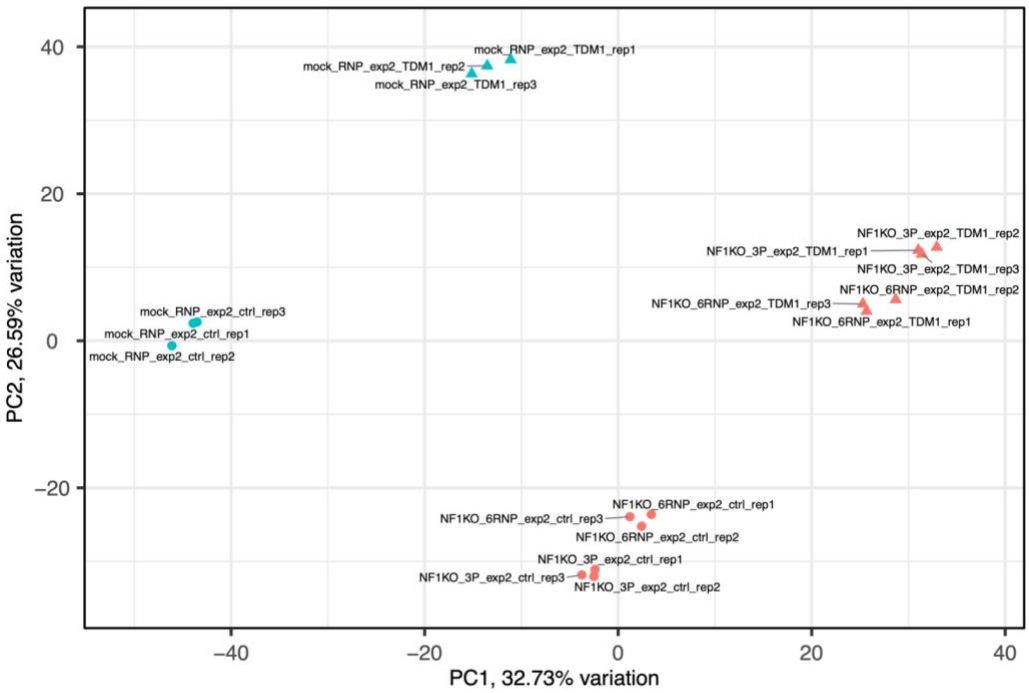

Figure A3. Principal component analysis (PCA) from RNA-seq (*figure R11*).